Unraveling Flashback Phenomena of Turbulent premixed Hydrogen-Natural Gas-Air Flames

G. Willems

Technische Universiteit Delft

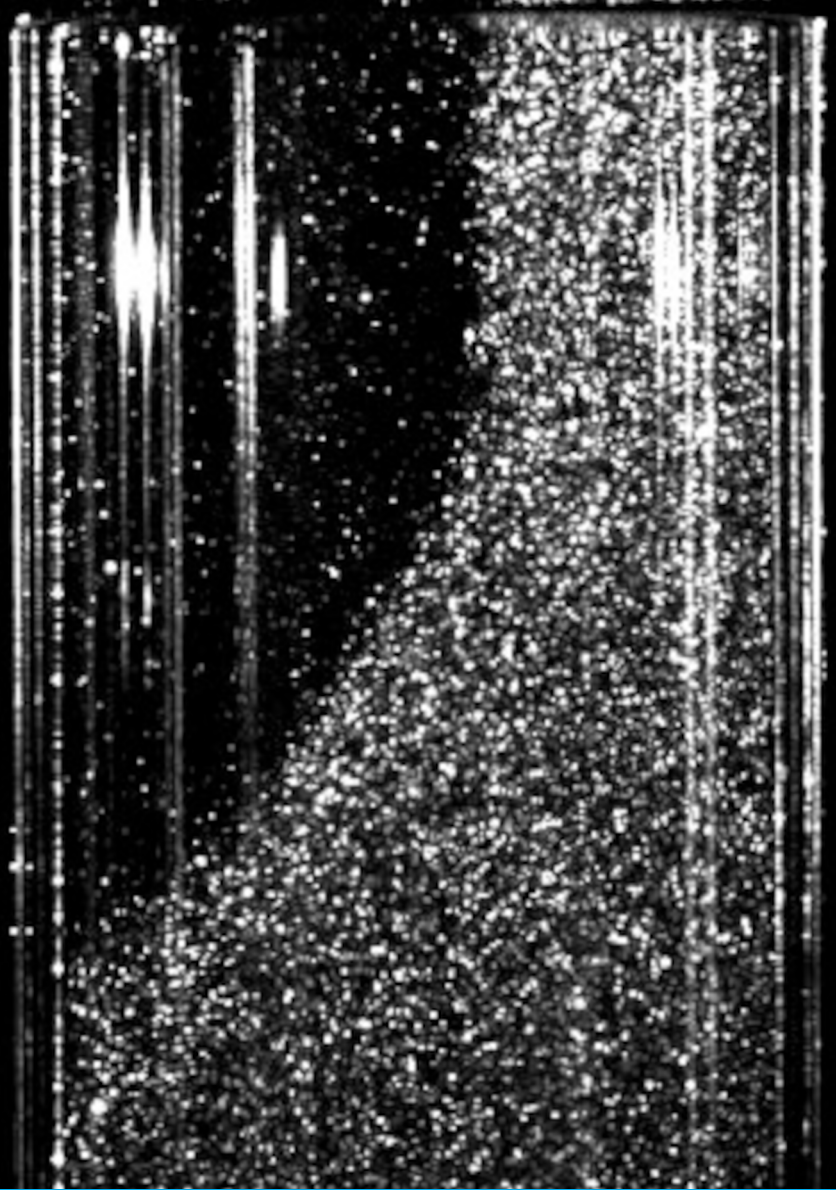

TU Delft

Unraveling Flashback Phenomena of Turbulent premixed Hydrogen-Natural Gas-Air Flames

by

G. Willems

to obtain the degree of Master of Science
at the Delft University of Technology,
to be defended publicly on 25 February 2022.

Student number: 4597745
Thesis committee:
Prof. dr. ir. S.A. Klein, TU Delft, supervisor, chair
Dr. ir. M. J. Tummers, TU Delft, supervisor
Ir. A. Altenburg, TU Delft
Prof. dr. ir. D.J.E.M. Roekaerts, TU Delft

An electronic version of this thesis is available at http://repository.tudelft.nl/.

TU Delft

Abstract

The growing energy demand and climate change poses a need for alternative energy generation in terms of renewable resources. Renewable energy resources are characterised by their intermittent behaviour. A backup power supply is required that can deliver electricity when the supply from the renewables is not sufficient. Gas turbines operating with hydrogen is an attractive option, since hydrogen combustion has zero carbon emissions and can be used as an energy storage when the supply of renewable energy sources are abundant. However, hydrogen combustion poses several challenges. A hydrogen flame has a higher flame temperature than natural gas, leading to more NO_x production. To reduce these NO_x emissions, gas turbines operate in lean premixed conditions. This creates a risk of flame flashback, in particular boundary layer flashback, which can lead to severe damage to the gas turbine. Recent research performed on boundary layer flashback revealed that two flame configurations, i.e. unconfined and confined, showed fundamentally different flashback phenomena. Unconfined flame flashback refers to the situation where an initially stable flame anchored at the burner rim eventually moves into burner tube. When a flame is partially of completely surrounded by walls and propagates and then starts propagation along the wall, it is called confined flame flashback. Previous studies have focused on one of the two flashback processes at a time. However, the transient flashback process between unconfined and confined flame flashback is not well understood. Research has shown that hydrogen is much more prone to flashback compared to natural gas. This has been attributed to the difference in flame speed between natural gas and hydrogen, but the exact reason for the difference in flashback behaviour between natural gas flames and hydrogen flames has yet to be found.

In this study, a quartz Bunsen burner is used to investigate the flashback phenomena of turbulent premixed hydrogen-natural gas-air flames. To gain more insight in the flashback phenomena, three experiments have been performed. First, flashback maps are obtained to determine the flashback limits of the quartz Bunsen burner. Secondly, the influence of a flame on the flow was investigated using turbulent statistics. Finally, both unconfined and confined flashback are visualised, thereby capturing the transient flashback process between these two configurations. This has been done for a stoichiometric natural gas flame and a lean hydrogen flame. Laser diagnostics like Particle Image Velocimetry (PIV) and Mie-scattering are used to obtain the turbulent flow statistics and to visualize the instantaneous flashback process.

The results show that regions with negative velocity fluctuations in the unburned mixture are the predominant physical mechanism for the start of unconfined flashback and for the transient flashback process of the flame propagating into the burner. However, the start of a flashback event depends on the combination of several parameters: the bulk velocity, the position of the flame front before it interacts with a region with negative velocity fluctuations, the magnitude of the negative velocity fluctuations and whether a region with positive velocity fluctuations is absent after interaction of the flame with the region consisting of negative fluctuations. So, unconfined flashback is rather a statistical phenomena, where the chance of the occurrence of a flashback event is increasing for a decreasing bulk flow velocity. Experiments showed that the transient process between unconfined and confined flashback is very short and fast. After a distance of approximately 5 mm upstream of the burner rim, a backflow region starts to develop in front of the flame, which denotes the start of confined flashback. The time needed for a natural gas flame propagating upstream from the burner rim to reach a confined configuration is approximately 17 ms and only 5.6 ms for the hydrogen flame. The suggested physical mechanisms leading from unconfined flashback to confined flashback are the convex shape of the flame towards the reactants during upstream flame propagation and the reduced cross-sectional flow area of the burned gases at the flame tip. Due to the created backflow in front of the flame and the above-mentioned mechanisms, the upstream flame propagation is strongly enhanced, which explains why the flashback propensity for confined flames is much higher than for unconfined flames. The experiments showed that the hydrogen flame propagates closer to the wall than the natural gas flame, indicating higher backpressure effects. The hydrogen flame is thermal-diffusive unstable and the convex shape of the

flame tip during flashback strongly enhances the local flame speed and thus the upstream propagation velocity. In contrast, the hydrodynamic instability encountered in the natural gas flame only retards the flow in front of the flame tip, but does not affect the flame speed. This might explain the difference in flashback behaviour between natural gas and hydrogen flames.

Acknowledgements

First of all, I want to thank my supervisors Mark Tummers, Sikke Klein and Luuk Altenburg for the opportunity and the possibility to work on this experimental graduation project during the COVID-19 pandemic. The meetings and discussions we had helped me to stay on the right track and kept me motivated and focused. It was a very pleasant working environment and in that respect I also want to thank Fedor van der Laan for working together in the lab.
I want to thank Bart Hoek for the help on the construction of the experimental setup and for the daily provision of coffee. Also, I want to thank Edwin Overmars for helping me to get familiar with the measuring equipment.
Next, I would like to say a big thank you to my friends Edwin Verlaan, Joran Hol and Bram Cleijpool for the great times during these years of studying together.
Most of all, I want to give thanks to my God and family for their support and for the provision of everything I needed to be able to reach to this point.

G. Willems
Delft, January 2021

Contents

Nomenclature

Abbreviations

CCGT	Combined Cycle Gas Turbine
CFD	Computational Fluid Dynamics
CIVB	Combustion Induced Vortex Breakdown
DNS	Direct Numerical Simulation
LDA	Laser Doppler Anemometry
NG	Natural Gas
PIV	Particle Image Velocimetry
PLIF	Planar Laser Induced Fluorescence

Greek symbols

α	Flame angle [-]
α	Heat diffusivity [m^2/s]
β	Experimental constant [-]
δ	Thickness [m]
$\epsilon_{R_{xx}}$	Uncertainty in Reynolds stress [m^2/s^2]
ϵ_u	Uncertainty in velocity [m/s]
λ	Thermal conductivity [W/(m·K)]
μ	Dynamic viscosity [Pa·s]
ν	Kinematic viscosity [m^2/s]
ϕ	Equivalence ratio [-]
ρ	Density [kg/m^3]
σ	Density ratio [-]
τ	Shear stress [Pa]
τ	Time [s]
ε	Turbulent dissipation rate [m^2/s^3]

Latin symbols

$\dot{m}$	Mass flux [kg/s]
ℓ	Length [m]
$\mathcal{L}$	Characteristic flow length [m]
$\mathcal{L}_M$	Markstein length [m]

$\mathcal{U}$ Characteristic flow velocity [m/s]

$\mathbb{K}$ Flame stretch rate [s^{-1}]

A Surface area [m^2]

C Dämkohler tuning constant [-]

C Logaritmic wall layer constant [-]

C_p Pressure coefficient [-]

D Diameter [m]

D Mass diffusivity [m^2/s]

d Diameter [m]

d Height from burner inner wall [m]

g Velocity gradient [s^{-1}]

K Von Kármán constant [-]

k Turbulent kinetic energy [m^2/s^2]

l Length [m]

N Number of samples [-]

p Pressure [Pa]

R Radius [m]

R Reynolds stress [m^2/s^2]

r Coordinate in radial direction [m]

r Eddy size [m]

s Flame speed [m/s]

s Height from burner rim [m]

T Measurement Time [s]

T Temperature [K]

t Time [s]

t thickness [m]

u Flow velocity in axial direction [m/s]

u_0 Integration constant core region velocity [-]

U_b Bulk flow velocity [m/s]

x Coordinate in axial direction [m]

Y Mass fraction [-]

y Coordinate normal to burner wall [m]

c_p Specific heat capacity [J/(kg·K]

Non-dimensional numbers

Ka	Karlovitz number
Le	Lewis number
Ma	Markstein number
Pe	Peclet number
Re	Reynolds number
Sc	Schmidt number
St	Stokes number

Subscripts

0	Initial value
0	Turbulent integral scale
0	Unstretched
η	Kolmogorov scale
$\mathbb{K}$	Stretch rate
τ	Friction
ad	Adiabatic
b	Burned
c	Critical
c	Curvature
eff	Effective
F	Fuel
f	Flame
f	Flashback
ft	Flame tip
i	Inner
i, j	Index
l	Laminar
n	Normal
P	Products
p	Particle
p	Penetration
ph	Preheat zone
q	Quench
r	Backflow
r	Reaction zone

s	Strain
t	Turbulent
u	Unburned
w	Wall
Ox	Oxidizer
st	Stoichiometric conditions

Superscripts

n	Exponential constant
’	Fluctuating value
+	Value in wall units
-	Average value

1 Introduction

1.1. Role of hydrogen in the energy transition

The electricity demand in the world has significantly grown in the past decades. Figure 1.1 shows that the generated electricity in the period from 1990-2018 has more than doubled [6]. The usage of large amounts of coal to generate electricity leads to the fact that the electricity industry is one of the most pollutant industries when it comes to CO_2 emissions. CO_2 and also other gases like CH_4 are called greenhouse gases and these are held responsible for the increased land and ocean temperatures, which lead to climate change [52]. Besides the greenhouse effect of fossil fuels, they have limited resources and hence are not renewable. There is therefore a need for alternative energy generation in terms of renewable resources. The share of renewable energy resources such as wind and solar have grown in the European Union from 9.6% to 19.7% in the period 2004-2019 [4]. This considerable amount of renewable energy poses a new challenge. Renewable energy resources like solar power and wind energy are characterised by their intermittent behaviour. To balance the demand and supply in the power system, a backup power supply is required that can deliver electricity when the supply from the renewables is not sufficient [32]. Gas turbines with their fast start-up time and high power range from 1-500 MW are able to deal with this requirement [59]. Currently natural gas is used as a fuel, since it has the lowest CO_2 emissions of all fossil fuels [3], but this is not enough to comply with the long-term goal of the EU. The EU aims at zero carbon emissions in 2050 [5]. Replacing natural gas with hydrogen could be a promising solution. Besides zero carbon emissions when it is burned, this fuel can also be

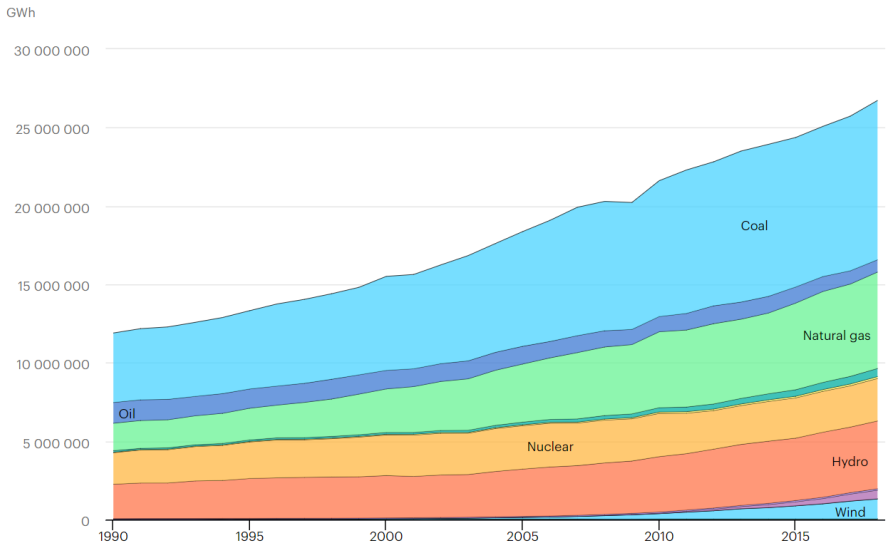

Figure 1.1: Electricity generation in the world by different sources [6].

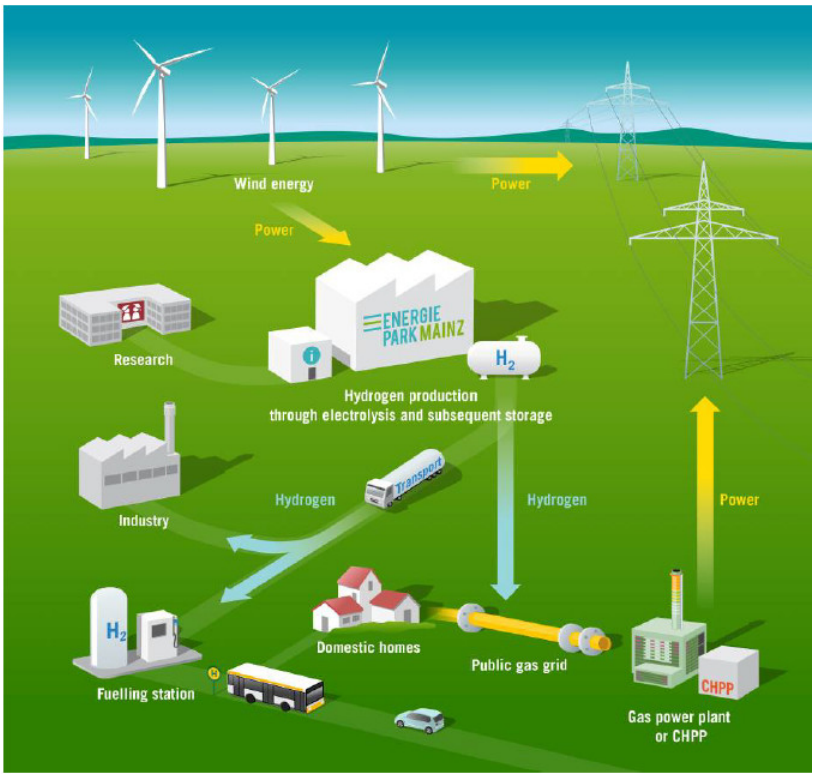

Figure 1.2: An overview of a hydrogen infrastructure with the process of using the excess energy from renewable energy source to generate hydrogen. This generated hydrogen can be used in a gas turbine power plant to generate energy when the energy from the renewable energy sources are not complying with the energy demand. Figure adopted from Zorn [73].

used as an energy storage when the supply of renewable energy sources are abundant. The excess electrical energy can be used to generate hydrogen via electrolysis. There are several ways to store this generated hydrogen [9]. When the energy generated from the renewable energy sources such as wind and solar are scarce and cannot comply with the energy demand, this stored hydrogen can be burned in gas turbines to generate the required energy. Such a hydrogen infrastructure can be seen in Figure 1.2. A study by CE Delft shows that hydrogen combustion in a retrofit of the existing combined cycle gas turbine (CCGT) plants is an attractive option, since the overall efficiency of a CCGT plant is relatively high (55-60 %) and the corresponding investment costs are low [8].

1.2. Hydrogen combustion challenges

Burning hydrogen in a gas turbine instead of natural gas imposes several challenges. First, hydrogen has a higher burning velocity, due to high reactivity and diffusivity. Secondly, hydrogen has a higher adiabatic flame temperature, which leads to higher thermal NO_x emissions which pollute the environment. To reduce these emissions, gas turbines are operated with lean premixed combustion. Lean premixed combustion means that the fuel is mixed with an excess of air before it is combusted in the combustion chamber, see Figure 1.3a. The excess air reduces the flame temperature and consequently NO_x emissions. When fuel and air are premixed upstream of the flame, there is always a risk of upstream flame propagation, see Figure 1.3b. This phenomenon is referred to as flame flashback. Once a flame has propagated upstream and enters the premix section of a combustion chamber, it is usually not possible to bring the flame to its original anchoring position. This leads to damage of the premix section as it is not designed for such high temperatures. Therefore, it is required to turn the engine off when flame flashback occurs. In order to prevent flame flashback within the combustion chamber of a gas turbine, it is important to gain insight into the underlying mechanisms that trigger the flame to propagate upstream.

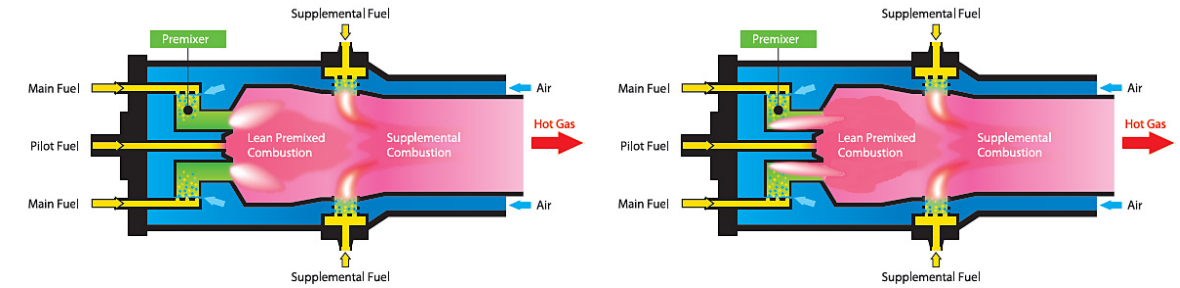

(a) (b)

Figure 1.3: **(a)** Combustion chamber of a gas turbine with stable lean premixed combustion. The flame is anchored at the exit of the premix section. Adopted from Kawasaki Gas Turbine Technology [7]. **(b)** Combustion chamber of a gas turbine with unstable lean premixed combustion. The flame propagates upstream into the premix section, referred to as flashback.

1.2.1. Boundary Layer Flashback

Hydrogen is highly reactive and has a low quenching distance, which means that a hydrogen flame is able to sustain itself very close to a surface. Therefore, it is considered that boundary layer flashback is the most critical flashback mechanism for hydrogen combustion in a gas turbine [37]. Boundary layer flashback refers to the situation where the flame is propagating upstream along the premixer wall as illustrated in Figure 1.4a. At the wall, the flow velocity of the fuel and air mixture goes to zero due due to the no-slip condition. As a result, there are low velocity regions near the wall where the flame is likely to propagate upstream. Much research has been done both experimentally and numerically to understand this mechanism, see the work of Kalantari et al. [39] for an overview. It revealed that boundary layer flashback consists of two flame configurations, which show fundamentally different flashback phenomena. These two flame configurations are referred to as unconfined (open) and confined, see Figure 1.4b. Unconfined flame flashback refers to the situation where an initially stable flame anchored at the burner rim eventually moves into burner tube. When a flame is partially of completely surrounded by walls and propagates and then starts propagation along the wall, it is called confined flame flashback. Studies performed on boundary layer flashback have shown that there is a significant difference in flashback limits between a confined and unconfined flame configuration, where the confined flame configuration is much more prone to flashback [11, 27]. Studies have focused on one of the two flashback processes at a time, i.e. unconfined or confined flashback. However, the transient flashback process of an initial unconfined flame propagating into the (confined) tube is not well understood. Research has also shown that hydrogen is much more prone to flashback compared to natural gas [39]. This has been attributed to the difference in flame speed between natural gas and hydrogen. However, the exact reason for the difference in flashback behaviour between natural gas flames and hydrogen flames is still not found. In order to prevent hydrogen flames from flashing back, it is necessary to gain insight in the physical mechanisms that play a role in the flashback process of hydrogen flames. This will be the focus of the current research.

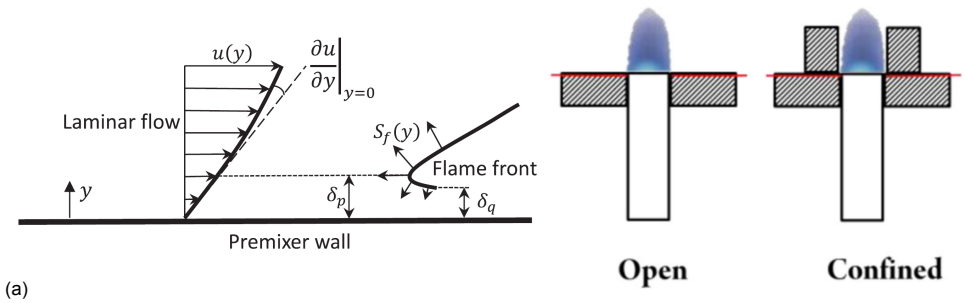

(a) (b)

Figure 1.4: **(a)** Illustration of boundary layer flashback. Adopted from Kalantari et al. [39].**(b)** An open (unconfined) and a confined flame configuration. Adopted from Duan et al. [22].

1.3. Objective of this work

The objective of this project is to gain insight in the physical mechanisms that play a role in the transition from unconfined flame flashback to confined flame flashback. To this end, three questions are formulated:

- *What are the physical mechanisms leading from unconfined flame flashback to confined flame flashback?*
  - *What causes the significant higher flashback limits of a confined flame configuration in comparison to an unconfined flame configuration?*
- *How can the difference in flashback behaviour for hydrogen flames and natural gas flames be explained?*

To answer these questions experiments will be performed using a type of Bunsen burner to gain a fundamental understanding of the flashback process. A Bunsen burner consists of a tube where fuel and air enter from below and are mixed such that at the tube outlet a premixed flame can be established, similar to the open configuration in Figure 1.4. The experiments will be done with premixed turbulent hydrogen-natural gas-air flames at stoichiometric and at lean equivalence ratios. Previous studies have focused on one of the two flashback processes at a time, i.e. unconfined or confined flashback. The focus of this study will be on visualizing both unconfined and confined flashback, thereby capturing the transient flashback process between these two configurations. Therefore, quartz is used as the burner material to visualize both the unburned mixture flow in front of the flame and the flame itself during the flashback process. This will be done with a high spatial and temporal resolution using laser diagnostics: Particle Image Velocimetry (PIV) and Mie-scattering.

1.4. Thesis outline

The outline of this thesis is as follows: in Chapter 2, basic theory of turbulent flow and laminar premixed combustion is provided in the Sections 2.1 - 2.4, which are then combined to discuss turbulent premixed combustion in Section 2.5. Chapter 3 presents the current knowledge on flame flashback mechanism. An overview of all the different flashback mechanisms is given in Section 3.1. Boundary layer flashback is discussed in more detail in Section 3.2, where in particular the difference between unconfined and confined flashback is explained. The details of the experimental setup including the Bunsen burner and the used measurement technique are provided in the Sections 4.1 and 4.2 of Chapter 4. The experimental methodology is discussed in Section 4.3. In Chapter 5 the results of the experiments are presented and analysed. Finally, a summary with conclusions and recommendations is given in Chapter 6.

2

Basics of turbulent flow and combustion

To be able to analyse the flashback mechanisms that play a role in premixed flames it is important to know the phenomena that are encountered in turbulent flow and combustion. This chapter only covers the basics of flow and combustion characteristics that are relevant for this research.

2.1. Turbulent flow

In most industrial applications the flow is turbulent. Therefore, turbulent flow of premixed fuel and air is used in the performed experiments. Figure 2.1 shows the differences between a laminar and turbulent flow. Laminar flow is a layered, smooth flow, whereas turbulent flow is chaotic and fluctuating. To be able to understand how the flame propagates upstream during boundary layer flashback it is important to know the characteristics of the flow. Turbulence adds a lot of complexity to the description of the flow, which will not be discussed in detail here. For a comprehensive study on this topic, the reader is referred to [50, 57]. The Sections 2.1.1 and 2.1.3 provide a description of the mean turbulent flow velocity. Also the scales of turbulent flow are provided in Section 2.1.2, which will be used to describe the effect of turbulence on the flame structure in Section 2.5.

2.1.1. Flow description

Turbulent flow is characterized by a high Reynolds number, which is defined as $\mathrm{Re} = \mathcal{U}\mathcal{L}/\nu$, where $\mathcal{U}$ and $\mathcal{L}$ are the characteristic velocity and length scales of the flow, respectively, and ν is the kinematic viscosity of the fluid [57]. The flow within a Bunsen burner resembles that of a pipe flow. For pipe flow, $\mathcal{U}$ and $\mathcal{L}$ are taken as the bulk velocity (U_b) and the pipe diameter (d), respectively. It is generally assumed that the flow in a pipe is laminar for Reynolds numbers below 2300. Pipe flow is considered fully turbulent for Reynolds numbers higher than approximately $4{\cdot}10^3$, but experiments have shown that this critical number can vary and depends quite strongly on the disturbances caused by the pipe entrance [60].

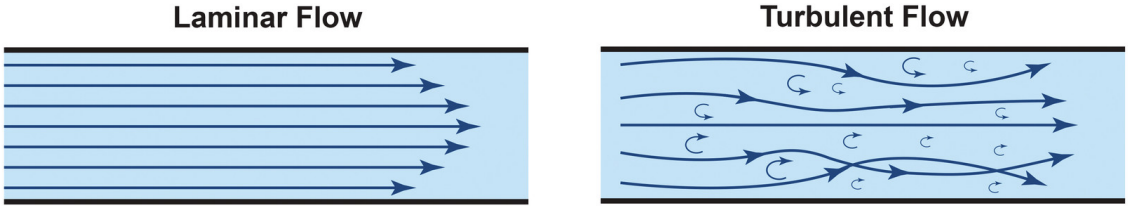

Figure 2.1: Laminar and turbulent flow. Laminar flow is a layered, smooth flow, whereas turbulent flow is chaotic and fluctuating.

In studies of turbulent flow it is common practice to split the instantaneous quantities like velocity and pressure into an ensemble average and a fluctuating component. For the velocity u_i and the pressure p this can be written as:

$$u_i = \overline{u}_i + u_i' \qquad \text{and} \qquad p = \overline{p} + p', \tag{2.1}$$

where the overbar denotes the ensemble average and the prime refers to a fluctuation. This is known as the Reynolds decomposition. Reynolds decomposition together with Reynolds averaging can be applied to the equations describing conservation of mass and momentum, leading to the following equations for mass and momentum in Einstein notation:

Continuity:

$$\frac{\partial \overline{u}_i}{\partial x_i} = 0, \tag{2.2}$$

Momentum:

$$\frac{\partial \overline{u}_i}{\partial t} + \frac{\partial \overline{u}_i \overline{u}_j}{\partial x_j} = -\frac{1}{\rho}\frac{\partial \overline{p}}{\partial x_i} + \nu \frac{\partial^2 \overline{u}_i}{\partial x_j^2} - \frac{\partial \overline{u_i' u_j'}}{\partial x_j}. \tag{2.3}$$

These equations are known as the continuity and Reynolds Averaged Navier-Stokes (RANS) equations, respectively. The flow of the unreacted mixture upstream of the flame can be assumed to be incompressible since the flow velocity is much lower than the speed of sound. Due to the Reynolds averaging the additional term $\overline{u_i' u_j'}$ appears in the momentum equation. This term captures the effect of turbulence and is the so-called Reynolds stress term [50]. This term can be interpreted as the transport in the x_j-direction of momentum per unit mass in the x_i-direction.

2.1.2. Scales of turbulence

Turbulent flow is also characterized by eddies of different length scales. These length scales can be estimated from a spatial correlation function which is based on the velocity fluctuations of two spatially separated points [54]. An important concept in turbulent flow is the energy cascade process, as visualized in Figure 2.2. It states that the kinetic energy enters turbulence in the largest eddies. These large eddies are unstable and break up and transfer their energy to smaller eddies. These smaller eddies also break up into even smaller eddies. This process continues until the smallest scales where viscosity is effective and the kinetic energy is dissipated into heat [57]. The turbulent kinetic energy k is defined as:

$$k = \frac{1}{2}\overline{u_i'^2}. \tag{2.4}$$

In isotropic turbulence, where the velocity fluctuations are equal in every direction, the expression for k reduces to $k = \frac{3}{2}\overline{u'^2}$. The largest eddies which contain the most kinetic energy are characterized by the integral length scale ℓ_0. The length scale is comparable with the flow length scale $\mathcal{L}$ and is typically set by the dimension of the device or confinement of the flow field [44]. The characteristic velocity at this length scale $u_0 \equiv u(\ell_0)$ is on the order of the root mean square turbulent velocity fluctuations $u' = (\frac{2}{3}k)^{1/2}$ and is comparable to $\mathcal{U}$. The Reynolds number of the large eddies, which is also called

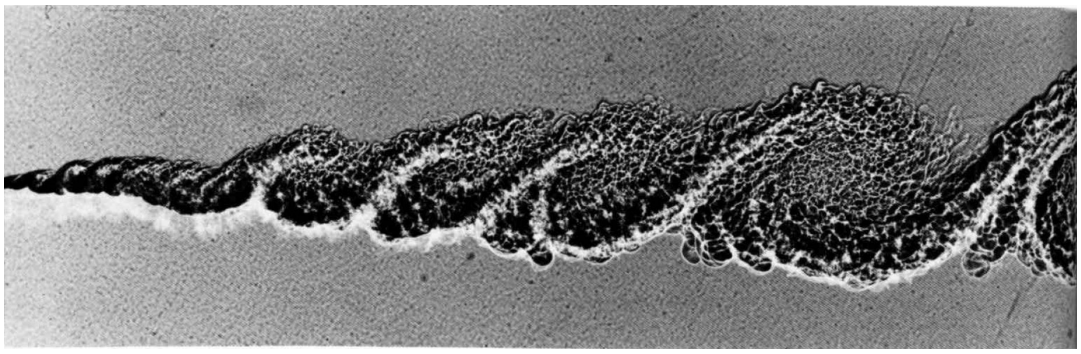

Figure 2.2: Visualisation of a turbulent mixing layer showing the the different length scales in a turbulent flow. Adopted from Van Dyke [65].

the turbulent Reynolds number, $\mathrm{Re}_0 = u'\ell_0/\nu$ is therefore large and comparable to the Reynolds number of the bulk flow. The effects of viscosity are therefore negligible.

According to the energy cascade hypothesis, the kinetic energy is transferred from the large scale eddies to the small scale eddies. Kolmogorov's second similarity hypothesis states that for turbulent flows at sufficient high Reynolds numbers there exists a range of length scales at which the energy dissipation rate is independent of the molecular viscosity. This range of length scales is called the inertial subrange and the energy dissipation rate ε in this range scales with [44]:

$$\varepsilon \sim \frac{u'^3}{\ell_0} \sim \frac{k^{\frac{3}{2}}}{\ell_0}. \tag{2.5}$$

The time scale in which a turbulent eddy loses its energy or breaks up into smaller eddies is then:

$$\tau_0 \sim \frac{\ell_0}{u'} \sim \frac{k}{\varepsilon}. \tag{2.6}$$

As mentioned before, the turbulent kinetic energy is transferred from the large scale eddies to the smaller scale eddies at a rate ε. Eventually the smallest scales are reached where viscosity dominates. The smallest scale is called the Kolmogorov scale, denoted by the subscript η in Eq.(2.7). The parameters that are important at this small scale is the rate at which the energy is received from the large scales, ε, and the kinematic viscosity ν. From dimensional analysis using these two parameters the Kolmogorov length scale ℓ_η, velocity scale u_η and time scale τ_η can be defined:

$$\ell_\eta \equiv \left(\frac{\nu^3}{\varepsilon}\right)^{\frac{1}{4}}, \qquad u_\eta \equiv (\nu\varepsilon)^{\frac{1}{4}}, \qquad \tau_\eta \equiv \left(\frac{\nu}{\varepsilon}\right)^{\frac{1}{2}} \tag{2.7}$$

The Reynolds number based on the Kolmogorov scales is unity, $\mathrm{Re}_\eta = \ell_\eta u_\eta/\nu = 1$. This is consistent with the notion that viscosity plays a dominant roles at the small scale turbulence.
The ratios between the smallest and largest scales are determined from the Kolmogorov scales (Eq. (2.7)) and the energy dissipation scale (Eq. (2.5)). This results in:

$$\frac{\ell_\eta}{\ell_0} \sim \mathrm{Re}_0^{-\frac{3}{4}}, \qquad \frac{u_\eta}{u'} \sim \mathrm{Re}_0^{-\frac{1}{4}}, \qquad \frac{\tau_\eta}{\tau_0} \sim \mathrm{Re}_0^{-\frac{1}{2}} \tag{2.8}$$

This shows that the difference between the small scales and the large scales grows as the turbulent Reynolds number increases.

2.1.3. Mean velocity profile turbulent pipe flow

The fluid motion near the wall is decelerated until it is zero at the wall due to friction. This is referred to as the no-slip boundary condition and leads to the formation of boundary layers. The mean velocity profile of a turbulent boundary layer can be divided into three regions: core region, the logarithmic wall layer and the viscous sublayer. In the core region the turbulent shear stress dominates. In the logarithmic wall region the turbulent stress dominates and reaches a nearly constant value. In the transition region between the logaritmic wall layer the turbulent shear stress drops and the viscous shear stress increases, which is also called the buffer layer. In the viscous sublayer viscous shear dominates.

Turbulent mean velocity profiles are generally described with the so called dimensionless wall distance [60]:

$$y^+ = \frac{\rho u_\tau y}{\mu} \tag{2.9}$$

and the dimensionless mean velocity:

$$u^+ = \frac{\bar{u}}{u_\tau}, \tag{2.10}$$

where $u_\tau = \sqrt{\tau_w/\rho}$ is the friction velocity based on the wall shear stress τ_w. The mean velocity profile of a turbulent boundary layer is visualized in Figure 2.3 and can be described by [50]:

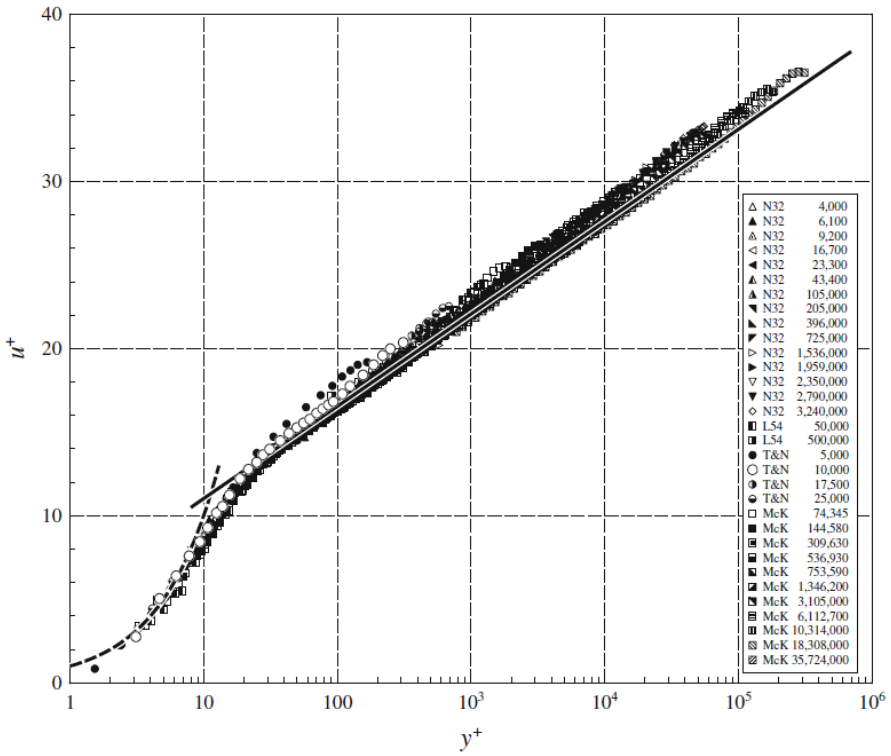

Figure 2.3: The dimensionless mean velocity profile u^+ as a function of the dimensionless wall distance y^+ for turbulent pipe flow with Reynolds numbers between $4 \cdot 10^3$ and $36 \cdot 10^6$. The solid line (——) corresponds to the logarithmic profile in 2.12; the dashed line (−−−) corresponds to the linear profile in 2.11. Adopted from Nieuwstadt et al. [50].

- **Viscous sublayer** ($y^+ \leq 5$): This is the region where viscosity dominates and the mean velocity is given by:

$$u^+ = y^+. \tag{2.11}$$

- **Buffer layer** ($5 < y^+ < 30$): This is the transition region between the viscosity dominated and the turbulence dominated parts of the flow. No simple solution exists here.

- **Logaritmic wall layer** ($y^+ > 30$): In this region the logarithmic law-of-the-wall describes the flow:

$$u^+ = \frac{1}{K} \ln y^+ + C^+, \tag{2.12}$$

  where K is the von Kármán constant with the approximate value $K \approx 0.4$ and C^+ is additive constant which depends on the wall roughness; for a smooth pipe wall $C^+ = 5$.

- **Core region**: The logarithmic law-of-the-wall cannot describe the mean velocity profile at the centreline of the pipe, because there the derivative of Eq. 2.12 $\neq 0$. In the core region the mean velocity profile is given by:

$$u^+ = u_0 - \frac{2}{3} \frac{u_\tau}{\beta} \left(1 - \frac{r}{d}\right)^{\frac{3}{2}}, \tag{2.13}$$

  where u_0 is an integration constant that represents the centreline velocity of the pipe, β is an experimental value and is about 0.13 for turbulent pipe flow.

2.2. Laminar premixed combustion

In premixed combustion the fuel and oxidizer (usually air) are mixed before they enter the combustion chamber. This combustible mixture is ignited in the combustion chamber. For a premixed flame, it is possible to vary the ratio between the fuel and air. The ratio between the fuel and air is used to control the flame temperature. A fuel-air mixture that is combusted with an excess or a shortage of air has a lower flame temperature than a mixture with the right amount of air needed to completely combust the fuel. Premixed combustion is used in gas turbines, since a lower flame temperature leads to a smaller amount of NO_x in the exhaust gases. A ratio that is commonly used to characterize the fuel-to-air ratio is the equivalence ratio ϕ, which is defined as the actual fuel-to-air ratio divided by the stoichiometric fuel-to-air ratio:

$$\phi = \frac{Y_{F,u}/Y_{air,u}}{(Y_{F,u}/Y_{air,u})_{\text{st}}}, \tag{2.14}$$

where, $Y_{F,u}$ and $Y_{air,u}$ denote the mass fraction of the fuel and oxidizer in the unburned mixture. The subscript 'st' stands for stoichiometric conditions, where the fuel and the air are completely burnt. The combustible mixture can be adjusted from rich ($\phi > 1$) over stoichiometric ($\phi = 1$) to lean ($\phi < 1$). The structure of the premixed flame and the relevant parameters are discussed in the following sections.

2.2.1. Flame structure

The structure of a one-dimensional laminar premixed flame is shown in Figure 2.4. This structure assumes a one-step chemical reaction with high activation energy. Two different regions can be distinguished: the preheat zone and the reaction zone [44]. The thickness of these zones are denoted in Figure 2.4 as δ_{ph} and δ_r, respectively. Starting on the left side of Figure 2.4, the fuel and the oxidizer are convected downstream into the preheat zone with a speed equal to the laminar flame speed, denoted as $u_u = s_{l,0}$. The laminar flame speed is much smaller than the speed of sound, so the combustion process can be assumed to be isobaric [44]. The combustible mixture can be characterised by an equivalence ratio ϕ, and a density ρ_u which depends on temperature T_u and pressure p_u. Within the preheat zone no combustion takes place. The mixture diffuses into the reaction zone and is heated up by the heat conducting from the reaction zone. These diffusion processes are captured by the Lewis number, which is defined as:

$$\text{Le} = \frac{\alpha}{D} = \frac{\lambda}{c_p \rho D}, \tag{2.15}$$

where α and D are the heat and mass diffusion of the mixture respectively. The heat diffusion α can be written in terms of the thermal conductivity λ, specific heat capacity c_p and density ρ of the mixture. When Le≠1, the heat and mass diffusion are not equal and this leads to sub- or superadiabatic flame

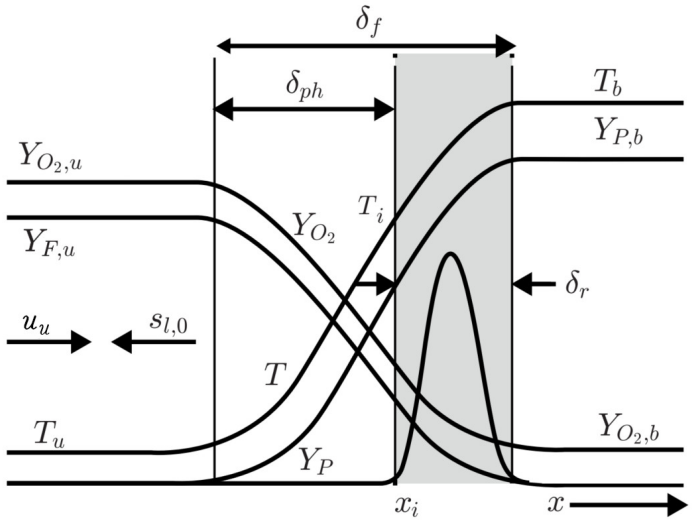

Figure 2.4: Schematic temperature and concentration profiles for a stationary and one-dimensional laminar flame. This schematic is based on one-step kinetics and considers a lean mixture. Based on figure from Peters [53].

temperatures and to the thermal-diffusive instability as will be discussed in Sections 2.3.2 and 2.4.2. Again moving with the mixture from the preheat zone to the reaction zone, the mixture will eventually reach the ignition temperature and rapid chemical reaction will take place [47]. In the case of a stoichiometric fuel-air mixture, both the fuel and the oxidizer will be completely depleted. In the particular case of Figure 2.8 the burned mixture still contains some oxygen. This is due to the fact that unburned mixture is lean, which means that the mass fraction ratio $Y_{air,u}/Y_{F,u}$ is higher than the stoichiometric mass fraction ratio $(Y_{air,u}/Y_{F,u})_{st}$, see Eq.(2.14). The mixture with the reaction products $Y_{P,b}$ is then convected downstream with a burned gas temperature T_b. The burned gas temperature is equal to the adiabatic flame temperature T_{ad} when no heat loss is assumed.

The preheat zone and the reaction zone are characterised by two different lengths, δ_{ph} and δ_r respectively, where $\delta_r << \delta_{ph}$ [47]. The flame thickness is therefore associated with $\delta_f \approx \delta_{ph}$. It is difficult to measure the flame thickness and different definitions for the flame thickness can be found in the literature [27].
For the one-dimensional flame, the continuity equation reads:

$$\frac{d(\rho u)}{dx} = 0, \tag{2.16}$$

where u is the flow velocity and x is the coordinate in the flow direction. This means that the mass flux through the flame is constant and the velocity increase across the flame front can be determined from

$$u_b = \frac{\rho_u}{\rho_b} u_u, \tag{2.17}$$

where the subscripts u and b refer to unburned and burned conditions, respectively. The density ratio of the unburned gas and burned gas is often described by a single parameter $\sigma = \rho_u/\rho_b$. This ratio is also important in determining the pressure difference over the flame. The pressure field of an one-dimensional flame is obtained via the continuity equation of Eq.(2.16) and momentum conservation equations over the flame. The momentum conservation equation is formulated as follows [44, 72]:

$$\rho_u (u_u)^2 + p_u = \rho_b (u_b)^2 + p_b, \tag{2.18}$$

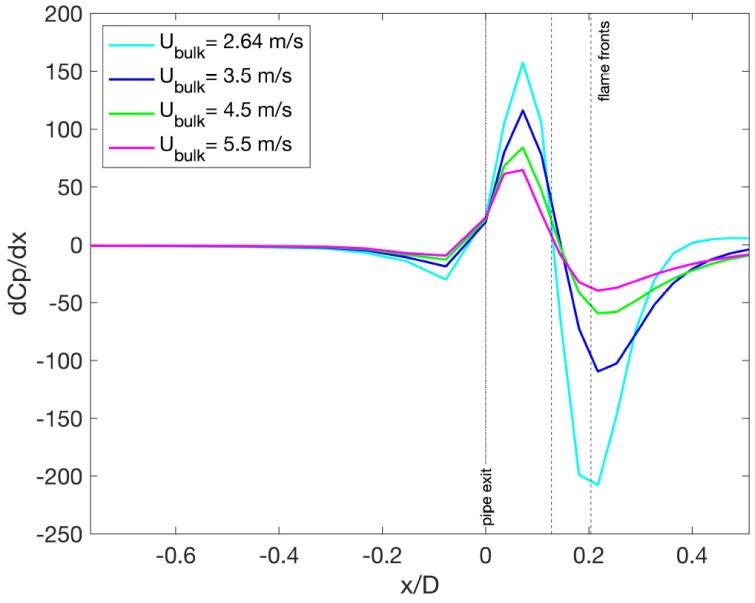

Figure 2.5: Pressure distribution through four different flame fronts, where on the vertical axis the gradient of the pressure coefficient $C_p = \frac{p(x)-p_0}{1/2\rho U_b}$ is used. p_0 is defined as the pressure equal to zero. Before the flame front the pressure gradient increases, and it decreases trough the flame front. The flame fronts are between the two vertical lines at $0.12 < x/D < 0.2$. Adopted from van Put [66].

where p denotes the pressure. Combining Eq.(2.17) and Eq.(2.18) and assuming that the velocity of the unburned mixture is equal to the laminar flame speed $u_u = s_l$, leads to the pressure difference over the flame, which is also referred to as the backpressure of a premixed flame:

$$\Delta p = p_u - p_b = \rho_u s_l^2 \left(\frac{\rho_u}{\rho_b} - 1 \right). \tag{2.19}$$

It stands for the pressure that is required to accelerate the unburned gas velocity to the burned gas velocity. For turbulent flames, the laminar flame speed s_l in Eq. (2.19) is replaced by the turbulent flame speed s_t [17, 37]. A typical pressure distribution through a flame front can be seen Figure 2.5. On the vertical axis the gradient of the pressure coefficient $C_p = \frac{p(x)-p_0}{1/2\rho U_b}$ is used, where p_0 is defined as the pressure equal to zero. It can be seen that the pressure gradient increases in front of the flame and decreases sharply through the flame front. This phenomenon leads to the hydrodynamic instability and plays an important role in flame flashback as will be discussed in Section 2.4.1.

2.2.2. Laminar flame speed

The laminar flame speed is a fundamental property for premixed flames. It is determined by the chemical kinetics and depends on the initial conditions of the fuel-air mixture. The equivalence ratio ϕ and the mixture composition have a significant influence on the flame speed as can be seen in Figure 2.6. For mixtures with Le ≈ 1 like CH_4-air, the flame speed peaks at stoichiometric conditions ($\phi = 1$) and decreases for off-stoichiometric conditions ($\phi < 1$ or $\phi > 1$), see Figure 2.6a. When comparing Figure 2.6a to Figure 2.6b, it can be seen that the flame speed of the H_2-air mixture is much higher. Furthermore, the peak of the flame speed is shifted to $\phi = 1.75$. This has to do with the high diffusivity of hydrogen, which will be explained in Section 2.3.2. Another important factor that influences the flame speed is the temperature of the unburned mixture. In general, the higher the temperature of the unburned mixture, the higher the flame speed [44].

There are several techniques to measure the laminar flame speed, for example: the Bunsen flame method, the flat and one-dimensional flame method, and the outwardly propagating spherical flame method [44]. Here, only the Bunsen flame method will be discussed as in this investigation a type of Bunsen burner is used. A Bunsen burner consists of a tube where fuel and air enter from below and are mixed such that at the tube outlet a premixed flame can be established. Under steady conditions this flame has a characteristic conical shape as can be seen in Figure 2.7b. In Figure 2.7a the kinematic balance is shown between the flow and the flame. The laminar flame speed s_l is defined as the velocity component normal to the flame front with respect to the unburned mixture. If the velocity of the mixture at the tube exit and the cone angle α_u can be determined via experiments, one can obtain the laminar flame speed via:

$$s_l = u_u \sin \alpha_u. \tag{2.20}$$

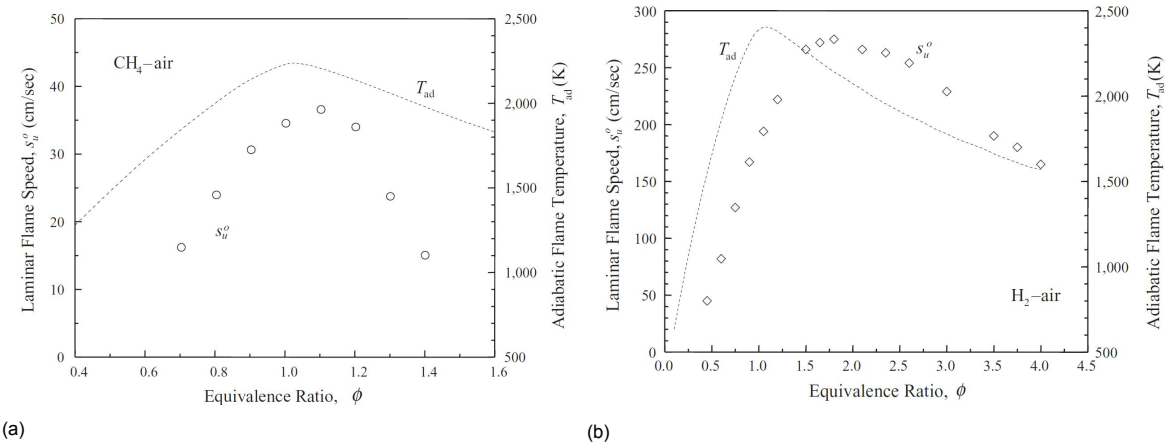

Figure 2.6: Calculated adiabatic flame temperatures and measured laminar flame speeds at atmospheric pressure of **(a)** CH_4-air and **(b)** H_2-air mixtures. The flame speed of the H_2-air flame is much higher than the CH_4-air flame. Adopted from Law [44].

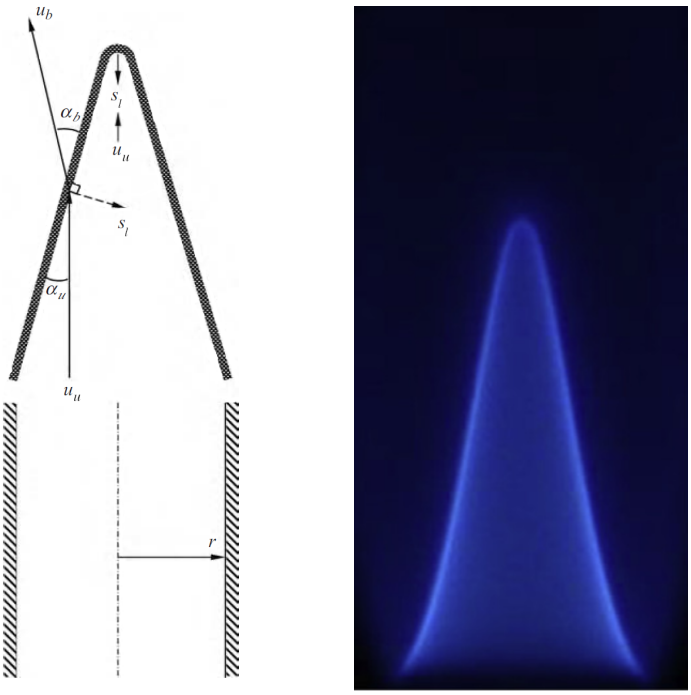

(a) (b)

Figure 2.7: **(a)** Kinematic balance of an laminar Bunsen flame. Adopted from Law [44]. **(b)** Image of a premixed laminar Bunsen flame with the characteristic conical shape. Adopted from Wei et al. [69].

If the flame tip is closed as shown in Figure 2.7, it can be seen that the flame front and the flow are perpendicular to each other, i.e $\alpha_u = \pi/2$. This means that at the flame tip the flame speed is a factor $1/\sin\alpha_u$ higher than the oblique part of the flame. As will be discussed in Section 2.3.2, this is due the strong influence of the flame front curvature. The increase of flame speed at the flame tip holds for mixtures with Le> 1 (for example CH_4-air). However, the opposite is true for mixtures with Le< 1 (for example lean H_2-air). For these mixtures the flame speed at the flame tip will be lower, which can lead to a phenomenon called flame tip opening [44]. The Bunsen flame method can also be used to estimate the flame speed of turbulent flames. When the time-averaged turbulent flame is considered, the cone angle can be determined [38, 54].

2.3. Flame stretch

The flame description in Section 2.2.1 is an idealization. In reality, the flame front is often curved and stretched, which is in particular the case for turbulent flames where the turbulence has a significant effect on the flame structure as will be discussed in Section 2.5. Curvature and stretch can have an influence on the flame speed [14, 44, 47], which will be discussed in the following sections.

2.3.1. Mathematical expressions for flame stretch

A general definition of the flame stretch rate at any point on the flame surface area A is given by:

$$\mathbb{K} = \frac{1}{A}\frac{dA}{dt}, \tag{2.21}$$

which is the Lagrangian time derivative of the logarithm of the area A of an infinitesimal element of the surface and has the unit of s^{-1}. This simple expression contains various factors that contribute to the flame stretch rate. Globally, two different phenomena are distinguished:

$$\mathbb{K} = \mathbb{K}_c + \mathbb{K}_s, \tag{2.22}$$

where $\mathbb{K}_c$ and $\mathbb{K}_s$ are the flame stretch rates due to flame curvature and flow straining, respectively. The $\mathbb{K}_c$ term contains the sum of the inverse radii of curvature. Both radii of curvature are negative when the flame sheet is concave towards the unburned gas [72] and thus the Bunsen flame on the left side of Figure 2.8, also depicted in Figure 2.7, is negatively stretched. The opposite is true for a flame with a convex flame front towards the reactants. An example of stretch due to flow straining can be seen on the right side of Figure 2.8. The flame is outwardly and thus positively stretched by the fluid motion due to the tangential velocity gradient.

2.3.2. Flame stretch phenomenon

In the previous section a mathematical expression for the flame stretch has been provided to distinguish different mechanisms leading to positive or negative stretch. Now the effects of stretch on a flame will be discussed. It has been found that the effects of flame stretch are especially strong for mixtures with different mass and thermal diffusivities (i.e. when Le$\neq$ 1) [44]. To analyse these effects, a distinction is made between three diffusivities: the thermal diffusivity, α, the mass diffusivity of the fuel, D_F, and the mass diffusivity of the oxidizer, D_{Ox}. These three diffusivities are captured by the Lewis number, $Le = \alpha/D$, (where D is often taken as the diffusivity of the deficient reactant) and by the mass diffusivity ratio (D_F/D_{Ox}) [47].

The unstretched one-dimensional premixed flame, discussed in Section 2.2.1, has aligned convective and diffusive fluxes. Considering a control volume enclosing the area between two streamlines and the preheat zone of the flame as depicted in Figure 2.8, the aligned fluxes cause the control volume to be adiabatic assuming no external heat loss. Therefore, the flame temperature of the unstretched premixed flame is equal to the adiabatic flame temperature, T_{ad}.

Now consider the two different types of stretched flames depicted in Figure 2.8. The curved flame on

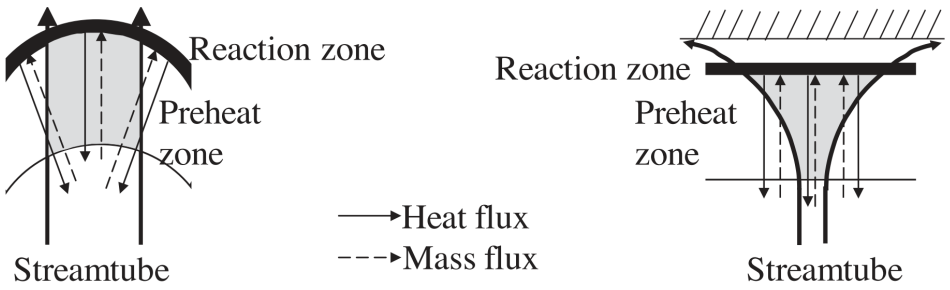

Figure 2.8: Schematic illustration of two different types of stretched flames. The left Bunsen flame is stretched due to curvature, the right stagnation flame due to flow straining. The grey area is the control volume and the misaligned fluxes are also shown. Adopted from Lieuwen [47].

the left is stretched due to curvature and the stagnation flame on the right due to flow straining. The thermal and mass diffusion fluxes are normal to their corresponding isosurface. It can be be seen that the curved flame on the left, also referred to as the tip of the Bunsen flame, has misaligned convective and diffusive fluxes. The curvature of the flame has a diverging effect on the mass fluxes. This reduces the concentration of the deficient species approaching the flame and thus the chemical energy, which leads to a flame temperature below T_{ad} and a lower mass burning rate. On the other hand, the heat fluxes are converged due to the curvature of the flame. This increases the thermal energy within the control volume, leading to a flame temperature above T_{ad} and a higher mass burning rate. So the flame temperature and the burning rate depends on the balance between the thermal and mass diffusivities. If the thermal and mass diffusivities are in balance, i.e. $Le \approx 1$ (stoichiometric natural gas-air mixture), then the effects cancel out. However, when $Le > 1$ (C_3H_8-air mixture), the net energy flux into the control volume is positive, leading to a higher flame temperature and burning rate. When $Le < 1$ (H_2-air mixture), the net energy flux is negative and leads to a decrease in flame temperature and mass burning rate. Note that the opposite is true for a flame that is curved in the opposite direction. This configuration has similar effects due to stretch as the stagnation flame depicted on the right side of Figure 2.8.
Next, the effects due to differential diffusion are considered. If the left flame in Figure 2.8 burns with a lean H_2-air mixture, both the H_2 and the O_2 diffuse through the sides of the control volume. However, H_2 is much lighter than O_2 and therefore has a higher mass diffusion. This leads to a higher net loss of H_2 in the control volume compared to O_2. The mixture entering the reaction zone in the control volume is therefore leaner compared to the approaching mixture flow in front of the control volume. As a consequence, the flame temperature and the burning rate decrease. Opposite behavior occurs when the mixture is rich. Then the higher mass diffusion of H_2 is causing the rich mixture to move to more stoichiometric conditions, leading to a increase in flame temperature and burning rate. The preferential diffusion effects described above are exactly the opposite for flames curved the other way around and for fuels that are heavier than air, for example, C_3H_8.

The effects of stretch described above can also be applied to turbulent flames when the laminar flame thickness is larger than the smallest turbulent eddy size [44, 56]. This will be explained in Section 2.5.

2.3.3. Weak flame stretch effects

In the previous sections, it was shown that curvature and nonuniform flow have an influence on the flame temperature and mass burning rates. If the flame is stretched, the flame speed may take different values and it is difficult in both experiments and numerical studies to determine the exact value. The only theoretical basis for the stretched flame speed comes from asymptotic analyses [56]. These asymtpotic analyses are based on high activation, one-step kinetics and suggest that when the flame is weakly stretched, the stretch $\mathbb{K}$ is the only parameter that controls the flame structure and describes the sensitivity of a flame to stretch through a linear relationship:

$$s_l = s_{l,0} - \mathcal{L}_{M,u}\mathbb{K}, \tag{2.23}$$

where $\mathcal{L}_{M,u}$ is the Markstein length. All the speeds are defined on the unburned side. The last term in Eq. (2.23) is often written in terms of two normalized numbers, namely the the normalized flame stretch sensitivity, called the Markstein number Ma_u:

$$\mathrm{Ma}_u = \frac{\mathcal{L}_{M,u}}{\delta_f} \tag{2.24}$$

and the normalized stretch rate, which is called the Karlovitz number $\mathrm{Ka}_{\mathbb{K}}$:

$$\mathrm{Ka}_{\mathbb{K}} = \frac{\delta_f \mathbb{K}}{s_{l,0}}, \tag{2.25}$$

The Markstein number contains the stretch effects that are described in Section 2.3.2, i.e. $\mathrm{Ma}_u = \mathrm{Ma}_u(\mathrm{Le}, D_F/D_{Ox}, \phi, ...)$. Different expressions for the Markstein number can be found in literature [13, 44, 56, 63] and it is important to note that the values of the Markstein number are sensitive to the position at which the flow and the flame speeds are measured [47]. Although the exact values may differ in literature, the result of a negative or positive Markstein number can be described. For a lean

mixture with a fuel that is lighter than air, e.g. H_2 and for a rich mixture with a fuel heavier than air, e.g. C_3H_8, Ma_u <0 [63]. For a lean mixture with a fuel heavier than air and for a rich mixture with a fuel lighter than air, Ma_u >0 [47]. For a flame that is negatively stretched ($Ka_{\mathbb{K}} << 0$), e.g. a Bunsen flame, the negative and positive Markstein number corresponds to a decrease or increase in flame speed respectively and this result is expected from the differential diffusion effects analysed in Section 2.3.2. It is emphasized that the above equations only hold for weak stretch, i.e. $|Ka_{\mathbb{K}}| << 1$ [47, 56]. For turbulent flames in which often high stretch rates are encountered, the equations above are not valid.

2.4. Flame front instabilities

Premixed flames have intrinsic flame front instabilities that can be distinguished in three different groups [44, 72]: Body-force or buoyancy-driven instabilities, hydrodynamic instabilities and thermo-diffusive instabilities. The hydrodynamic and thermal-diffusive instabilities are the primary instability mechanisms in Bunsen flames and will be explained in Section 2.4.1 and 2.4.2 respectively.

2.4.1. Hydrodynamic flame instability

The hydrodynamic instability, also called the Darrieus-Landau instability, is related to the interaction between the flame and the flow. The flame is assumed to be infinitely thin and can therefore be seen a surface of density discontinuity. This flame surface separates the unburned region with constant density ρ_u from the burned region with constant density ρ_b and is assumed to propagate with the constant laminar flame speed $s_{l,0}$. To analyse the stability of a flame that is wrinkled, Lieuwen [47] performed a linearized analysis that captured the coupling between the flame and the flow field. The obtained solution can be seen in Figure 2.9. An important result from the analysis is the effect of the flame bulge that is convex to the unburned mixture. It causes the streamlines of the approach flow to diverge and decelerates the flow in front of the flame wrinkle. This goes together with an adverse pressure gradient as can be seen in Figure 2.9b. The opposite occurs when the flame bulge is concave to the unburned mixture. As stated before, the flame speed is assumed to remain constant. This results in an imbalance between the local flow and flame velocity. The convex bulge of the flame will propagate further into the unburned mixture, while the concave flame bulge propagates further into the burned mixture. The initial perturbation is therefore enhanced and the flame is unstable. The effect of the convex flame bulge plays an important role flame flashback, because the leading edge of the flame must be oriented this way when it penetrates into the unburned mixture [47].

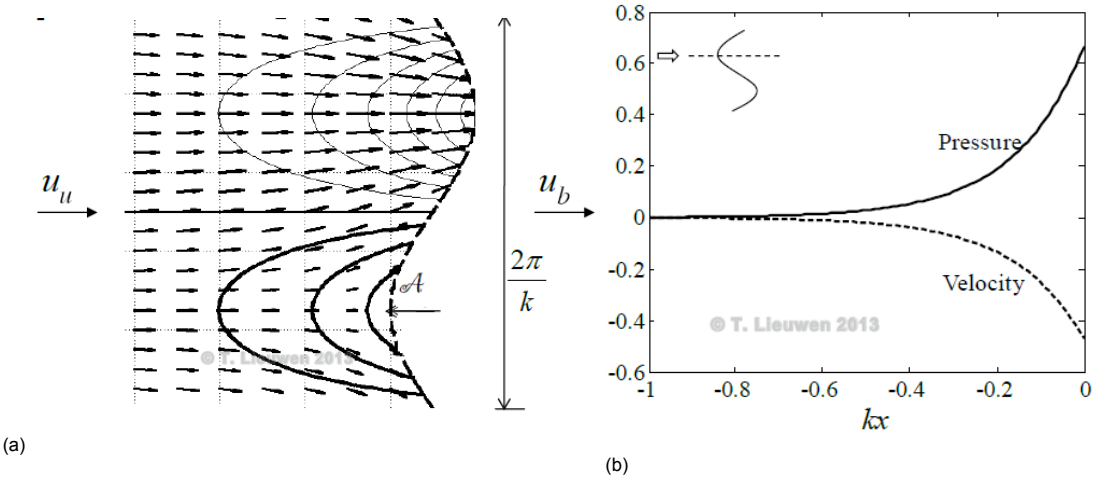

(a) (b)

Figure 2.9: Illustration of the hydrodynamic flame instability showing the flame-flow interaction. **(a)** The effect of convex and concave flame bulges on the incoming flow. The thick and thin lines are isobars and correspond to a positive and negative pressure fluctuation respectively. **(b)** Illustration of the normalized pressure and velocity in front of a convex flame bulge into the reactants. Although not shown, the opposite occurs for a concave flame bulge into the reactants. Adopted from Lieuwen [47].

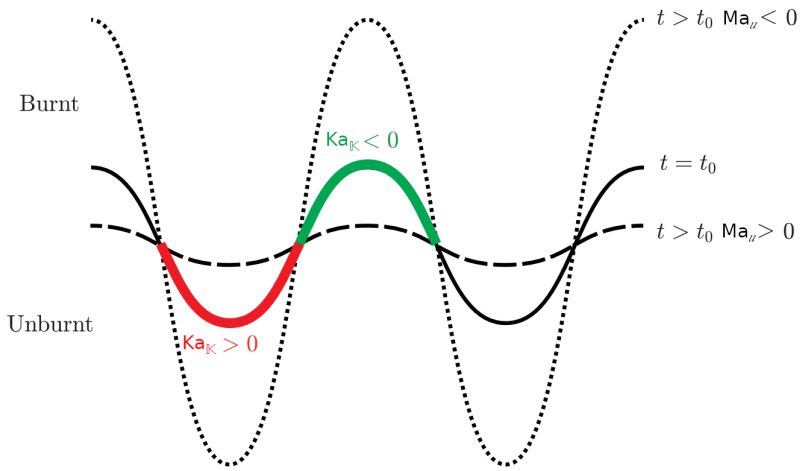

Figure 2.10: Schematic illustration of the thermal-diffusive instability. The amplitude of a perturbation of the flame front at $t = t_0$ is either decreasing ($\mathrm{Ma}_u > 0$) or increasing ($\mathrm{Ma}_u < 0$). Adopted from Faldella [28].

2.4.2. Thermal-diffusive flame instability

Nonequidiffusion plays an important role in the stability of a flame. The thermal-diffusive instability covers the combined effect of a non unity Lewis number and differential diffusion [47, 72]. As already discussed in Sections 2.3.2 and 2.3.3, fuel-air mixtures with unequal diffusion fluxes cause changes in the flame speed when the flame is wrinkled. Consider a flame front that is initially ($t = t_0$) perturbed by a harmonic wave in a uniform flow field, see Figure 2.10. The flame front consists now of convex and concave bulges with respect to the flow direction which leads to positive and negative stretch. For a fuel-air mixture with a positive Markstein number ($\mathrm{Ma}_u > 0$), the flame speed increases and decreases when the flame front is respectively negatively ($\mathrm{Ka}_{\mathbb{K}} < 0$) and positively ($\mathrm{Ka}_{\mathbb{K}} > 0$) stretched according to the Eqs. (2.23 - 2.25). This leads to an inward movement of the initial bulges at $t > t_0$ and eventually the harmonic wave is damped. It has therefore a stabilizing effect on the flame front. Most hydrocarbon fuels have this stabilizing property. However, this is not true for a lean H_2-air mixture. Such a mixture is characterised by a negative Markstein number ($\mathrm{Ma}_u < 0$). This lead to growth of the initial bulges of the flame and therefore destabilizes the flame front. Both of these mechanisms are visualized in Figure 2.10.

2.5. Turbulent premixed combustion

Most industrial gas turbines use turbulent combustion in their combustor. They operate in this way, because turbulence enhances mixing, thereby increasing the mass consumption rate of the reactant mixture. The increased mass consumption rate leads to a higher chemical heat release rate and thus to a higher power output [33]. So in contrast to laminar flow, turbulent flow interacts with the reaction chemistry. A flow field which is turbulent interacts with a flame. In the following sections, the effect of turbulence on the flame will be discussed in more detail.

2.5.1. Flame regimes

In the previous sections the time and the length scales of turbulent flow are described. These scales are important to describe the effect of turbulence on a flame front. Figure 2.11 shows the interaction of turbulent eddies with a flame front. The turnover velocity of a turbulent eddy, denoted with u', is an important parameter for the interaction of an eddy with a flame front. Only eddies with a larger turnover velocity than the laminar flame speed can push the flame front around, leading to wrinkles in the flame front, see figure 2.11a. In addition, the size of an eddy is important. As discussed in Section 2.1.2 the size of the smallest eddy in the flow depends on the turbulent Reynolds number. If the turbulent Reynolds number is very large, the size of the smallest eddies can be on the order of the flame thickness δ_f. As Figure 2.11b shows these eddies can penetrate into the preheat zone of a flame and advect the preheated material, which enhances mixing. To distinguish different flame regimes that occur in turbulent combustion, the turbulent scales are compared to chemical and laminar flame scales. For laminar flames, the following characteristic flame length and times scale are applied [54]:

$$\delta_f = \frac{D}{s_l}, \qquad \tau_f = \frac{D}{(s_l)^2}, \tag{2.26}$$

where δ_f is also referred to as the laminar flame thickness and D is the mass diffusivity of the mixture. If the Schmidt number $\mathrm{Sc} = \nu/D$ of unity is assumed, then the turbulent Reynolds number defined in Section 2.1.2 can be compared to the laminar flame scales as:

$$Re_0 = \frac{u'\ell_0}{\nu} = \frac{u'}{s_l}\frac{\ell_0}{\delta_f}, \tag{2.27}$$

The effect that turbulence has on the structure of the flame front is determined by the scales of the eddies in the flow. In the classical approach, flame stretch in turbulent flow in terms of flow straining is

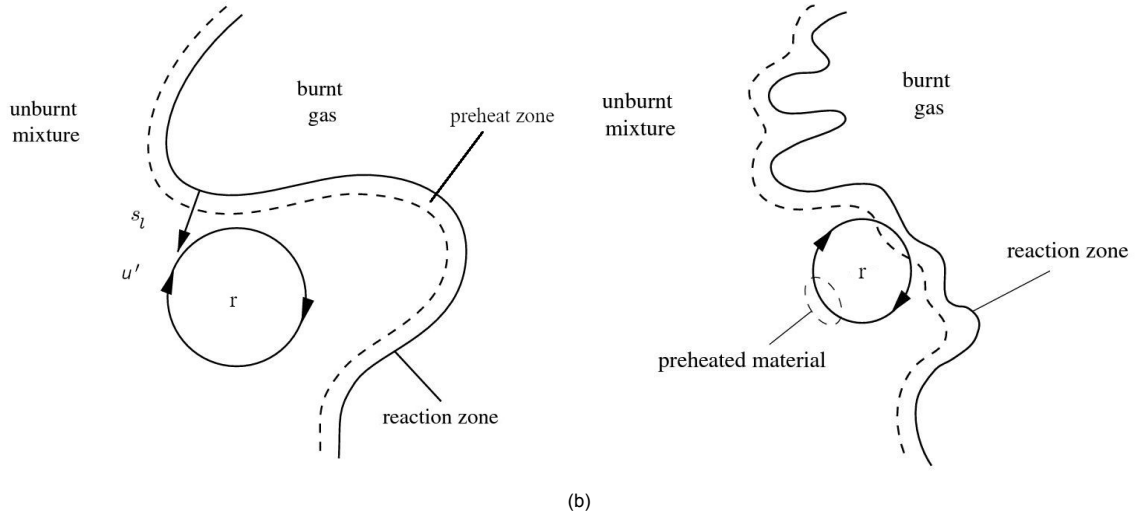

Figure 2.11: **(a)** Interaction of a turbulent eddy with a flame front front. The eddy has a turnover velocity u' equal to the laminar flame speed s_l and is able to wrinkle the flame front. **(b)** Interaction of a small turbulent eddy with a flame front. The eddy is able to advect the preheated material in front of the flame. Based on figures from Peters [54].

estimated by [56]:

$$\mathbb{K}(r) = \frac{u'(r)}{r} \tag{2.28}$$

where r is the size of an eddy. The characteristic time scale of an eddy with size r is:

$$\tau(r) = \frac{r}{u'(r)} = \frac{1}{\mathbb{K}(r)}. \tag{2.29}$$

This implies that eddies with a Kolmogorov length scale induce the highest stretch on the flame. However, the Kolmogorov eddies have also the shortest life time τ_η and thus the actual effect on the flame front is not clear. It is still unsolved which turbulent eddies are the most relevant in determining the flame structure [56]. Nevertheless, the classical approach uses the Kolmogorov scales to describe the dominant flame structure in a turbulent flow.
Therefore, two turbulent Karlovitz numbers are defined as a parameter to determine whether the laminar flame structure can be sustained in a turbulent flow. The first Karlovitz number compares the laminar flame scales with the Kolmogorov scales:

$$\mathrm{Ka} = \frac{\tau_f}{\tau_\eta} = \left(\frac{\delta_f}{\ell_\eta}\right)^2 = \left(\frac{u_\eta}{s_l}\right)^2. \tag{2.30}$$

The second Karlovitz number is a parameter of the effect that turbulence has on the reaction zone of a flame and therefore compares the reaction zone scales to the Kolmogorov scales:

$$\mathrm{Ka}_r = \frac{\tau_r}{\tau_\eta} = \left(\frac{\delta_r}{\ell_\eta}\right)^2. \tag{2.31}$$

According to Peters[54] and Law [44] five different flame regimes can be distinguished, which can be seen in the Borghi diagram of Figure 2.12:

- **Laminar flame regime** ($\mathrm{Re}_0 < 1$): In this flame regime, the intensity of turbulence is weak, so the flow can be called laminar. The flame can be wrinkled to a minimum extent.
- **Wrinkled flamelet regime** ($\mathrm{Re}_0 > 1$, $\mathrm{Ka} < 1$, $u' < s_l$): In this flame regime, Ka< 1, which means that the flame thickness is much smaller than the smallest turbulent scale. The flame can therefore retain its laminar flame structure and is described as a locally laminar premixed flame embedded in a turbulent flow [68]. The only the effect of turbulence can be seen in the wrinkling of the flame. This can be seen in images (a) and (b) of Figure 2.13.

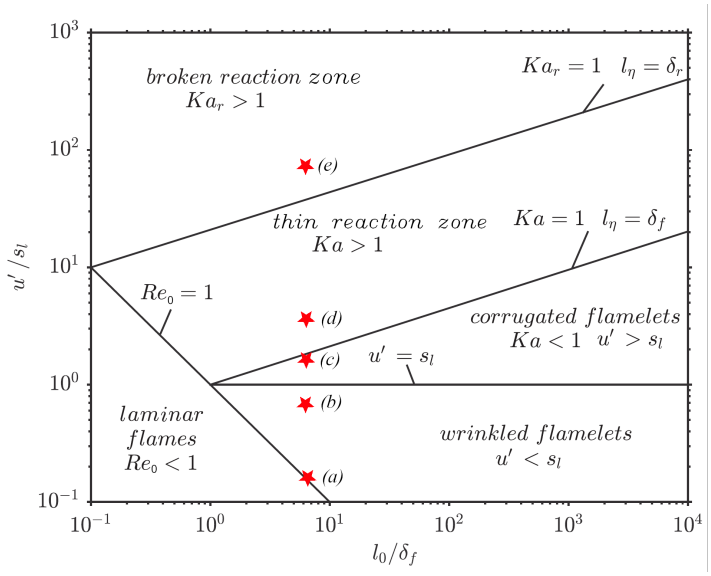

Figure 2.12: Borghi diagram showing the different modes in turbulent premixed combustion. The stars denote the flames with different flame regimes that are simulated by Aspden et al. [10] as can be seen in Figure 2.13.

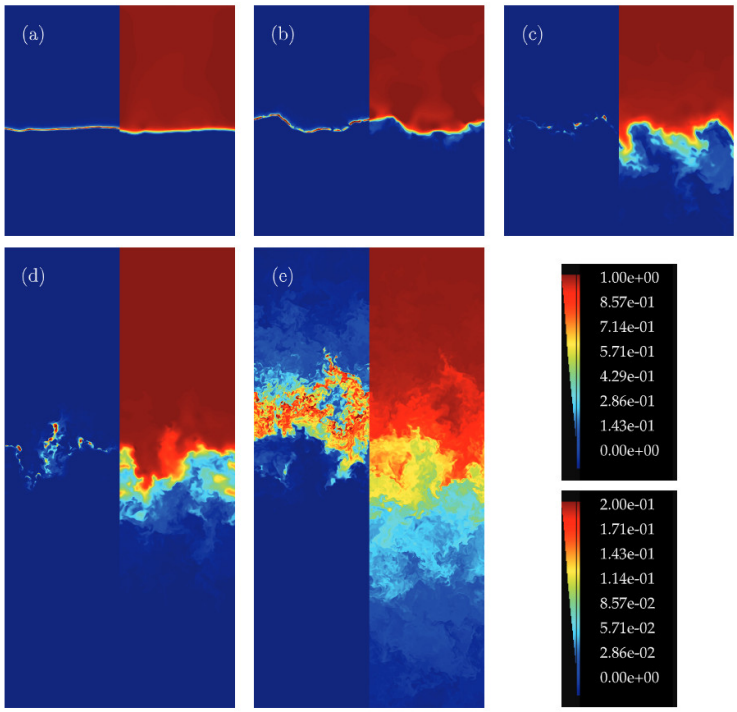

Figure 2.13: Instantaneous vertical slices through five different flames. The left-hand side of each figure shows the fuel consumption rate, normalized by the corresponding laminar value (except for case (e), which was normalized by one-fifth of the laminar value because it burns much less intensely than the laminar flame). The right-hand side of each figure shows the temperature field, again normalized by the laminar value. The top legend shows the range for each normalized value except the fuel consumption rate in case (e), which is shown by the lower legend. The corresponding flame regimes can be seen in Figure 2.12. Adopted from Aspden et al. [10].

- **Corrugated flamelet regime** ($\mathrm{Re}_0 > 1$, $\mathrm{Ka} < 1$, $u' > s_l$): This flame regime is still below the upper boundary of $\mathrm{Ka} = 1$, so the flame can still retain its laminar structure. But now the turbulence intensity is higher than the laminar flame speed. Consequently, the flame becomes highly wrinkled when it interacts with a turbulent eddy, which can be seen in in Figure (c) of Figure 2.13. It is being thought of that this wrinkling leads to island formations of burned and unburned mixtures.
- **Thin reaction zone** ($\mathrm{Re}_0 > 1$, $\mathrm{Ka} > 1$, $\mathrm{Ka}_r < 1$): In this regime the smallest turbulent eddies are comparable or smaller than the laminar flame thickness, but much larger than the reaction zone. The eddies can therefore penetrate into the preheat zone, thereby enhancing the mass and heat transfer rates. The preheat zone loses its laminar structure and as a consequence the flame is thickened as can be seen in Figure (d) of Figure 2.13. The reaction zone, however, retains its structure although it is wrinkled by the eddies. Note that in this regime, the effects of flame stretch described in Section 2.3.2 can be applied when the mass and heat transfer rates in the preheat zone are largely affected by the smallest turbulent eddies.
- **Broken reaction zone or well-stirred reactor regime**($\mathrm{Re}_0 > 1$, $\mathrm{Ka}_r > 1$): In this regime, the turbulent eddies penetrate into the reaction zone, which enhances the heat transfer into the preheat zone. This leads to a sudden drop in flame temperature and consequently to extinction of the flame. The flame is even more broadened and a clear local structure of the flame cannot be observed, see Figure (e) of Figure 2.13.

The different flame regimes as described by the Borghi diagram are mostly based on dimensional analysis, where the length and time scales of the flow and flame are compared. Moreover, the combustion process is idealized as it assumes one-step kinetics, high activation energy, a Lewis number of unity, equal diffusivities of the reactants, and steady and spatially uniform characteristics [15]. The boundaries given in the Borghi diagram are therefore not fixed and can be modified when additional physics are considered. For example, the interaction of a turbulent eddy with a flame represents a disturbance

in the flame. This disturbance can lead to the growth of the hydrodynamic and the thermo-diffusive instabilities, which enhances flame wrinkling.

However, it is important to note that the exact effects of the hydrodynamic instability and the thermo-diffusive instability on turbulent premixed combustion are still objects of research. Several studies have shown that the hydrodynamic instability plays only a role in low turbulent intensity ($u'/s_{l,0} < 1$) and in regions where the flame thickness is much lower than the integral length scale ($\ell_0/\delta_f \gg 1$) [20, 49], which is the wrinkled flamelet regime. The thermo-diffusive instability seems to be effective in the wrinkled and corrugated regime and even in part of the thin reaction zone ($u'/s_{l,0} \gg 1$) [21, 48].

2.5.2. Turbulent flame speed

A challenge in turbulent premixed combustion is the determination of the flame speed, which is called the turbulent flame speed for modeling purposes. While the laminar flame speed is only a function of the diffusive reactive properties of the unburned mixture, the turbulent flame speed is much more complex, as turbulence is coupled with the combustion processes within the flame. In literature, many correlations for the turbulent flame speed have been derived [18]. A widely used theoretical expression is the one proposed by Damköhler. He distinguished only two different flame regimes: large scale and small scale turbulence. These regimes correspond to the corrugated flamelet regime and the thin reaction zone, respectively, described in Section 2.5.1.
In the wrinkled/corrugated flamelet regime, the turbulent eddies are larger than the flame thickness. The flame retains therefore its laminar structure, but due to wrinkling the surface area of the flame increases as is visualised in Figure 2.14. Damköhler equated the mass flux through the increased flame surface area A_t to the mass flux through the flow cross-sectional area:

$$\dot{m} = \rho_u s_l A_t = \rho_u s_t A, \tag{2.32}$$

where the laminar flame speed is used perpendicular to the increased flame surface area and the turbulent flame speed is associated with the cross-sectional area of the incoming flow. This leads to the ratio between the laminar and the turbulent flame speed:

$$\frac{s_t}{s_l} = \frac{A_t}{A}. \tag{2.33}$$

In determining the area ratio, Damköhler reasoned in analogy to the Bunsen cone geometry, that the area increase in the turbulent flow is proportional to turbulent velocity fluctuations leading to:

$$\frac{A_t}{A} \sim \frac{u'}{s_l}. \tag{2.34}$$

Combining Eq. (2.33) and Eq. (2.34) this leads to:

$$\frac{s_t}{s_l} \sim \frac{u'}{s_l}. \tag{2.35}$$

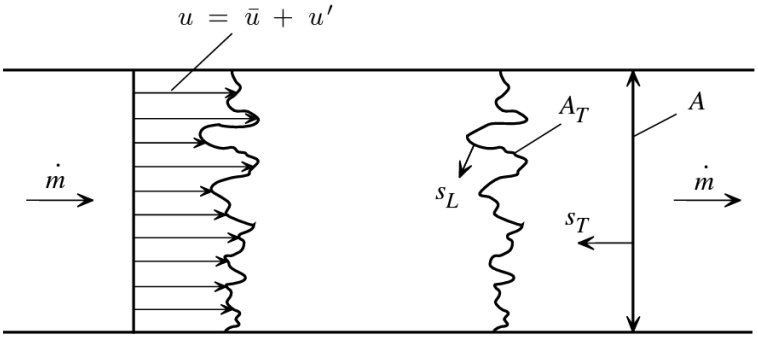

Figure 2.14: Illustration of the turbulent premixed flame front area used to define the turbulent flame speed. Adopted from Peters [54].

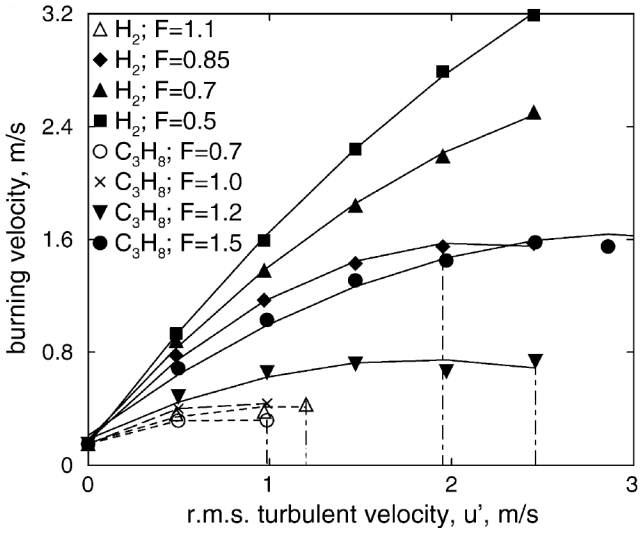

Figure 2.15: Effect of the thermal-diffusive instability in turbulent flow. By decreasing the equivalence ratio (F) the flame speed strongly increases for hydrogen (H_2). Adopted from Chomiak et al. [48]

From the flame geometry analysis by Law [44], this relation corresponds to a high turbulence intensity ($u'/s_l >> 1$), which is in the corrugated flamelet regime.
Since the preheat zone retains its laminar structure in the wrinkled/corrugated flamelet regime, the effects of flame stretch on the laminar flame speed can be applied here [44]. Figure 2.15 shows that the thermal-diffusive instability leads to a strong increase in flame speed for pure hydrogen even at high turbulent intensities.

In the thin reaction zone, the turbulent eddies are smaller than the laminar flame thickness. Therefore, the turbulent eddies affect the transport within the preheat zone. This is described by the turbulent diffusion D_t. According to Damköhler, the relation between the laminar and the turbulent flame speed can be described as:

$$\frac{s_t}{s_l} \sim \left(\frac{D_t}{D}\right)^{\frac{1}{2}}, \tag{2.36}$$

where D is the molecular diffusivity. This expression can also be rewritten using the fact that $D_t \sim u'\ell_0$ and $D \sim s_l\delta_f$:

$$\frac{s_t}{s_l} \sim \left(\frac{u'}{s_l}\frac{\ell_0}{\delta_f}\right)^{\frac{1}{2}} \sim Re_0^{\frac{1}{2}}. \tag{2.37}$$

This shows that for small scale turbulence the turbulent flame speed does also depend on the length scale ratio ℓ_0/δ_f.
A correlation based on Damköhler analysis that is widely used, is obtained by combining Eq. (2.35) and Eq. (2.37) [54]:

$$\frac{s_t}{s_l} = 1 + C\left(\frac{u'}{s_l}\right)^n, \tag{2.38}$$

where the value of n varies between 0.5 and 1. The constant C is expected to depend on the length scale ratio ℓ_0/δ_f. This expression also includes laminar flame propagation in the limit $u' \to 0$, where $s_t = s_l$.

3

Flame flashback

For safe and reliable operation of a gas turbine, it is required that the flame is stable within the combustion chamber. A premixed flame is called stable when the kinematics of the flame velocity are in balance with the velocity at which the incoming fresh mixture is supplied to the flame [47]. The flame is then anchored at the desired position in the combustion chamber. The flame can however be unstable and can blow off. It also can propagate upstream, which is called flashback. In Section 3.1 an overview of the different flashback mechanisms is provided. The focus of Section 3.2 will be on boundary layer flashback as it is regarded as the main flashback mechanism in gas turbines.

3.1. Flashback mechanisms

Flashback of premixed flames is a topic that is extensively investigated since the 1940s [39]. These investigations have revealed four different flashback mechanisms: core flow flashback, flashback due to combustion instabilities, boundary layer flashback, and flashback due to combustion-induced vortex breakdown [27, 31, 46]. Each different mechanism is briefly explained below:

- **Core flow flashback:** The flame is able to propagate upstream when the turbulent flame speed at some position in the combustion chamber is higher than the flow velocity [55]. This however, is not a common reason for flashback in an modern industrial gas turbine, because the core flow velocity in the premixer is in most cases well above the turbulent flame speed.

- **Flashback due to combustion instabilities:** Combustion instabilities can be generated by the interaction of acoustic modes, unsteady heat release, and flow structure [39], leading to velocity fluctuations. At high pulsation levels it periodically causes velocity deficits in the flow. The flame is able to propagate upstream when the frequency of the velocity deficits is low enough. However, as is stated by Lieuwen [46], such high pulsation levels should be avoided in a gas turbine for structural reasons, so that this type of flashback should not occur in stable combustor operation.

- **Flashback due to combustion induced vortex breakdown (CIVB):** This type of flashback occurs in swirl stabilized combustors. In these combustors, an internal recirculation zone is created on the burner axis, where the area suddenly increases between the prechamber and the combustion chamber, see figure 3.1. This internal recirculation zone stabilizes the flame during regular operation. However, under certain conditions between the internal recirculation zone and the flame, flashback can occur. The position of the flame front relative to the internal recirculation zone is thereby the critical parameter that leads to flashback [41]. The internal recirculation zone together with the flame propagate upstream on the burner axis into the premixer when flashback is initiated.

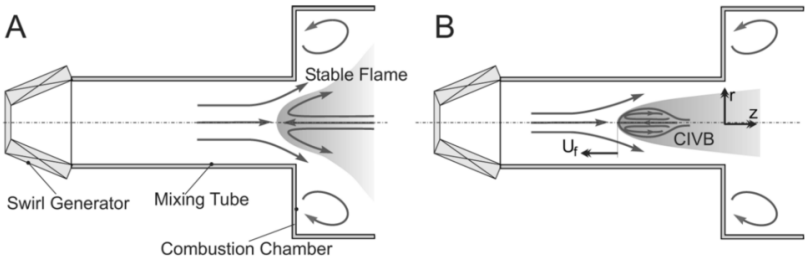

Figure 3.1: Visualization of the flashback process due to CIVB. (A) Denotes a stable flame, whereas (B) shows flashback due to upstream propagation of the recirculation zone together with the flame. Adopted from Kröner et al. [42].

- **Boundary layer flashback:** This type of flashback is regarded as one of the primary flashback mechanism in gas turbines. At the walls of the premix tube, the flow velocity reaches zero due to the no-slip condition. As a result, there are low velocity regions near the wall where the flame is likely to propagate upstream. Upstream flame propagation at the wall is only prevented by heat losses to the wall which will quench the combustion reactions. The distance from the wall where quenching occurs, depends on the fuel and on the flow conditions such as temperature and pressure. For a highly reactive fuel like hydrogen, the quenching distance is small and the flame is therefore highly prone to flashback. For hydrogen combustion in a gas turbine, boundary layer flashback is considered one of the most critical mechanisms and therefore the focus in this study is on this particular mechanism.

3.2. Boundary layer flashback

This section provides more details of the underlying mechanisms that lead to boundary layer flashback. First, the pioneering work on boundary layer flashback of Lewis and von Elbe [45] will be discussed in Section 3.2.1. In the Sections 3.2.2 and 3.2.3 the difference between confined and unconfined flame flashback is explained. Finally, in Section 3.2.4 the knowledge on boundary layer flashback obtained at the TU Delft is treated.

3.2.1. Critical velocity gradient model

The first systematic experimental research on boundary layer flashback was performed by Lewis and von Elbe in 1943 [45]. In this study, the flashback propensity of laminar premixed natural gas-air flames in tube burners of different diameters were investigated. Lewis and von Elbe introduced the widely adopted critical velocity gradient model, which is a simple model based on the velocity gradient at the wall to predict boundary layer flashback. Figure 3.2 shows a flame that is stabilized close to the wall. The flame speed reduces close to the wall due to heat loss and at a certain quenching distance δ_q the flame is quenched. To indicate whether the flame will flashback, the velocity gradient at the wall is used. According to this theory, the flame will propagate upstream when the local flame speed is higher than the local flow velocity close to the wall. The penetration distance δ_p is the location where the flame speed is equal to the flow velocity. Based on this, the critical velocity gradient, g_c is defined as:

$$g_c = \frac{u|_{y=\delta_p}}{\delta_p} = \frac{s_l}{\delta_p} \tag{3.1}$$

As long as the velocity gradient at the wall is higher than this critical velocity gradient, the flame will not propagate upstream.

3.2.1.1. Laminar and turbulent flames

A key assumption of the velocity gradient model is that the flow and the flame do not interact. Consequently, the velocity profile (and thus the velocity gradient) is not affected by the presence of the flame. Another assumption is that the flame speed is only affected by the wall, meaning that the flame speed reduces due to the heat loss to the wall. Under these assumptions the velocity gradient model is capable of correlating the experimental data of unconfined laminar flames [39]. This can be seen in Figure 3.3a, where the correlation of Berlad et al.[16] is used:

$$g_c = 14.125\left(\frac{s_l}{\delta_q}\right)^{1.168}, \tag{3.2}$$

Originally, the critical velocity gradient model is developed for predicting the flashback propensity of laminar flames. However, Kalantari et al. [39] mention that the model is extended to turbulent conditions where the flow velocity gradient is estimated using the Blasius correlation for a fully developed turbulent flow in smooth pipes with an internal diameter d_i:

$$g = 0.03955\mathrm{Re}^{0.75}\frac{U_b}{d_i}, \qquad 4\times10^3 < \mathrm{Re} < 10^5 \tag{3.3}$$

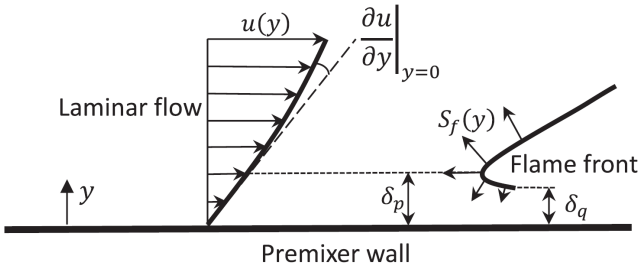

Figure 3.2: Illustration of the critical velocity gradient model. Adopted from Kalantari et al. [39].

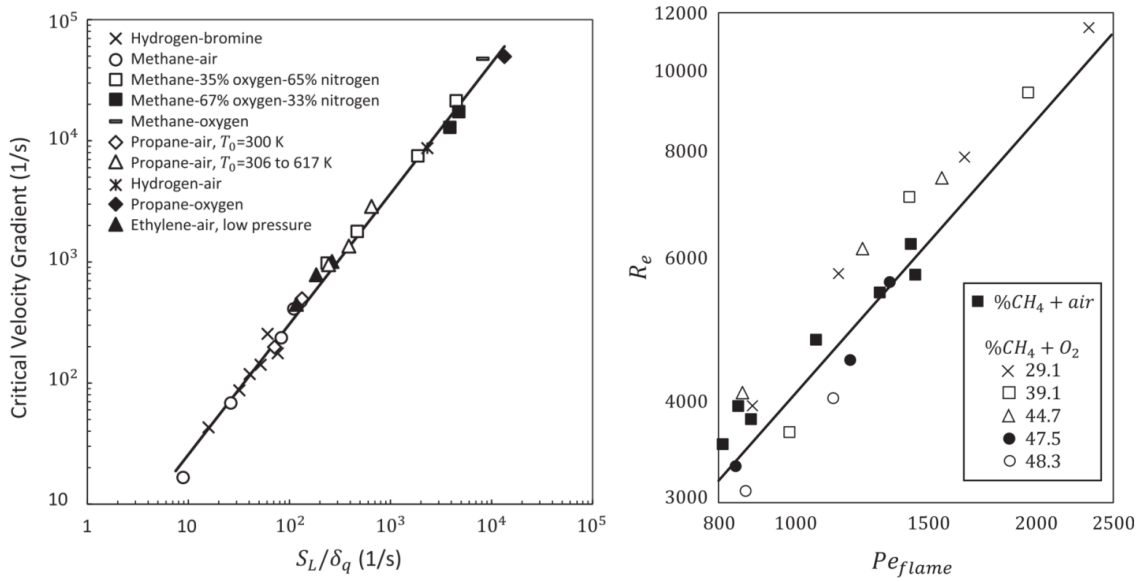

(a) (b)

Figure 3.3: **(a)** Flashback prediction for laminar flames using the correlation of Eq. (3.2), where the critical velocity gradient is a function of the laminar flame speed (s_l) and quenching distance (δ_q). **(b)** Flashback prediction for turbulent flames using the correlation of Eq. (3.4). The experimental results for turbulent flames deviate significantly from the predicted values. Adopted from Kalantari et al. [39].

where U_b is the bulk velocity. Eq. (3.1) and Eq. (3.3) together are used to determine the upstream flame propagation for turbulent flames. Khitrin et al. [40] used Eq. (3.1) and Eq. (3.3) and obtained the following correlation for flashback prediction:

$$\mathrm{Re} = 2.0 \cdot \mathrm{Pe}_f^{1.10}, \tag{3.4}$$

where Pe_f is the Peclet number defined as $\mathrm{Pe}_f = ds_l/\alpha$. The results of this prediction in comparison with the experimental data can be seen in Figure 3.3b. As can be seen, the critical velocity gradient model is not able to accurately predict the flashback limits for turbulent flames. This is due to the fact that (1) the unstretched laminar flame speed is used and (2) it is assumed that flashback occurs in the viscous sublayer ($y^+ < 5$) of the turbulent boundary layer. As discussed in Section 2.3 the flame stretch has a non-negligible impact on the flame speed. Also, as will be shown later in Sections 3.2.2 and 3.2.3 flashback does not occur in the viscous sublayer.

3.2.1.2. Confined and unconfined flames

In boundary layer flashback two flame configurations are distinguished. The first is called an unconfined configuration, where the flame is stabilized downstream of the burner rim. The second is called a confined configuration, where the flame exists inside a confinement, for example, a burner tube. A physical representation can be seen in Figure 3.4.

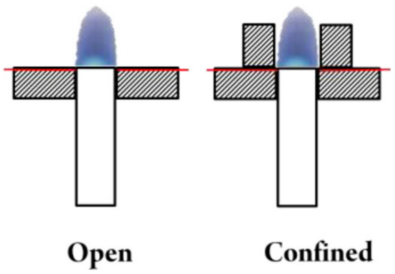

Figure 3.4: An open (unconfined) and a confined flame configuration. Adopted from Duan et al. [22].

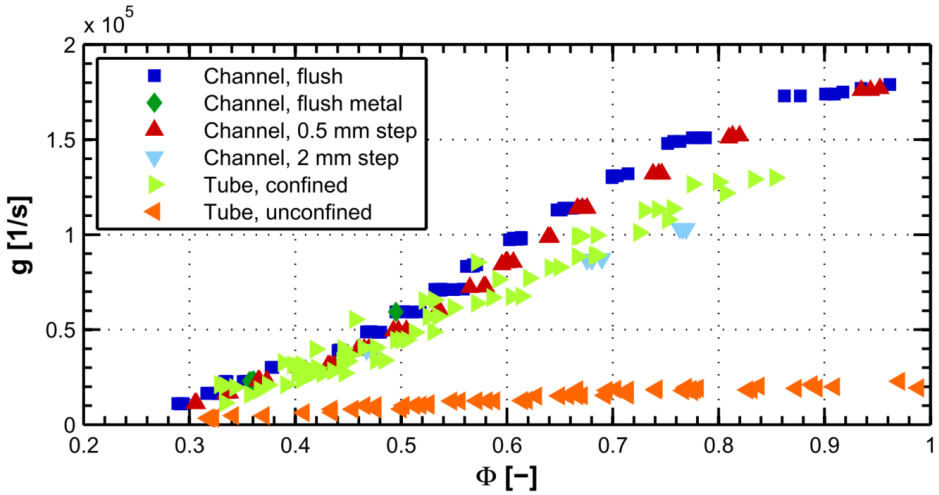

Figure 3.5: Boundary layer flashback limits of turbulent hydrogen flames for confined and unconfined configurations in terms of the velocity gradient g as a function of the equivalence ratio ϕ. Adopted from Eichler [27].

This distinction is made, because experimental research performed by Eichler et al. [26] showed a significant higher critical velocity gradient for confined flames than for unconfined flames as can be seen in Figure 3.5. It was shown in later studies that a laminar or turbulent flame propagating inside a confinement has an increased impact on the flow just upstream of the flame, which cannot be neglected [25, 35]. It is suggested that a confinement increases the backpressure induced by the flame on the upstream flow. The interaction of the flame with the flow shows that the critical velocity gradient model is not able to predict this type of flashback. It is therefore important to know the underlying mechanisms of the two different types of boundary layer flashback that lead to such significant differences in flashback propensity. This will be further elaborated on Sections 3.2.2 and 3.2.3.

3.2.2. Confined flame flashback

Confined flame flashback refers to the situation where the flame is already located inside the burner tube and propagates upstream along the wall. An experimental and numerical study on the flashback propensity of confined flames is performed by Eichler [27]. A channel burner that ends with a diffusing section with slopes of 0°, 2° and 4° was used. For the depicted 0° slope in Figure 3.6 three different configurations were studied. In the first configuration, a ceramic tile is mounted flush with the lower wall of the channel. In the second configuration, a stainless metal corner is placed over the ceramic tile and is again flush with the lower wall. The third configuration consists of a step size of 0.5 or 2 mm

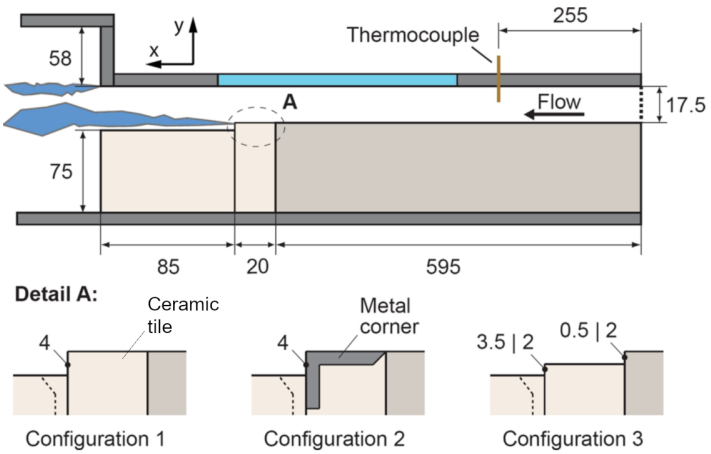

Figure 3.6: The setup used by Eichler to investigate a confined flame configuration. Adopted from Eichler et al. [26].

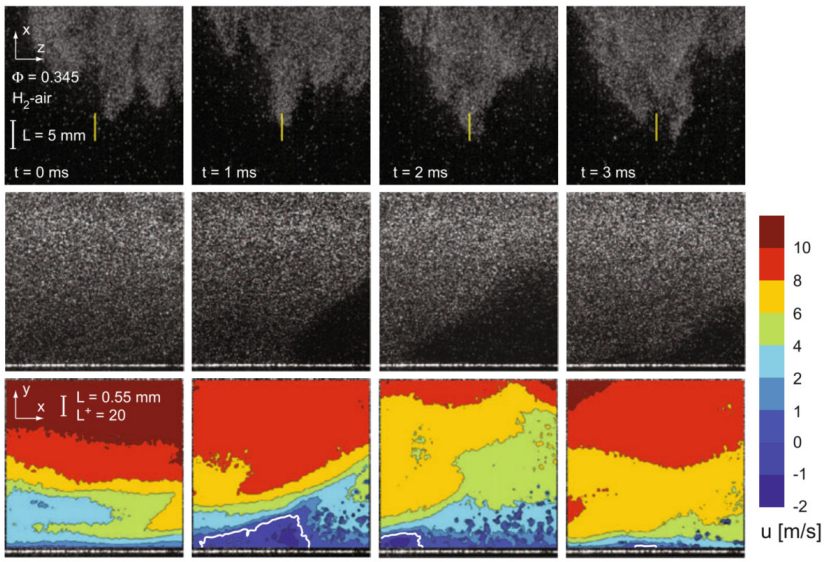

Figure 3.7: OH*-chemiluminescence, Mie-scattering and μ-PIV measurements of turbulent boundary layer flashback of hydrogen-air flames. x is the streamwise direction, y is the wall normal direction and z is the spanwise direction. Adopted from Eichler et al. [25].

with the lower wall. The flashback limits of these configurations in terms of the critical velocity gradient and equivalence ratio can be seen in Figure 3.5. This data is compared to the flashback limits of a tube burner with an unconfined and confined flame configuration [25]. It can be seen that the flashback propensity of a flame, that is confined inside the channel or a tube is much higher than the unconfined case. Furthermore, the flashback limits increase with a decrease in step height. In the step configuration the flame stabilization is the same as for the unconfined case, where quenching of the flame forms a small gap between the wall and the flame. Eichler [27] contributes the lower flashback propensity of the step configurations to a so-called leakage flow that 'leaks' through the small gap between the flame and the burner rim. This leakage flow convects heat from the preheat zone of the flame and thus prevents the flame from propagating in the upstream direction. It is suggested by Baumgartner [11] that this leakage flow plays also a role in unconfined flashback discussed in Section 3.2.3.

As the difference in flashback propensity between confined and unconfined was significant, Eichler [25] investigated the upstream flame propagation in the near wall region for both laminar and turbulent flames with μ-PIV, OH*-chemiluminescence and Mie-scattering measurements. From a macroscopic view, the laminar flames in the channel propagated with a homogeneous and unwrinkled flame front, whereas the turbulent flame front was highly irregular, wrinkled, and formed cusps in the leading parts of the flame. These cusps separated into new cusps and a high fraction of these cusps moved in the upstream direction, leading to a global upstream motion of the turbulent flames, as is visualized by the upper four OH*-chemiluminescence images in Figure 3.7.

The close-up of the upstream propagation of a turbulent hydrogen flame is shown in the bottom two image rows in Figure 3.7. A backflow region, marked by a white isoline of zero axial velocity, is observed just upstream of the flame tip. A similar observation was done earlier by Heeger et al. [36] in a swirl burner with a bluff body. Eichler [27] observed the same phenomenon for laminar flames, different fuels, and different channel slopes. It was assumed that the boundary layer separation is caused by an increased adverse pressure gradient in front of the flame. Eichler [27] performed a numerical study on flashback of a premixed laminar hydrogen-air flame to further verify the separation of the boundary layer. This has led to the development of a new physical model for laminar and turbulent wall flashback, which is depicted in Figure 3.8. The numerical simulation showed that the presence of the flame caused a strong upward deflection of the streamlines. According to inviscid flow theory, curved streamlines go together with a positive pressure gradient that is pointing outwards from the center of curvature [34]. Eichler [27] states this as the main reason for the high static pressure rise upstream of the flame. In

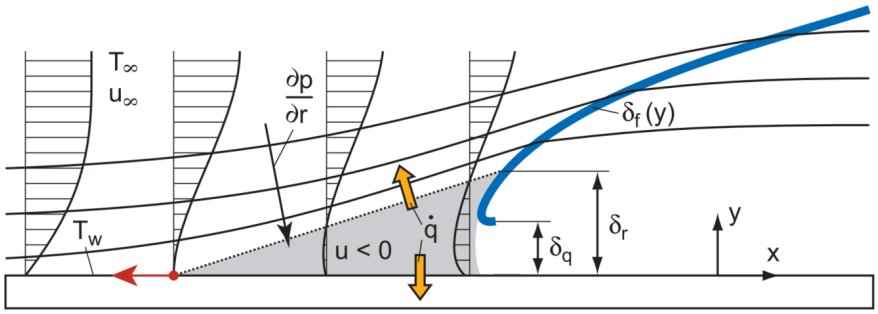

Figure 3.8: Physical model for laminar and turbulent wall flashback developed by Eichler [27].

addition, the existence of a wall below the flame reduces the flow volume of the burned gases, which lead to higher flow velocities and thus to an increased backpressure of the flame. The two-dimensional flame-flow interaction shows therefore a higher pressure rise than the one-dimensional backpressure analysis of Eq.(2.19).
An interesting fact is that the upper wall also affects the backpressure of the flame. The streamlines must eventually be parallel to this wall, which leads to less curvature of the streamlines and thus the adverse pressure gradient is reduced.
Gruber et al. [35], who performed a Direct Numerical Simulation (DNS) of boundary layer flashback in a turbulent channel flow, suggested that the formation of backflow regions is due to the interaction of the fluctuating turbulent flow with the hydrodynamic instability. The idea is that a flame cusp is initiated by turbulence and the hydrodynamic instability causes a sufficient adverse pressure gradient to cause a backflow in front of the flame. However, according to Eichler [27] this backflow does not necessarily lead to upstream flame propagation. It has to reach a certain height δ_r, which is larger than the quenching distance δ_q, to be able to sustain the chemical reaction of the flame and cause the flame to propagate upstream. The reported heights of the backflow region of turbulent hydrogen-air flames are between 0.53 - 0.96 mm [27]. The flame is then anchored inside the top region of this backflow which correspond to $y^+ \approx 25$ to 35. Looking at the turbulent mean velocity profile (see Section 2.1.3) this corresponds to the buffer layer where the velocity profile is not linear anymore.

3.2.3. Unconfined flame flashback

Unconfined flame flashback refers to the situation where an initially stable flame at the burner rim eventually moves into the burner tube. Baumgartner [11] performed an experimental study on the flashback process of an unconfined flame. The used measurement techniques were PIV, PLIF, OH*-chemiluminescence, and Mie-scattering. First the difference between the velocity field of isothermal flow and stable combustion has been examined. In contrast to the observation of Eichler et al. [25] for confined flames, no clear interaction between the stable, unconfined flame and the approaching flow was observed. The reason for this observation was given to be the outward deflection of the flame downstream of the channel wall. At flashback conditions, the velocity field of the flow was clearly deflected and retarded due to the front of the flame tip, which increased the upstream propagation velocity of the flame as is visualised by the PIV-measurements in Figure 3.9a. This interaction of the flame with the flow is linked to the backpressure of the flame. However, in this experiment no backflow region was observed, in contrast to what Eichler et al. [25] observed for confined flames. Baumgartner [11] states that this is due to the setup of the channel burner, where the upper wall was 7 mm shorter than the lower wall. This has as a consequence that the flame is not entirely confined during the initial phase of flashback. It was also observed that during flashback, the flame did not jump onto the lower wall, but as can be seen in Figure 3.9b, it bends convex to the reactants at some distance $s_f \approx 3$ mm downstream of the burner rim, which is larger than the quenching distance δ_q. The formed flame tip propagated upstream at a vertical distance of approximately $d_f \approx 1$ mm, see Figure 3.9b. This is slightly higher than the measured values for a confined flame ($d_f \approx 0.53$ - 0.96 mm) [25]. The

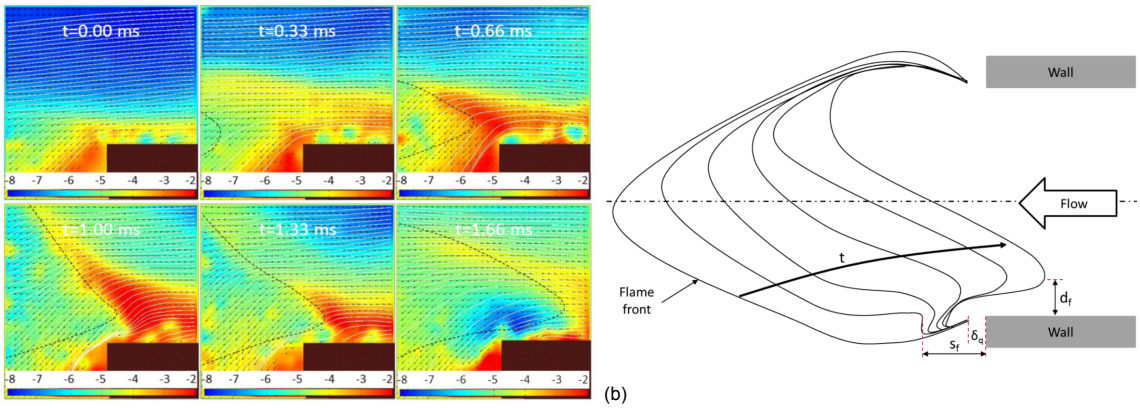

Figure 3.9: **(a)** PIV measurements of the flame propagation of an unconfined flame. Note that the flow velocity is defined negative from left to right. **(b)** Illustration of the flame front transition from a unconfined stable flame to flashback. Adopted from Baumgartner [11].

experimental results of Baumgartner [11] showed that the streamline through the flashback starting position s_f downstream of the burner rim corresponds to the location y_f within the channel, see Figure 3.10. At s_f the flame speed is equal to the flow velocity at the onset of flashback. Baumgartner [11] therefore proposes the following prediction model for unconfined flames, see also Figure 3.10:

$$s_l(s_f) = u(s_f) \propto u(y_f) \tag{3.5}$$

This states that the flashback propensity of an unconfined flame is a function of the undisturbed velocity profile of the approaching fresh mixture, which should explain why the critical velocity gradient model has been capable to predict flashback for unconfined laminar and some turbulent flames. However, it is observed that the distance y_f ranged between 0.6 and 0.7 mm, which corresponds to $y^+ = 13 - 21$. This observation is not consistent with the critical velocity gradient model, where a linear velocity profile is assumed at flashback, which is only valid in the viscous sublayer $(y^+ < 5)$. Hoferichter [37] further investigated and modified the unconfined flashback prediction model by Baumgartner. The onset of flashback was linked with the streamline where the turbulent velocity fluctuations in a fully developed channel or pipe flow are maximum. The location of this streamline corresponds to $y^+ = 16.4$ and it is assumed that at the onset of flashback, the turbulent flame speed and the turbulent flow velocity are equal along this streamline.

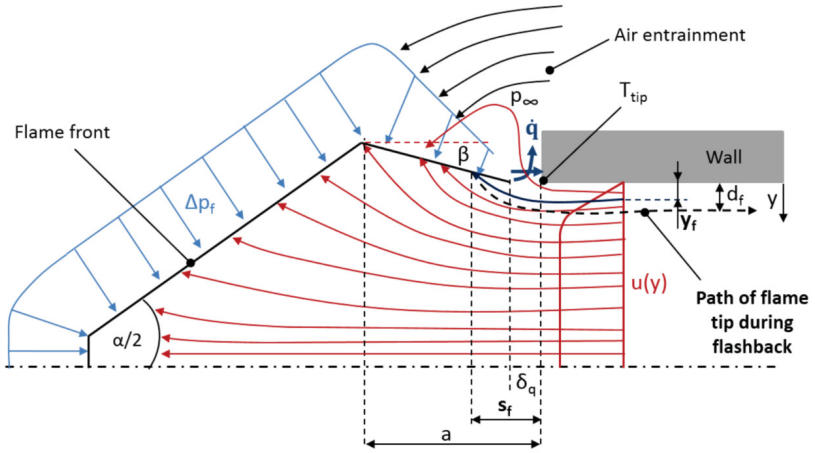

Figure 3.10: Illustration of a stable, unconfined flame close to the flashback limit. The streamlines are shown in red and the black dashed line denotes the propagation path of the leading flame tip during flashback. Adopted from Baumgartner [11].

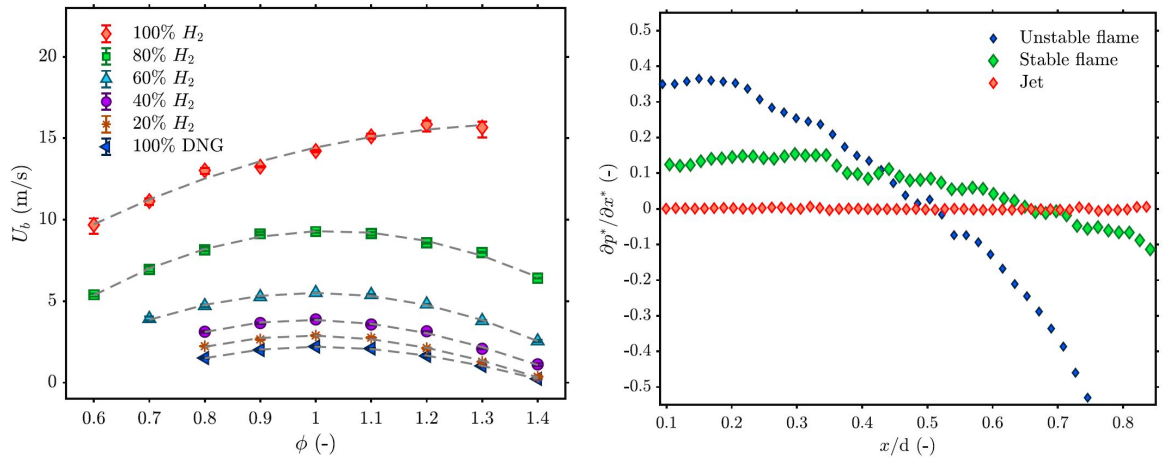

(a) (b)

Figure 3.11: **(a)** Bulk velocity as function of equivalence ratio at flashback conditions, for different fuel composition mixtures ranging from pure hydrogen (100% H_2) to pure natural gas (100% DNG). **(b)** Pressure gradient for a jet, a stable flame and an unstable flame. The average adverse pressure gradient increases with a flame closer to flashback. Both figures are adopted from Faldella [28].

An unconfined flame is thought of to be less prone to flashback compared to a confined flame due to two reasons [12, 27]: first, the quenching gap between the flame and the wall gives rise to a so-called leakage flow of the fresh mixture, which convects heat from the preheat zone of the flame and thus prevents the flame from propagating in the upstream direction. It is also suggested that this leakage flow accelerates through the quenching gap and thus reduces the effect of flow separation close to the burner rim [67]. Secondly, the expansion of the exhaust gases is not obstructed by a wall, which reduces the backpressure effect of the flame. However, the effect of the obstruction of the exhaust gases is not shown experimentally. Moreover, it remains unclear why the flashback starting position of an unconfined flame shown in Figure 3.9b is at a relatively large downstream distance.

3.2.4. Previous numerical and experimental studies performed at the TU Delft

Recently, experimental studies on boundary layer flashback have been performed at the TU Delft. Faldella [28] investigated the flashback propensity of natural gas/H2-air flames in terms of a critical velocity gradient (g_c) and bulk flow velocity (U_b) as a function of equivalence ratio for different hydrogen concentrations. Flashback occurs when the bulk velocity of a certain mixture composition at a certain equivalence ratio is lower than the critical bulk velocity. The critical bulk velocities are put in a flashback map as can be seen in Figure 5.2a.

Most interestingly for this present study, the onset of flashback has been visualized for premixed natural gas and hydrogen flames, which is done by Mie-scattering and PIV measurements. The Mie-scattering and PIV images of a premixed natural gas-air flame at the onset of flashback can be seen in Figure 3.12a and 3.12b respectively. In the second image of Figure 3.12a a convex bulge of the flame into the reactants appears at some distance downstream of the burner rim. This flame bulge is advected downstream by the flow. Simultaneously, the bulge grows very fast and flattens in time. A qualitatively similar process is observed for the hydrogen-air flame as can be seen in Figure 3.12c and 3.12d, but the flame front of the hydrogen-air flame is much more wrinkled during this process and the time for the hydrogen-air flame to propagate upstream is approximately one fifth of the time needed for the natural gas-air flame. Faldella [28] states that the adverse pressure gradient in front of the flame is the key factor that leads to flashback. It was shown by solving the Navier-Stokes equations in the unburned mixture that the average adverse pressure gradient increases for a flame closer to flashback, see Figure 3.11b. The effect of the adverse pressure gradient can most clearly be seen in the third last PIV-image of Figure 3.12d. The convex flame bulge into the reactants leads to a deflection and retardation of the incoming flow, which is referred to as the hydrodynamic instability described in Section 2.4.1.

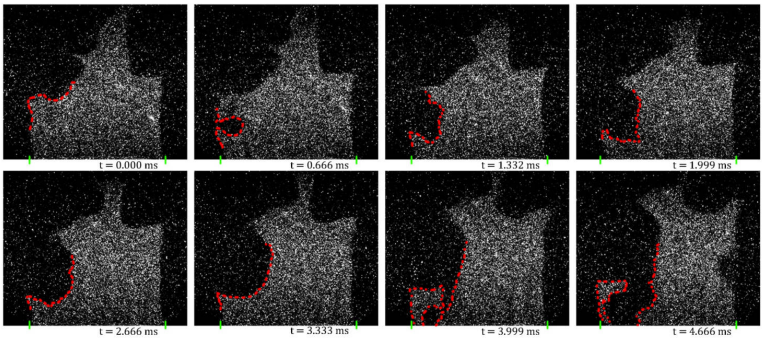

(a) Mie-scattering measurements for a natural gas-air flame.

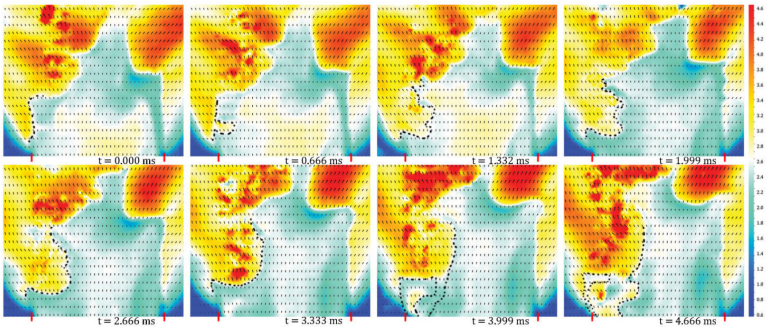

(b) PIV measurements for a natural gas-air flame.

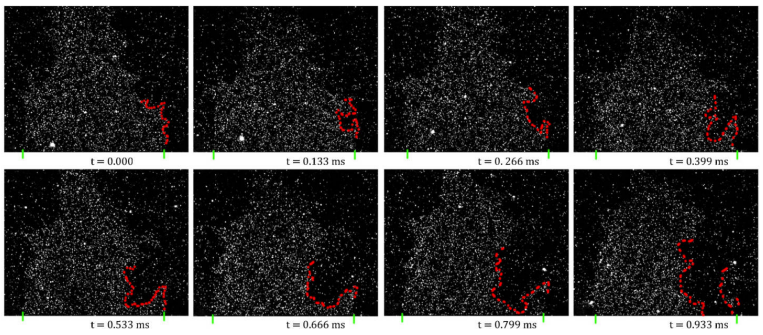

(c) Mie-scattering measurements for a hydrogen-air flame. The flame is much more wrinkled than the natural gas-air flame

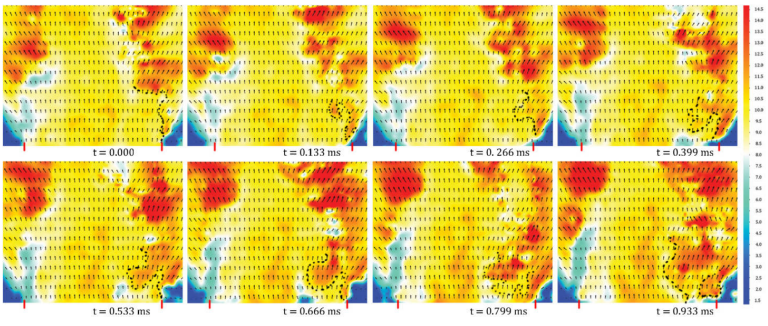

(d) PIV measurements for a hydrogen-air flame.

Figure 3.12: Mie-scattering and PIV measurements of the flashback process for turbulent natural gas-air and hydrogen-air flames. From the PIV measurements it can be seen that the flow decelerates in front of a convex flame bulge. Adopted from Faldella [28].

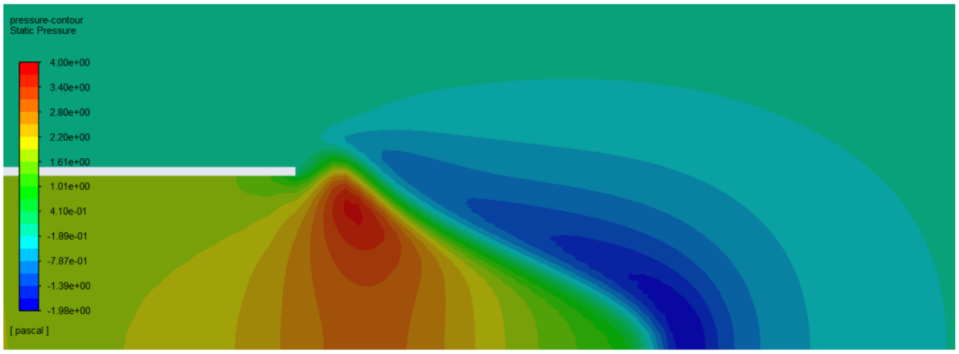

Figure 3.13: The static pressure contours of a flame close to flashback. The flame is located in the green zone, between the red and the blue contours. Note the high pressure gradient in front of the flame. Adopted from van Put [66].

This phenomenon is observed for both stable and unstable flames, but the interaction becomes stronger for unstable flames at the onset of flashback. These flames are closer to the burner exit, so it is suggested that the diverging flow is obstructed by the tube walls leading to a stronger retardation of the flow. When this retardation is strong enough, it will cause flame flashback. It is noted that the observed upstream flame propagation for both flames does not start in the direct vicinity of the wall, which was also observed by Baumgartner [11]. However, since the visualization of flashback process was limited to the region downstream of the burner exit, it is unclear how the flame propagated further into the burner tube.

More recently, Van Put [66] performed a CFD simulation of the flashback process in tube burners with unconfined flames. The study showed that when the bulk velocity was decreased and consequently the flame was closer to flashback, the adverse pressure gradient in front of the flame increased (Figure 2.5), which is similar to what Faldella [28] reported. The static pressure contours of a flame close to flashback can be seen in Figure 3.13. Similar to what Baumgartner [11] observed, no boundary layer separation occurred when flashback was initiated. This indicates that boundary layer instability does not play a role in the flashback process of an unconfined flame. Another interesting result was that the flow velocity did not fall below the turbulent flame speed near the flashback conditions, which is different to what Baumgartner [11] suggested. It seems that the flashback process is initiated after a certain threshold is exceeded and is self-amplifying thereafter [66].
Recently, Lambers [43] has reported on the effects of velocity fluctuations on flashback by means of a small obstacle mounted in the tube inner wall that could vary in height. The experimental obtained bulk

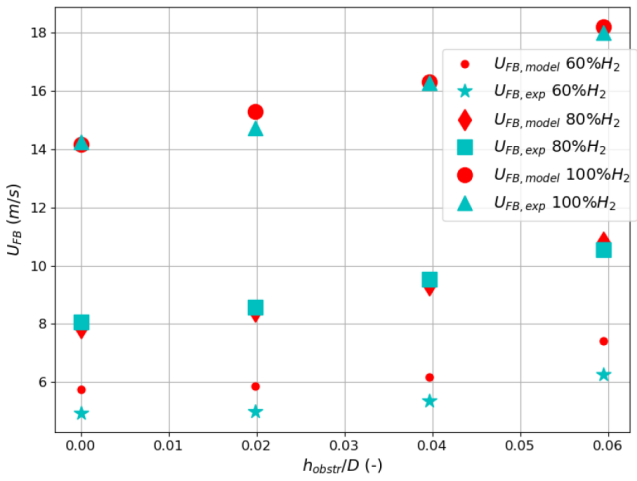

Figure 3.14: Comparison between experimental and modeled bulk velocities at flashback with the dependence on a dimensionless obstruction height. Adopted from Lambers [43].

velocities at flashback were compared to the predicted values of a modified version of the unconfined flashback model by Hoferichter [37] for stoichiometric 60 - 100 % hydrogen-air flames. Both showed the same dependence on the obstacle height as can be seen in Figure 3.14 and thus indicated that the turbulent flame speed is a critical parameter in the flashback process of a unconfined premixed flame [43]. The flashback process was visualized by means of Mie-scattering and PIV. When the obstacle was flush with the tube inner wall, flashback was initiated around 8 - 12 mm downstream of the burner exit and a similar flashback process was observed as visualized in Figures 3.12a and 3.12c. The observed downstream distance of flashback initiation differs about three to four times the downstream distance that Baumgartner [11] observed. When the height of the obstacle was increased, the bulk velocity at flashback (U_b), the turbulent velocity fluctuations (u') and the flame angle (α_u) increased. The screw which served as the obstacle caused the flame to anchor closer to the burner rim, which confirmed the increased flashback propensity. A different flashback process was observed when the boundary layer was obstructed. First, the flame anchors very close to the burner rim, then it moves upstream to the obstacle and anchors there. Finally, flashback is initiated at the obstacle. However, the last two steps are assumptions, because the flow upstream of the burner rim could not be visualized.

4

Experimental setup and methodology

4.1. Bunsen Burner setup

4.1.1. Hardware

The experiments were done with a Bunsen burner setup as can be seen in Figure 4.1. The setup is similar to the setup used in previous works by Faldella [28] and Lambers [43], except for the end section of the burner tube. To visualize both the unconfined and the confined flashback process it is necessary to obtain optical access to the inside of the burner tube. Therefore, the burner was equipped with a quartz tube, which seamlessly fitted with the copper part of the burner tube.

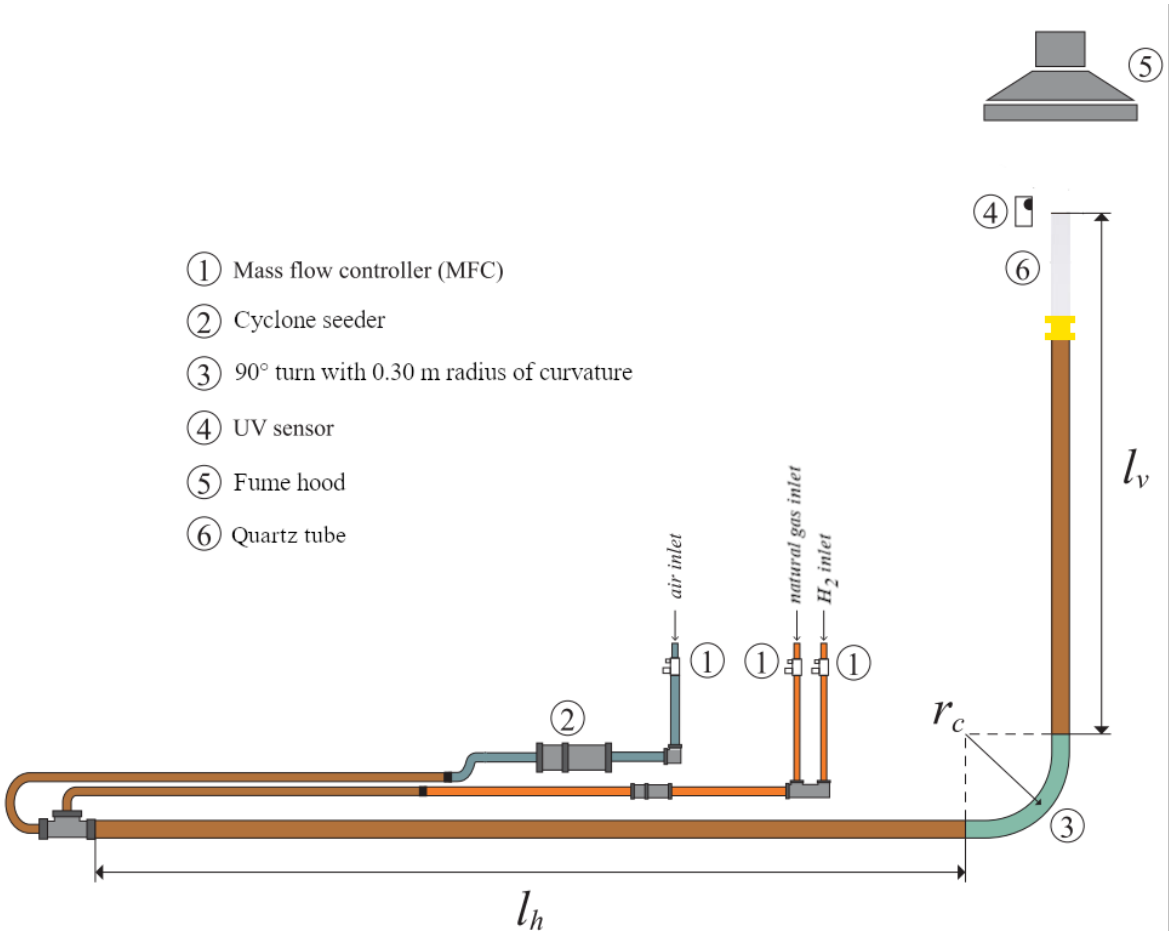

Figure 4.1: Sketch of the experimental setup used in this investigation.

Bunsen burner	Horizontal tube	Turn	Vertical tube	Final tube
Inner diameter d_i [mm]	25.0		25.67	25.16
Wall thickness t [mm]	2.0		1.1	1.47
Length l [mm]	2300		1000	219
Length-over-diameter ratio l/d_i [mm]	92		39	8.7
Material	copper	PVC	copper	quartz

Table 4.1: Details of the dimensions of the Bunsen burner setup used in the experiments.

A large length-over-diameter ratio (l/d_i) is required to obtain a fully developed turbulent flow in the burner tube. According to Çengel et al. [19] this ratio can be calculated from:

$$\frac{l}{d_i} = 1.359\mathrm{Re}^{\frac{1}{4}}. \tag{4.1}$$

In the experiments, Reynolds numbers up to 27850 were used, which leads to a length-over-diameter ratio of approximately 18. To achieve this large ratio within the lab, a long horizontal tube is connected with a 90° bend to the vertical burner tube. Details on the dimensions of the Bunsen burner setup are given in Table 4.1.
Two self adhesive polymide thermocouples of type K were used to monitor the temperature of the burner tip. One thermocouple was placed 1 mm below the burner tip, whereas the other one was placed 25 mm below the burner tip. Both thermocouples have a reaction time of 0.08 s and have an operating range between -40°C and +250°C.
The three gas supply lines are each equipped with a mass flow controller, which are used to regulate the combustible mixture of air, natural gas and hydrogen in the burner. The mass flow controllers are manufactured by Bronkhorst and have an uncertainty of 0.1% of the full scale (FS) plus 0.5% of the flow rate reading (RD) [1]. The mass flow controllers measure the flow in normal liters per minute, which has to be converted into liters per minute, using the ideal gas law:

$$Q_{actual} = Q_{reading}\left(\frac{p_n}{p}\right)\left(\frac{T}{T_n}\right) \tag{4.2}$$

where Q_{actual} is the measured flow in liters per minute, $Q_{reading}$ is the measured flow in normal liters per minute, p is the lab pressure and T is lab temperature. The subscript n denotes the normal reference values of the pressure and temperature, where $p_n = 10132.5$ Pa and $T_n = 273.15$ K. The lab conditions were continuously measured by a portable weather station and were communicated to the mass flow controllers.
The UV-sensor in Figure 4.1 is used as a safety measure. It is only possible to open the main fuel lines when the UV-sensor detects a pilot flame. When the pilot flame has ignited the main flame, the UV-sensor detects the main flame and keeps the fuel lines open. If the flame blows off or flashes back, the UV-sensor detects no combustion and the fuel lines are then automatically cut off.

4.1.2. Control panel

The three mass flow controllers regulate the fuel and air mixtures. The communication with the mass flow controllers is via a computer with a LabView control panel. In this control panel all relevant parameters are filled in to obtain the desired mass flows of fuel and air, such as: the lab temperature and pressure, the burner tube inner diameter d_i, the equivalence ratio ϕ, the volume percentage of hydrogen in the fuel and the Reynolds number. The Reynolds number is used as the parameter to control the bulk velocity of the unburned mixture. This gives more information about the characteristics of the flow. In order to convert the Reynolds number into a bulk velocity, the dynamic viscosity of the combustible mixture has to be calculated. A wide range of mixtures consisting of hydrogen, natural gas, and air were used in the experiments. Therefore, Wilke's method [71] is used to calculate the dynamic viscosity. For an overview of the control panel and the used equations, the reader is referred to Appendix A.

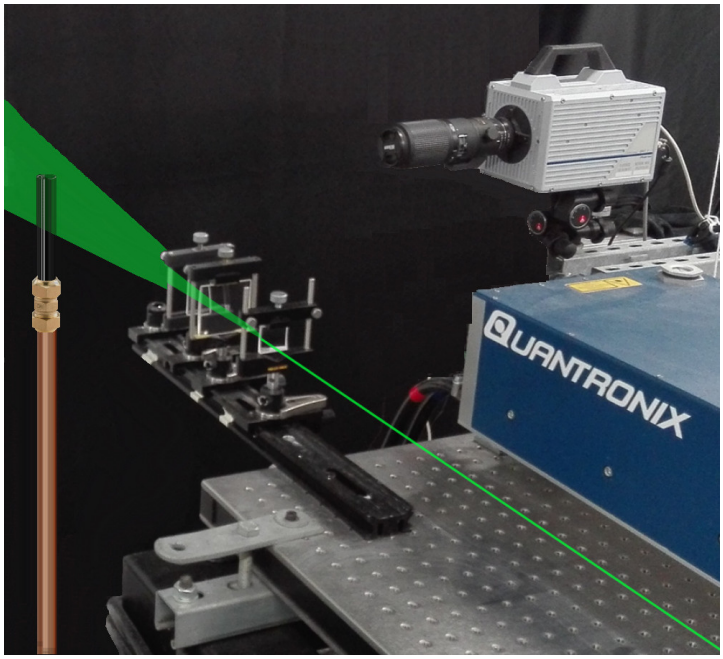

Figure 4.2: The Particle Image Velocimetry (PIV) setup with the laser, the light sheet optics and the high speed camera. The high speed camera views the seeding particles through the quartz tube in radial direction, perpendicular to the laser sheet.

4.2. Flow measurement technique

4.2.1. Planar Particle Image Velocimetry

Particle Image Velocimetry (PIV) was used to acquire the 2D velocity field in a planar cross section of the flow in a non-intrusive manner. The PIV setup consists of a laser, light sheet optics, seeding particles, a high-speed camera, and software to control the equipment and convert the camera images into velocity fields using correlation algorithms. The PIV system in the lab, as can be seen in Figure 4.2, uses a Photron Fastcam SA1.1 camera and a Quantronix Nd:YLF dual-cavity laser type Darwin-Duo Pro 527-80-M. The laser beam emits green light with a wavelength of 527 nm. The laser beam first passes through a horizontal plano-concave lens to widen the laser beam to a laser sheet in the vertical direction. Then, it passes through a vertical plano-convex lens to obtain a laser sheet of approximately 1 mm thickness. This laser sheet finally passes through the quartz tube section of the burner, but it also illuminates the air above the burner rim.

The air and fuel mixture were seeded with flow tracer particles with a diameter of 1 μm. This is done via a cyclone seeder, see Figure 4.1. The seeding particles that were used are on the same order of magnitude of the wavelength of light that is emitted by the laser. This leads to a phenomenon called Mie-scattering. Mie-scattering is an elastic light scattering that causes a significantly increased scattered light intensity in comparison with flow velocity measurements based on Rayleigh scattering with no seeding particles [30]. Therefore, the motions in the flow can clearly be tracked by the high-speed camera.

In flows with combustion, the Mie-scattering phenomenon can be used to visualize the flame front. To be able to do so, the seeding particles have to survive the high temperatures of the flame. Therefore, aluminium-oxide (Al_2O_3) was used as the seeding particle material. An example of a flame front determined by Mie-scattering can be seen in Figure 4.3. The flow enters the image at the bottom and leaves at the top. When the seeding particles move through the flame front, they undergo a large acceleration due to the heat release by the combustion reaction. Equivalent to the decrease in gas density after the flame front, the seeding particle density decreases after the flame front. The difference in seeding particle density before and after the flame front leads to a higher and lower light scattering intensity, respectively. According to this knowledge, it can be determined that the flame front exists between the difference in seeding particle density.

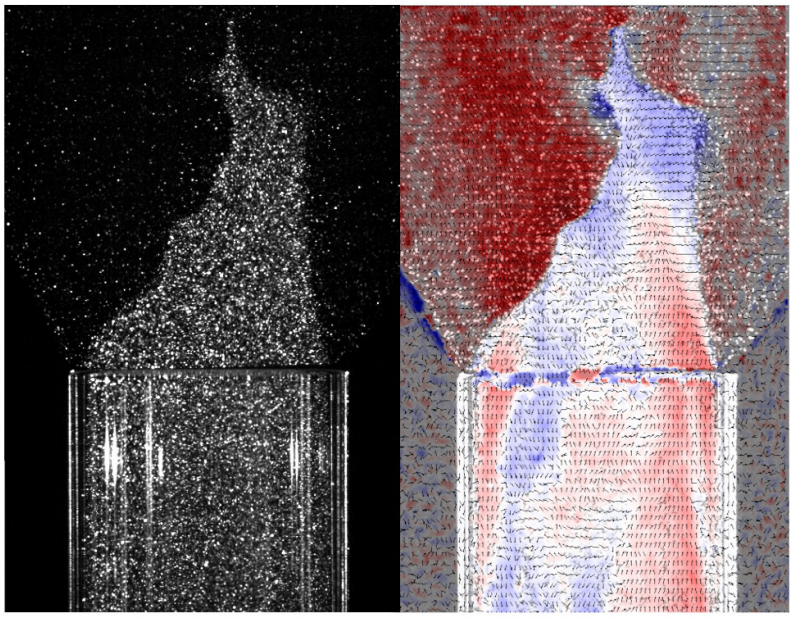

Figure 4.3: On the left-hand side a Mie-scattering image of a turbulent pure natural gas flame with on the right-hand side the corresponding instantaneous velocity fluctuations obtained from DaVis 8.4.0.

The seeding particles were chosen such that the velocity fluctuations of the flow could be followed accurately. The extent to which a particle can follow the flow, can be obtained from the Basset-Boussinesq-Oseen (BBO) equation, which describes the motion of a rigid spherical particle in a viscous fluid [50]. The properties of the seeding particles can be used to simplify this equation. First of all, the seeding particles have a density much larger than the surrounding air ($\rho_p >> \rho_{\text{air}}$). Secondly, the diameter of the particles is smaller than the Kolmogorov length scale ($d_p < l_\eta$), where $l_\eta \approx 10$ μm for the highest Reynolds number used in the experiments. These properties lead to the simplified BBO equation [62]:

$$\frac{\pi}{6}\rho_p d_p^3 \frac{du_p}{dt} = 3\pi\mu d_p(u - u_p), \tag{4.3}$$

where ρ_p is the particle density, d_p is the particle diameter and u_p is particle velocity, μ and u are the dynamic viscosity and the velocity of the surrounding air, respectively. The term on the right hand side of Eqn.(4.3) is the viscous drag according to Stokes' Law, which is accurate when the relative particle Reynolds number is small, i.e. $\text{Re}_{pr} = Vd_p/\nu < 1$, where $V = u - u_p$ is the relative velocity between the particle and the air flow. If we now assume a uniform flow with a velocity u and a particle is released from rest at $t = 0$, then the solution of Eqn.(4.3) reads:

$$u_p(t) = u\left(1 - e^{\frac{-18\mu}{\rho_p d_p^2}t}\right) = u\left(1 - e^{\frac{-t}{\tau_p}}\right), \tag{4.4}$$

where τ_p is the so-called particle response time, given by:

$$\tau_p = \frac{\rho_p d_p^2}{18\mu}. \tag{4.5}$$

The particle response time is a characteristic timescale that represents the time that is needed to accelerate a particle at rest to approximately 63% of the surrounding air velocity. The seeding particles that were used in the experiments consist of aluminium-oxide (Al_2O_3), which has a density of 3200 kg/m^3. The particles have a mean diameter of 1 μm. At a temperature of 300 K, the dynamic viscosity of air is $18.7 \cdot 10^{-6}$ Pa·s. This results in a particle response time of 9.5 μs. A way to determine if the particles will behave as tracers is to compare the particle response time with the Kolmogorov time scale

of the flow, which is represented by the Stokes number St:

$$St = \frac{\tau_p}{\tau_\eta}. \tag{4.6}$$

If $St << 1$, the seeding particles accurately follow the flow and behave as material tracers. If $St >> 1$, the particles are completely unresponsive to the flow [50]. The Kolmogorov time scale τ_η can be determined from Eqn.(2.7), where η is scaled with the bulk flow velocity U_b and the tube diameter d. For the flow with the highest Reynolds number (Re = 23000), this results in $St \approx 0.85$. This means that at the smallest scales of the flow, the seeding particles did not accurately represent the fluid motion. However, for larger scales in the flow, the used seeding particles were excellent tracers.

4.2.2. Quartz tube

As it is the goal of this study to investigate the flashback process of an initial unconfined flame into a (confined) tube, both the area inside and outside the burner have to be captured in a single frame. The optical access inside the burner tube is provided by a quartz tube that is mounted on a copper tube. Besides the optical access, the quartz tube can give some optical distortions. The high-speed camera views the seeding particles through the quartz tube in radial direction, perpendicular to the laser sheet. The light scattered from the seeding particles in the laser sheet has to pass through the curved quartz tube before it reaches the camera lens. In this way, the quartz tube acts as a weak lens, which deforms the obtained image by the high-speed camera. This effect is the strongest near the tube wall.

It is necessary for the PIV experiments to know whether the quartz tube cause large deformations in the obtained images. If so, the motions of the seeding particles do not represent the true motion of the flow and will result in erroneous velocity fields. To compensate for the optical distortion of the quartz tube, a calibration target has been placed both inside and outside the tube as can be seen in Figure 4.4a. Every mark position on the calibration target has a length of 1 mm in both the axial and the radial direction and the spacing between the center of the crosses is 2 mm. The calibration software of DaVis 8.4.0 uses the calibration target to obtain a pixel-wise mapping that is subsequently used to correct the acquired PIV images for the optical distortion caused by the quartz tube. Figure 4.4b shows the result of the calibration. To know whether the calibration can be used for the PIV measurements

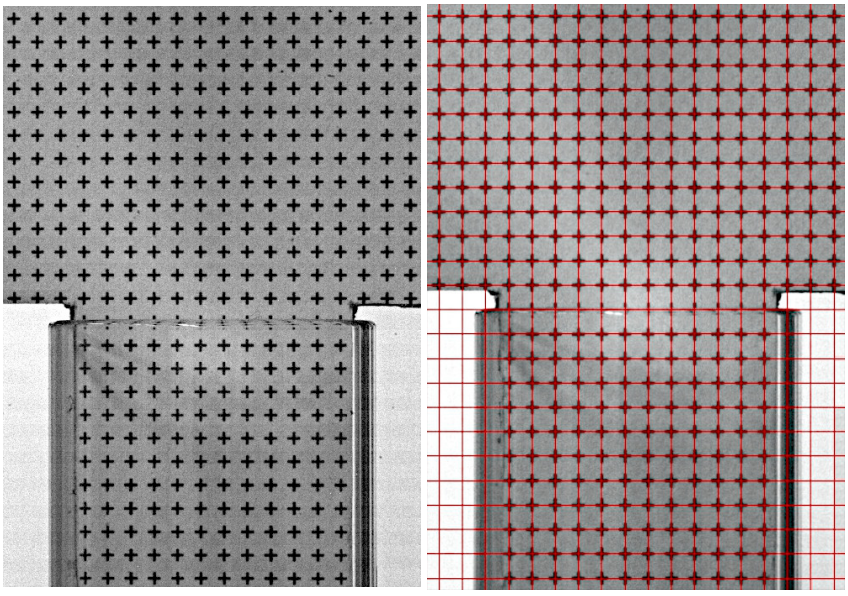

(a) (b)

Figure 4.4: **(a)** Raw image of the quartz tube with a calibration target. **(b)** Calibrated image after correction for the optical distortions caused by the quartz tube.

a so-called RMS fit value is presented by DaVis. This RMS fit value shows the average deviation of the dewarped mark positions to the ideal regular grid and is denoted in pixels. For a good calibration, DaVis recommends a RMS of fit lower than 1 pixel. The RMS fit value of the calibration is 0.25 pixel, so the calibration is excellent for the PIV measurements.

4.2.3. Image processing

The raw images were obtained and processed using the software of DaVis 8.4.0. The processing was done in three steps. In the first step, the images were preprocessed to enhance the quality of the raw data. A particle intensity normalisation (min/max filter) was applied with a scale of 3 to 4 pixels depending on the image quality. In the second step, the image processing was done via cross-correlation using multipass iterations with decreasing interrogation window size. First, two passes with a window size of 32 x 32 pixels with an overlap of 50% and then three passes with a window size of 12 x 12 pixels with an overlap of 75%. Adaptive PIV was used as the weighing function for the interrogation windows. This function will change the interrogation window size and shape automatically and optimized locally according to the local seeding density and flow gradient. This leads to the highest possible accuracy, robustness, and spatial resolution [2]. The only drawback is the required computation time. In the third processing step, the obtained vector were postprocessed using the universal outlier detection filter [70]. The empty spaces due to the filter were filled up using linear interpolation.

4.3. Experimental methodology

To gain insight in the physical mechanisms that play a role in the transition from unconfined to confined flame flashback and the difference in flashback behaviour between natural gas flames and hydrogen flames, four main experiments were done. In the first experiment, the velocity profile and turbulence statistics of the non-reacting flow (cold flow) were measured by means of PIV in order to verify that the turbulent flow was fully developed. In the second experiment, the flashback limits of the quartz Bunsen burner were investigated for different natural gas/hydrogen fuel compositions at different equivalence ratios. In experiment 3, PIV was used to measure the mean velocity profiles in the presence of the flame. These mean velocity profiles were then compared to the velocity profiles of the cold flow obtained in experiment 1. In addition, the mean velocity profile of a flame brought close to flashback conditions was compared with the mean velocity profile of a stable flame. The influence of the flame on the Reynolds stresses is also considered here. In the fourth experiment, the transient flashback process was visualised for a pure natural gas and a pure hydrogen flame by means of PIV and Mie-scattering measurements. All four experiments were done with a macro-PIV setup using a Tokina F 100mm f/2.8 Macro AT-X Pro lens. The resulting field of view was 40 mm x 80 mm. However, in experiment 4 also a micro-PIV setup was used to capture the interaction of the pure hydrogen flame with the flow. In this micro-PIV setup, a Nikon AF Micro-Nikkor 200mm f/4D IF-ED lens is fitted on the camera with a field of view size of 12 mm x 24 mm.

4.3.1. Experiment 1: Cold flow

In this experiment the mean velocity profile and turbulence statistics of the cold flow were measured at a distance of 0.19*d_i downstream of the burner rim by means of PIV. An overview of the experimental conditions can be found in Table 4.2. Three flows were investigated, each with a different Reynolds number corresponding to the Reynolds number used in experiment 3 for 100% NG, 50% H_2 and 100% H_2 flames. To verify that the flow is fully developed, the data will be compared to fully developed flow data from the literature. Reliable evaluation of the turbulence statistics requires averaging over

	Reynolds number [-]	**Inner diameter d_i [mm]**	**Bulk velocity [m/s]**	**Temp. [°C]**	**Pressure [kPa]**	**# Images [-]**	**Frame rate [Hz]**	**Δt laser [μs]**
Flow 1	4000	25.16	2.45	23.9	102.43	2500	50	200
Flow 2	11000	25.16	6.78	23.0	101.48	2500	150	70
Flow 3	23000	25.16	13.99	22.7	102.58	2500	450	34

Table 4.2: Overview of the experimental conditions in experiment 1

	Integral time scale τ_0 [ms]	Measurement time T [s]	Effective samples N_{eff} [-]	Relative uncertainty $\frac{\epsilon_{\bar{u}}}{\sigma_u}$ [-]	Relative uncertainty $\frac{\epsilon_{R_{xx}}}{R_{xx}}$ [-]
Flow 1	10.3	50	2434	2.0%	2.9%
Flow 2	3.7	16.7	2245	2.1%	3.0%
Flow 3	1.8	5.6	1544	2.5%	3.6%

Table 4.3: Overview of the measurement uncertainties in experiment 1

a sufficient number of frames. The absolute uncertainty ϵ for the mean velocity and the Reynolds stresses in the PIV measurements can be determined by [61]:
uncertainty of the mean velocity:

$$\epsilon_{\bar{u}} = \frac{\sigma_u}{\sqrt{N_{\text{eff}}}}, \tag{4.7}$$

where σ_u is the standard deviation, which contains both the velocity fluctuations and the measurement errors. The uncertainty in Reynolds stress is calculated by:

$$\epsilon_{R_{xx}} = R_{xx}\left(\frac{2}{N_{\text{eff}} - 1}\right)^{\frac{1}{2}}, \tag{4.8}$$

with:

$$N_{\text{eff}} = \frac{T}{2\tau_0}, \tag{4.9}$$

where N_{eff} is the effective number of independent samples, T is the measurement time and τ_0 is the integral timescale estimated with d_i/U_b. The effective number of independent samples has to be used, since the samples taken in the measurements are not statistically independent. The relative measurement uncertainty for each flow can be found in Table 4.3. As can be seen, the measurement uncertainty is the largest for the flow with the highest Reynolds number. The measurement time is here the limiting factor, as the quartz burner tube gets dirty very fast due to the seeding particles.

4.3.2. Experiment 2: Flashback map

The objective of experiment 2 is to obtain the flashback propensity of various hydrogen/natural gas/air flames in the quartz Bunsen burner. The flashback propensity is expressed in terms of the bulk velocity or the Reynolds number at which flashback occurs. An overview of the different parameters in the experiment is given in Table 4.4. Six fuel compositions were used to obtain a good comparison with the previous work of Faldella [28]. The equivalence ratios were equal to one and lower. The temperature of the burner tube was monitored using two thermocouples to ensure that the burner had reached a steady temperature. There are several ways to trigger flashback. For example, by gradually increasing the equivalence ratio at constant Reynolds number and constant fuel composition. Another way is to gradually change the fuel composition at a constant equivalence ratio and constant Reynolds number. However, to allow a good comparison with the results obtained by Faldella [28], it was chosen to perform

Fuel composition	Equivalence ratio ϕ [-]	Reynolds number	Inner diameter d_i [mm]
100% NG	0.8 - 1.0	1350 - 2850	25.16
80% NG / 20% H_2	0.8 - 1.0	3000 - 4150	25.16
60% NG / 40% H_2	0.7 - 1.0	3550 - 5750	25.16
40% NG / 60% H_2	0.6 - 1.0	4500 - 8700	25.16
20% NG / 80% H_2	0.5 - 1.0	5700 - 15300	25.16
100% H_2	0.4 - 1.0	8100 - 27850	25.16

Table 4.4: Overview of the fuel compositions and equivalence ratio's used in experiment 2.

	Reynolds number [-]	**Fuel % H_2**	**Equivalence ratio ϕ [-]**	**Bulk velocity [m/s]**	**Temp. [°C]**	**Pressure [kPa]**	**# Images**	**Frame rate [Hz]**	**Δt laser [μs]**
Flame 1	4000	0%	1	2.47	23.9	102.43	2500	50	200
Flame 2	11000	50%	1	7.23	22.5	102.55	2500	150	70
Flame 3	23000	100%	0.6	16.87	20.9	102.76	2500	450	28
Flame 4	21000	100%	0.6	15.64	23.2	102.56	2500	450	31
Flame 5	18600	100%	0.6	13.88	23.4	102.51	2500	450	32

Table 4.5: Overview of the flames used in experiment 3.

the same procedure as in his work: (1) obtain a stable flame, (2) wait until the burner has reached a steady temperature and finally (3) gradually lower the Reynolds number. When reducing the Reynolds number, the fuel and air flows were decreased simultaneously in small steps to maintain a constant equivalence ratio. Steps (2) and (3) were repeated until the flame flashes back into the burner. For each fuel composition, the experiment was repeated three times for each equivalence ratio to ensure an accurate measurement.

4.3.3. Experiment 3: Influence flame on flow characteristics

In this experiment the mean velocity profiles and turbulent statistics in the presence of a flame were obtained using PIV. In Table 4.5 the overview of the different flames are shown. The experiment had two objectives. The first objective was to determine whether the stable unconfined flame affects the mean velocity profile in the tube. Thereby, it was investigated whether the fuel composition also plays a role. The influence of the flame was determined by comparing the velocity profiles of the cold flow to those of the reacting flow at a distance of $0.12d_i$ inside the tube. To allow a good comparison, the Reynolds numbers for flames 1, 2 and 3 in this experiment were the same as those in flows 1, 2 and 3 in experiment 1. The second objective of this experiment was to determine whether the transition of a stable flame to an unstable flame close to flashback has an effect on the mean velocity profile inside the burner tube. The influence of the flame on the Reynolds stresses is also considered here. This was done via comparison of flames 3, 4, and 5. The difference between these successive flames is a decreasing Reynolds number. Flame 3 is a stable flame, while flame 5 is an unstable flame close to flashback.

4.3.4. Experiment 4: Flashback process

In the last experiment the flashback process was visualized for both a 100% natural gas flame and a 100% H_2 flame using both PIV and Mie-scattering measurements. The objective was to understand why and how flashback is triggered; how the flame propagates upstream above the burner rim and how it propagates once it has reached the inside of the burner tube. Previous studies from Faldella [28] and Lambers [43] show that the transient flashback process of an unconfined 100% natural gas flame takes 4 ms and a 100% H_2 flame only needs 1 ms. To capture this fast transient process, the camera operated in double frame, double exposure mode with a frame rate of 2 kHz for 100% natural gas flames. For 100% H_2 flames the camera operated in single frame, single exposure mode with a frame rate of 10 kHz. Such high frame rates are however not possible with the full sensor of 1024x1024 pixels. To achieve the high frame rates, the images were cropped to 1024x512 pixels.

5

Results and Analysis

This chapter presents the results that are obtained in the four experiments described in chapter 4. First, the validation for fully developed turbulent pipe flow will be presented in Section 5.1. Then the flashback map is discussed in Section 5.2. In Section 5.3 the statistics of the reacting flow field is analysed for three different fuel compositions including a pure hydrogen flame which is brought to flashback conditions. Finally, in Section 5.4 the instantaneous flashback process will be shown and discussed in detail.

5.1. Experiment 1: Validation for fully developed turbulent pipe flow

For the validation of the flashback map, the statistics of the reacting flow and for the flashback process it is necessary to have a fully developed turbulent pipe flow. To determine whether the flow in the burner tube is fully developed, PIV is used to obtain profiles of the mean velocity ($\overline{u}$) and the Reynolds stresses ($\overline{u'u'}$ and $\overline{u'v'}$). The current measurements are done with a quartz tube with an inner diameter d_i = 25.16 mm at three different Reynolds numbers: Re = 4000, Re = 11000 and Re = 23000.

The results are plotted in Figure 5.1 and are compared with LDA measurements from Tummers et al. [64]. On the horizontal axes, the radius of the quartz burner tube has been normalized with the inner diameter d_i. On the vertical axes the mean velocity and the Reynolds stresses are both normalized by the bulk velocity U_b. Figure 5.1a shows that the measured mean velocity profiles match the mean velocity profile from literature very well. It can be seen that with increasing Reynolds number the velocity profile flattens and becomes wider as expected.

The obtained axial and radial Reynolds stresses ($\overline{u'u'}$ and $\overline{u'v'}$) in the Figures 5.1b, 5.1c coincides well with literature. The difference in the distribution of $\overline{u'u'}$ reflects the thinning of the boundary layer with increased Reynolds number as observed by Pollard et al. [29]. The shear Reynolds stress ($\overline{u'v'}$) goes to zero at the centreline as expected. Some differences between the LDA measurements and the PIV measurements in Figure 5.1c can be found, namely the peak values of $\overline{u'v'}$ at $r/d_i = \pm 0.5$. At these distances the values from the current PIV measurements at Re = 23000 are 20% lower than the LDA measurements from Tummers et al. [64]. This is due to the effect that PIV is less accurate than LDA when it comes to high velocity gradients. Also, the surrounding air in the experiment of Tummers et al. [64] was seeded, which was not done during this experiment and thus could not be measured. Despite these differences, it can be concluded that the flow within the quartz tube is a fully developed turbulent flow.

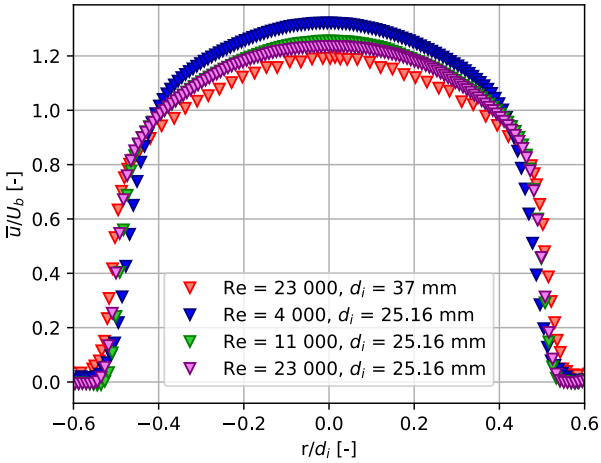

(a) The normalized mean axial velocity $\overline{u}/U_b$ profile measured at a distance of 0.19d_i downstream of the tube exit. The reference LDA data is from Tummers et al. [64] for a tube inner diameter of d_i = 37 mm at Re = 23000.

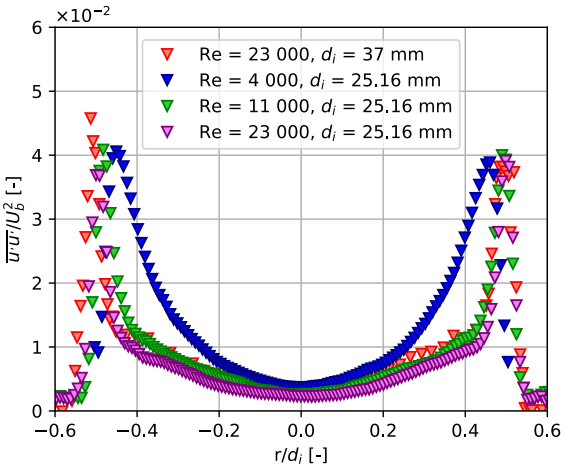

(b) The normalized Reynolds stress in axial direction $\overline{u'u'}/U_b$ measured at a distance of 0.19d_i downstream of the tube exit. The reference LDA data is from Tummers et al. [64] for a tube inner diameter of d_i = 37 mm at Re = 23000.

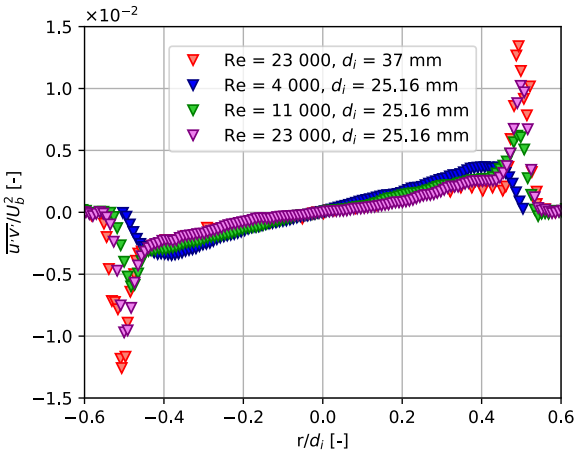

(c) The shear Reynolds stress $\overline{u'v'}$ measured at a distance of 0.19d_i downstream of the tube exit. The reference LDA data is from Tummers et al. [64] for a tube inner diameter of d_i = 37 mm at Re = 23000.

Figure 5.1: The normalized mean axial velocity $\overline{u}$ profile and the normalized Reynolds stresses ($\overline{u'u'}$ and $\overline{u'v'}$) measured at a distance of 0.19d_i downstream of the tube exit. Current PIV measurements are performed with a tube inner diameter of d_i = 25.16 mm at Re = 4000, Re = 11000 and Re = 23000. The reference LDA data is from Tummers et al. [64] performed with a tube inner diameter of d_i = 37 mm.

5.2. Experiment 2: Flashback map

The flashback propensity of different fuel-air mixtures in the quartz burner is shown in three flashback maps, see Figures 5.2a, 5.2b and 5.3b. In the flashback map shown in Figure 5.2a, the flashback propensity is expressed as the bulk velocity at which flashback occurs U_b as a function of the equivalence ratio ϕ. In the Figures 5.2b and 5.3b the flashback propensity is presented in terms of the Reynolds number and the ratio between the bulk velocity and the unstretched laminar flame speed ($U_b/s_{l,0}$), where $s_{l,0}$ is calculated by using Cantera. In the experiment six different fuel compositions are considered ranging from pure natural gas (0% H_2) to pure hydrogen (100% H_2). For a given mixture, the area above the line denotes a stable flame regime up to the blow-off limit (not shown here), while the area below the line denotes the flashback regime. However, these areas do not have sharp boundaries. Flashback is a statistical phenomena as will be discussed in Section 5.4.4, so the lines drawn here have some kind of bandwidth in which the flashback event may occur.

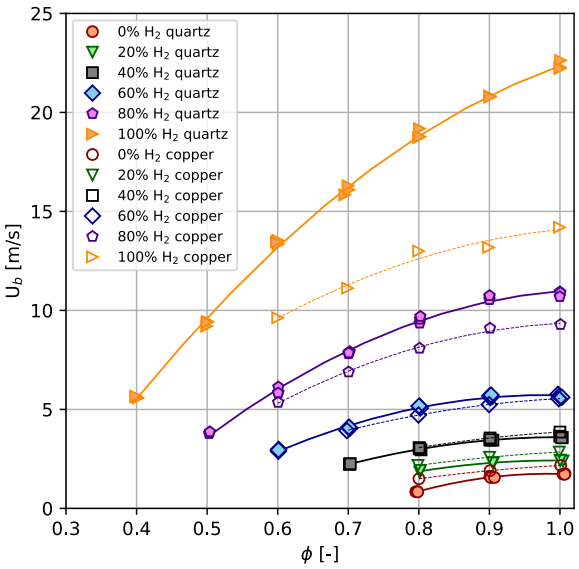

(a) Bulk velocity at flashback as a function of the equivalence ratio for six different fuel compositions. The open symbols denote the flashback data for an uncooled copper burner tube taken from Faldella[28].

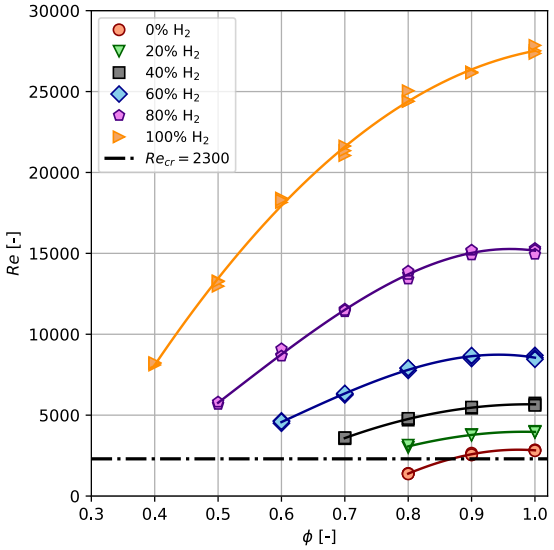

(b) Reynolds number of the bulk flow at flashback as a function of the equivalence ratio for six different fuel compositions. The dashed line shows the critical Reynolds number (Re_{cr} = 2300) at which laminar flow becomes turbulent flow.

Figure 5.2: **(a)** Bulk velocity at flashback and **(b)** Reynolds number of the bulk flow at flashback as a function of the equivalence ratio for six different fuel compositions, ranging from pure natural gas (0% H_2) to pure hydrogen (100% H_2).

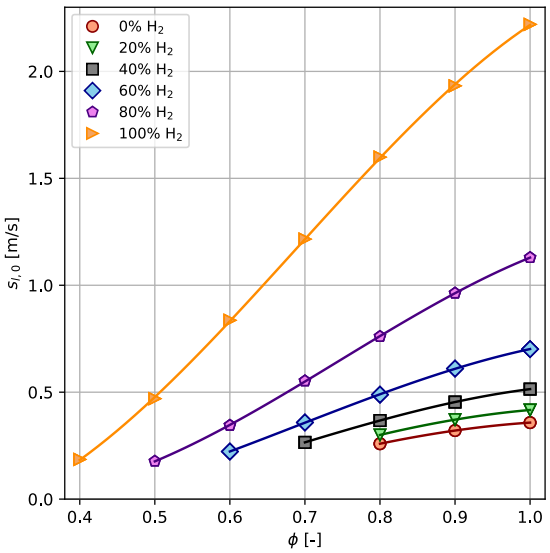

(a) Unstretched laminar flame speed as a function of the equivalence ratio for six different fuel compositions. The unstretched laminar flame speed is calculated from Cantera using the GRI 3.0 model for the fuel compositions up to 80% H_2. For pure hydrogen the Ó Conaire reaction mechanism [51] was used.

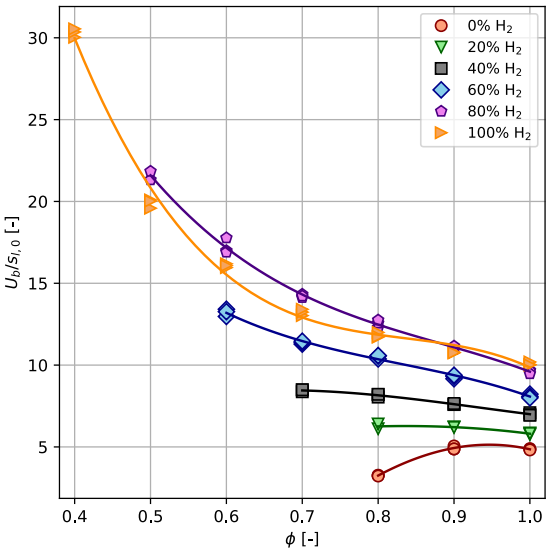

(b) Bulk velocity at flashback normalized with the unstretched laminar flame speed from Figure 5.3a as a function of the equivalence ratio for six different fuel compositions.

Figure 5.3: **(a)** Unstretched laminar flame speed $s_{l,0}$ and **(b)** the normalized bulk velocity at flashback ($U_b/s_{l,0}$) as a function of the equivalence ratio for six different fuel compositions, ranging from pure natural gas (0% H_2) to pure hydrogen (100% H_2).

The flashback map in Figure 5.2a shows that for mixtures with 80% hydrogen or higher, the quartz burner tube is much more prone to flashback in comparison to the uncooled copper burner tube used by Faldella [28]. This difference between two burner materials is also observed by Duan et al. [22], who performed a study on the effect of burner material and burner tip temperature on the flashback propensity of pure hydrogen-air flames. The conclusion of that study was that the lower thermal conductivity

of quartz is one of the reasons for the increased flashback propensity. The low thermal conductivity of quartz leads to slightly higher burner tip temperatures, which allows the flame to anchor closer to the burner rim and thus the tendency of the flame to propagate upstream becomes higher. However, only the slight increase in burner tip temperature does not explain the large difference in flashback propensity [22]. It remains also unclear why the difference in flashback propensity only occurs for mixtures with a high percentage of hydrogen.

Figure 5.2a clearly shows that the hydrogen addition in the fuel leads to a significantly higher flashback propensity, e.g. at $\phi = 1$ the ratio in bulk velocity at flashback for pure natural gas and pure hydrogen is more than 10. It can also be seen that there is a non-linear increase in flashback propensity for every 20% hydrogen addition in the fuel. Comparing Figure 5.2a with Figure 5.3a, it can be seen that the non-linear increase in flashback propensity is related to the non-linear increase in unstretched laminar flame speed of the different mixtures. However, Figure 5.3b shows that the ratio between the bulk velocity at flashback and the unstretched laminar flame speed ($U_b/s_{l,0}$) is not the same for every mixture. For example, for the pure natural gas flame with an equivalence ratio of $\phi = 0.8$ the ratio $U_b/s_{l,0}$ is about two times lower than for the pure natural gas flame with an equivalence ratio of $\phi = 0.9$ or 1. Figure 5.2b shows that for $\phi = 0.8$, the Reynolds number at flashback is lower than 2300, which means that the flow is laminar. During the experiments this was clearly visible as the flame took a conical shape with no wrinkles as illustrated in Figure 2.7b. The flashback propensity of a laminar flame is much lower than that of a turbulent flame [39], which explains the significant drop in ratio of $U_b/s_{l,0}$. Figure 5.3b also shows that for fuels with a high hydrogen content the ratio $U_b/s_{l,0}$ strongly increases with decreasing equivalence ratio.

5.2.1. Flame regimes

For the analysis of the strong increase in $U_b/s_{l,0}$ for fuels with high hydrogen content at low equivalence ratios, shown in Figure 5.3b, it is important to know the flame regimes of the considered flames in experiment 2. As discussed in Section 2.5.1, this can be determined by four parameters: the integral length scale ℓ_0, the laminar flame thickness δ_f, the velocity fluctuations in the unburned mixture $\overline{u'}$ and the laminar flame speed $s_{l,0}$.

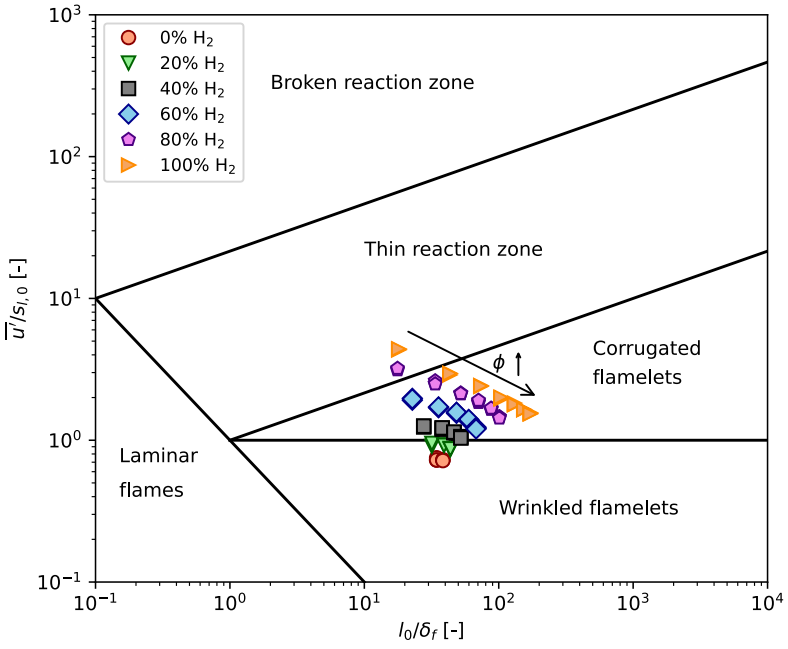

Figure 5.4: Flame regimes of the flames considered in Experiment 2. The laminar natural gas (ϕ = 0.8) flame is not shown. For the definition of the different regimes, see Section 2.5.1.

According to Nieuwstadt et al. [50], the integral length scale in the core region of a turbulent pipe flow can be estimated by:

$$\ell_0 = 0.13\frac{d_i}{2}. \tag{5.1}$$

The laminar flame thickness is determined using Eq. (2.26), where the mass diffusivity D is replaced by the viscosity of the mixture ν, since a Schmidt number ($Sc = \nu/D$) of unity is assumed. The velocity fluctuations at the burner exit are the largest in axial direction and are located close to the wall, see Figure 5.1. From Figure 5.1b it can be determined that the maximum velocity fluctuations are $\overline{u'} = (0.004U_b^2)^{1/2}$. This results in a turbulence intensity of $I = \overline{u'}/U_b = 0.02$. However, as is shown in Figure 5.8 in Section 5.3.2 and also by Baumgartner [11], the turbulent intensity decreases as the unburned mixture reaches the flame. Therefore, a turbulence intensity $\overline{u'}/U_b = 0.015$ is used as an estimate. Figure 5.4 shows the resulting flame regimes diagram.

It can be seen that the flame regimes of the flames in experiment 2 range from the wrinkled flamelets to the thin reaction zones. As already mentioned in Section 2.5.1, this has to be interpreted as an indication instead of the exact determination of the type of flame, since a lot of assumptions are made. So, the flame regime map indicates that, especially for fuels with a high hydrogen content, the very lean mixtures are in the thin reaction zone close to the corrugated flamelet regime. In contrast to the corrugated flamelet regime, the turbulent eddies are now able to penetrate into the preheat zone of the flame. This will enhance the transport of the reactants and increase the flame speed, as discussed Section 2.5.2. This could be a reason for the strong increase in the ratio $U_b/s_{l,0}$ for the very lean flames with a high hydrogen content. It is suggested that the main reason can be found in the thermal-diffusive properties of the lean hydrogen flames. A lean hydrogen flame has a negative Lewis number (Le < 1) and the mass diffusion of hydrogen is much higher than oxygen, which means that the flame is thermal-diffusive unstable. The thermal-diffusive instability becomes more apparent for leaner hydrogen flames. This leads to much higher flame speeds, even in flames with a high turbulent intensity, as described in Section 2.5.2.

5.3. Experiment 3: Influence flame on flow characteristics

5.3.1. Average flame front

This section presents how the location of the average flame front is determined. The location of the average flame front is needed for the discussion in section 5.3.2. As discussed in 4.2.1, Mie-scattering can be used to determine the flame front. The large difference in seeding density denotes the flame front. This is quantified in the Mie-scattering images by means of the large difference in Mie-scattering intensity. The determination of the average flame front is based on the principle used by Faldella [28]. The Mie-scattering intensity is averaged over 2500 images to obtain the time-averaged signal intensity, see Figure 5.5a. The time-averaged signal at three lines A, B and C in Figure 5.5a are shown in Figure 5.6. The scattered average signal is filtered by a simple moving average filter to obtain a smooth curve. The flame width is then defined as the width of the signal at 50% of the maximum intensity. This procedure is repeated for 20 equally spaced horizontal lines to obtain the shape of the average flame front. Figure 5.5b shows the result.

	Reynolds number [-]	**Fuel % H_2**	**Equivalence ratio ϕ [-]**	**Bulk velocity [m/s]**	**Temp. [°C]**	**Pressure [kPa]**	**# Images**	**Frame rate [Hz]**	**Δt laser [μs]**
Flame 1	4000	0%	1	2.47	23.9	102.43	2500	50	200
Flame 2	11000	50%	1	7.23	22.5	102.55	2500	150	70
Flame 3	23000	100%	0.6	16.87	20.9	102.76	2500	450	28
Flame 4	21000	100%	0.6	15.64	23.2	102.56	2500	450	31
Flame 5	18600	100%	0.6	13.88	23.4	102.51	2500	450	32

Table 5.1: Overview of the different flames used in experiment 3 to determine the influence of the flame on the flow characteristics. (repeated from page 36)

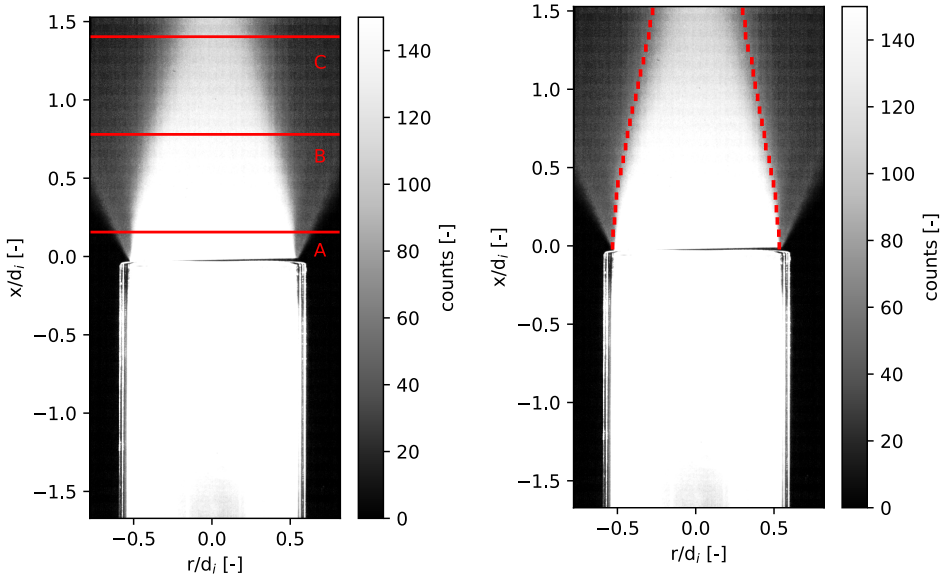

(a) Time-averaged Mie-scattering intensity of the flame. The averaged signal intensities corresponding to the lines A, B and C are shown in Figure 5.6.

(b) Time-averaged Mie-scattering intensity. The red dashed lines denote the average flame front. The flame width is defined as the width of the signal at 50% of the maximum intensity.

Figure 5.5: Time-averaged Mie-scattering intensity of the flame. The Mie-scattering images are averaged over 2500 images.

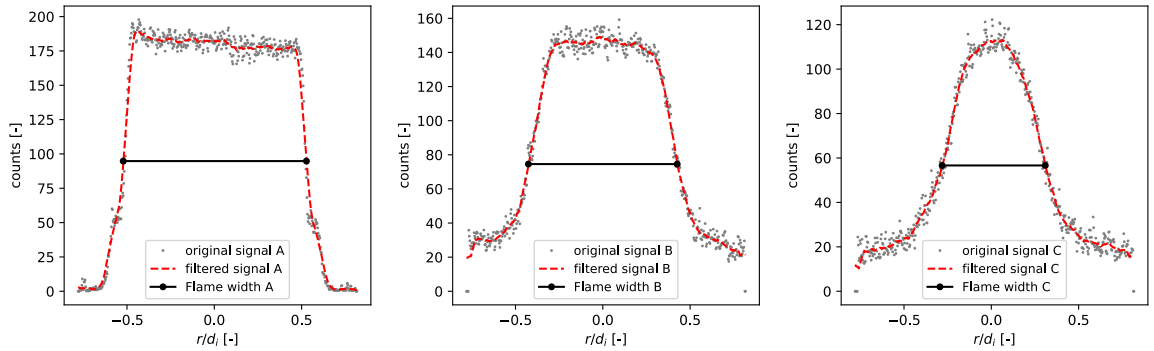

(a) Time-averaged Mie-scattering intensity along line A

(b) Time-averaged Mie-scattering intensity along line B

(c) Time-averaged Mie-scattering intensity along line C

Figure 5.6: Time-averaged Mie-scattering intensity corresponding to the lines A, B and C from Figure 5.5a. The red dashed lines denote the signal after applying a moving average filter. The black lines denote the width of the flame.

5.3.2. Influence flame on flow characteristics

In this section the influence of the flame on the flow inside and outside of the burner is presented in two parts: In the first part, the influence of a stable unconfined flame on the velocity profile at a distance of $0.12d_i$ upstream of the burner rim is determined through a comparison of the velocity profile of cold flow and reacting flow at the same Reynolds number. Three different fuel compositions are used in order to determine whether hydrogen addition to natural gas results in a stronger effect on the flow inside the tube. In the second part, it is discussed whether the transition of a stable flame to an unstable flame close to flashback has an influence on the mean velocity profile inside the tube and on the Reynolds stresses in the flow outside the tube. An overview of the flames considered is given in Table 5.1.

Figures 5.7a - 5.7c show the mean velocity profiles of cold flows and of reacting flows with 0%, 50% and 100% hydrogen content in the fuel, respectively. The flashback maps that were presented in Section 5.2 show that an increasing amount of hydrogen in the fuel strongly increases the flashback propensity of the flame. So, it is expected that the pure hydrogen flame has a higher backpressure effect on the flow, which may lead to an observable degree of mean flow retardation. However, from

the measurements in Figures 5.7a - 5.7c no difference in the mean velocity profiles of the cold flow and that of the reacting flow inside the tube is observed, even for the pure hydrogen flame. Similar to what Baumgartner [11] observed, this means that the backpressure of a stable unconfined flame is not strong enough to interact with the flow inside the tube.

The next question is whether this is also true for a flame that is brought close to flashback conditions. Therefore, a pure hydrogen flame with $\phi = 0.6$ is brought to flashback conditions via reducing the Reynolds number of the flow. Figure 5.7d shows the corresponding velocity profiles at three different Reynolds numbers. At Re = 18 600 the flame is very close to flashback, see Figure 5.2b. Still, no influence of the flame on the mean velocity profile of the flow inside the tube is observed. This is an important result as it indicates that flashback cannot be predicted via measurements in the mean flow inside the burner tube.

Clearly, there are no significant effects on the the mean velocity profile inside the tube when a stable unconfined flame brought close to flashback. However, this does not hold for the flow downstream of the burner exit. The difference between a stable flame and a flame close to flashback is the most visi-

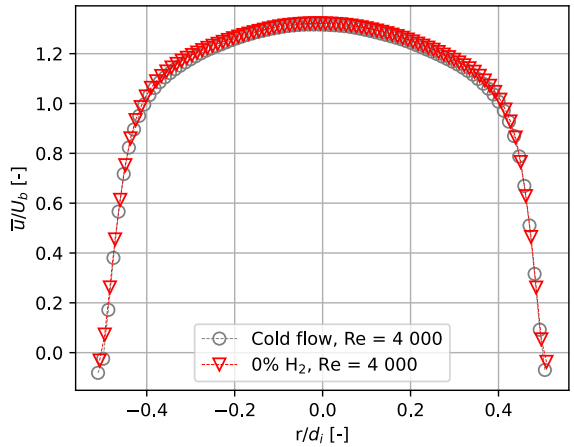

(a) The normalized mean axial velocity $\overline{u}/U_b$ profiles of the cold flow and the reacting flow of pure natural gas (0% H_2) at Re = 4 000. Measured at a distance $0.12d_i$ upstream of the tube exit.

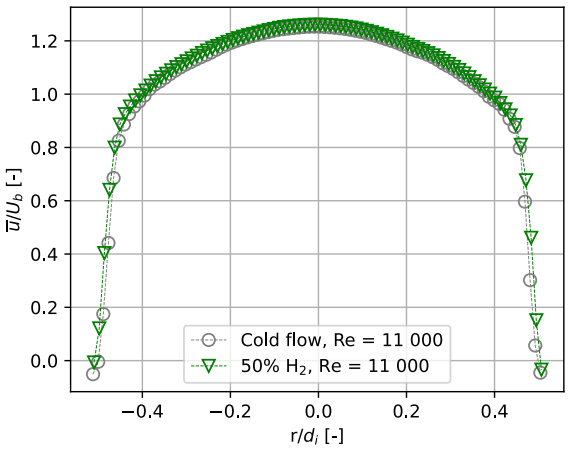

(b) The normalized mean axial velocity $\overline{u}/U_b$ profiles of the cold flow and the reacting flow a mixture of 50% natural gas and 50% hydrogen at Re = 11 000. Measured at a distance $0.12d_i$ upstream of the tube exit.

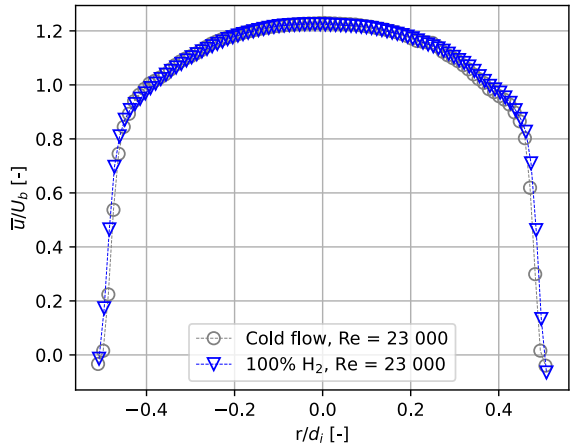

(c) The normalized mean axial velocity $\overline{u}/U_b$ profiles of the cold flow and the reacting flow of pure hydrogen gas(100% H_2) at Re = 23 000. Measured at a distance $0.12d_i$ upstream of the tube exit.

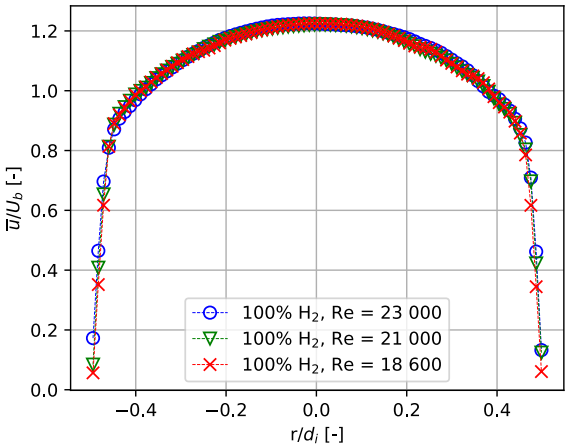

(d) The normalized mean axial velocity $\overline{u}/U_b$ profiles of the reacting flow of pure hydrogen gas (100% H_2) at Re = 23 000, 21 000 and 18 600. Re = 18 600 is close to flashback conditions. Measured at a distance $0.12d_i$ upstream of the tube exit.

Figure 5.7: Comparison of normalized mean velocity profiles ($\overline{u}/U_b$) of cold flow and reacting flow for different fuel compositions in Figures 5.7a-5.7c. Figure 5.7d shows the comparison of normalized mean velocity profiles ($\overline{u}/U_b$) of pure hydrogen the reacting flow at three different Reynolds numbers.

ble in the normalized Reynolds stresses in the flow. Figures 5.8 and 5.9 show the normalized Reynolds stresses in axial ($\overline{u'u'}/U_b$) and radial ($\overline{v'v'}/U_b$) direction, respectively, for a pure hydrogen flame brought to flashback.

The axial Reynolds stress ($\overline{u'u'}/U_b^2$) shows two regions of high magnitude downstream of the burner rim. The first region close to the burner rim is a continuation of the high Reynolds stress region inside the tube in the vicinity the wall. It is interesting to see that this region is not straight as would be the case for a cold flow, see Figure 5.10. Instead, it is curved towards the centerline of the tube and also the magnitude decreases further downstream of the burner rim. Figure 5.8 shows that the average flame front is located just slightly outside the first region of high axial Reynolds stress. The second region further downstream with a high magnitude in the axial Reynolds stresses is due to the intermittent behaviour of the flame front [56]. To understand this, consider a stationary point in time located on the average flame front, which will be the so-called Eulerian frame of reference. At certain times the instantaneous flame front will be located above the average flame front, meaning that the stationary point is located in the unburned gases. The opposite will be true for other moments in time, where the stationary point is located in the burned gases. The velocity difference between the unburned gases and the burned gases is high due to the acceleration of the burned gases resulting from the thermal expansion. Consequently, significant velocity fluctuations in both the axial and radial direction are observed in the stationary point and thus in the region of the average flame front, see Figures 5.8 and 5.9.

Comparing Figures 5.8a, 5.8b and 5.8c and also comparing Figures 5.9a, 5.9b and 5.9a, it can be seen that the area of high magnitude of the normalized Reynolds stresses ($\overline{u'u'}/U_b^2$ and $\overline{v'v'}$) increases as the Reynolds number decreases. For Reynolds numbers well above the flashback limit e.g. Re = 23 000, the hydrogen flame is stable. This means that, due to the high bulk velocity, the velocity fluctuations in the unburned mixture do not cause large scale wrinkles on the flame front and thus the flame front will stay in more or less the same location. As a consequence, the acceleration of the burned gas occurs in more or less the same location. This results in a small region of high velocity fluctuations and as can be seen in the Figures 5.8a and 5.9a. In Figures 5.8c and 5.9c the Reynolds number is decreased to 18 600. Consequently, the flame becomes unstable, which means that now the velocity fluctuations in the unburned mixture do have a larger effect on the flame front. The intrinsic flame instabilities like the thermal-diffusive instability do now have more time to grow before they are advected by the bulk flow. As a result, the flame becomes more wobbly and the location of the frame front will be spread over a larger area and with the same reasoning as above, this leads to an increased area of high Reynolds stresses in both the axial and radial direction.

Besides an increase in area of high Reynolds stresses, the magnitude of the Reynolds stresses in

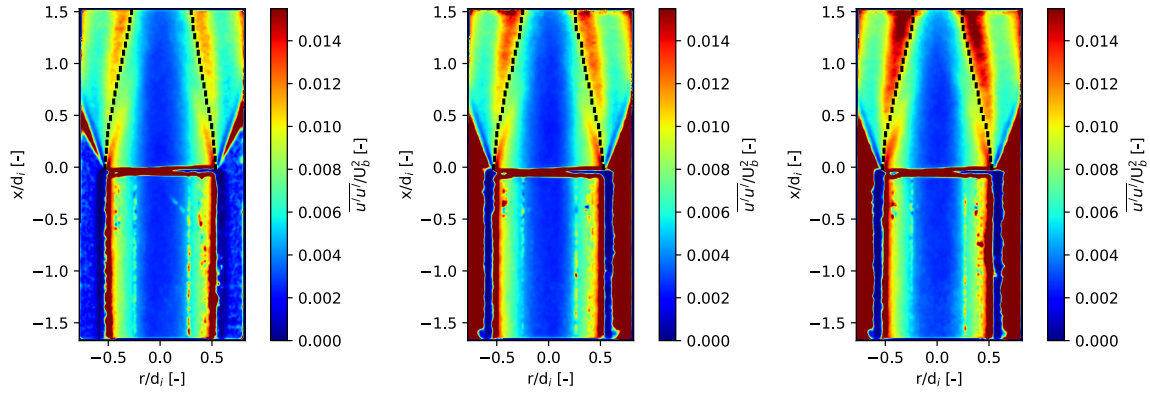

(a) Normalized Reynolds stresses in axial direction $\overline{u'u'}/U_b^2$ at Re = 23000

(b) Normalized Reynolds stresses in axial direction $\overline{u'u'}/U_b^2$ at Re = 21000

(c) Normalized Reynolds stresses in axial direction $\overline{u'u'}/U_b^2$ at Re = 18600

Figure 5.8: A lean ($\phi = 0.6$) 100% hydrogen flame brought to flashback conditions via reducing the Reynolds number: comparison of the normalized Reynolds stresses in axial direction $\overline{u'u'}/U_b^2$. The burner exit is at $x/d_i = 0$. The black dashed lines show the average flame front.

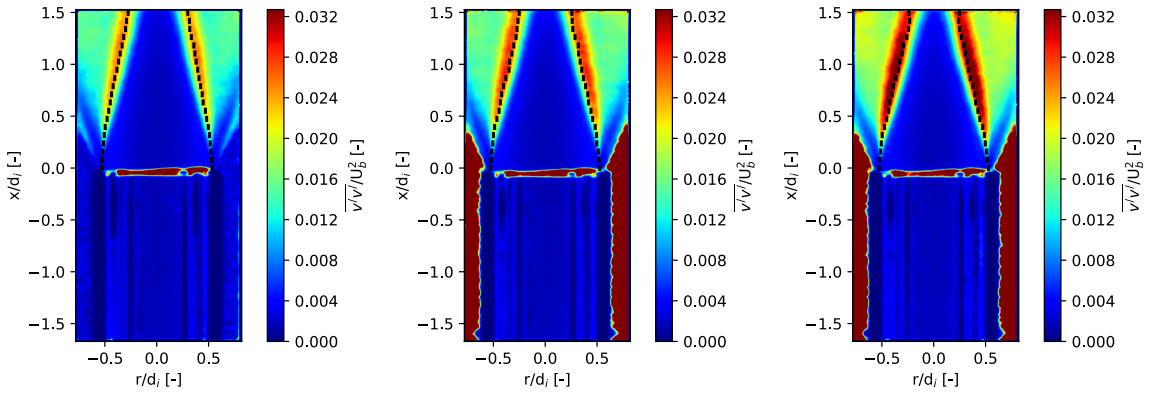

(a) Normalized Reynolds stresses in radial direction $\overline{v'v'}/U_b^2$ at Re = 23000

(b) Normalized Reynolds stresses in radial direction $\overline{v'v'}/U_b^2$ at Re = 21000

(c) Normalized Reynolds stresses in radial direction $\overline{v'v'}/U_b^2$ at Re = 18600

Figure 5.9: A lean ($\phi = 0.6$) 100% hydrogen flame brought to flashback conditions via reducing the Reynolds number: comparison of the normalized Reynolds stresses in radial direction $\overline{v'v'}/U_b^2$. The burner exit is at $x/d_i = 0$. The black dashed lines show the average flame front.

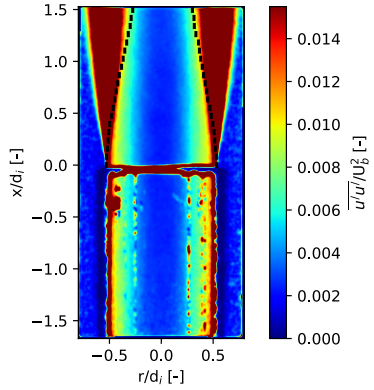

Figure 5.10: Normalized Reynolds stresses in axial direction $\overline{u'u'}/U_b^2$ of a cold flow at Re = 23000. The black dashed lines show the average flame front from Figure 5.8a.

the region of the flame front also increases as the Reynolds number is decreased. This increase in magnitude can be explained by a simple kinematic balance over the flame as described in Section 2.2.2. As the Reynolds number decreases, the average flame cone angle increases, which can clearly be seen comparing Figure 5.8a with Figure 5.8c. As the unburned gases reach the flame front, the component of the velocity normal to the flame front undergoes the acceleration due to the expansion of the burned gases, whereas the tangential component remains the same. By increasing the flame angle, the more the flame front is angled perpendicular towards the axial flow direction. Some basic vector analysis shows that this leads to a higher acceleration across the flame front in both the axial and radial direction for an average flame angle between 0°and 45°. Again, consider a stationary point in time located on the average flame front. For a lower Reynolds number the instantaneous flame front has, on average, a larger angle with the unburned gases. As explained, this leads to a higher velocity difference between the unburned and the burned gases. As the instantaneous flame front moves in time past the stationary point, this will result in a higher observed velocity fluctuation. Hence, a higher magnitude of the Reynolds stresses is observed. Both the increase in area and magnitude of Reynolds stresses for a reduced Reynolds number are also observed in the study of Faldella [28].

5.4. Experiment 4: Flashback process of turbulent flames

This section shows the results of the instantaneous flashback process. The initial phase of the flashback process, called unconfined flashback, starts when the flame is still anchored at the burner rim.

From the statistics shown in Figure 5.9 it is clear that the flame angle is increased and that the flame burns more closely to the burner rim. However, from the statistics it can not be determined what leads to the initiation of the flashback process. Therefore, the instantaneous flashback process has been visualized to obtain knowledge about the onset of flashback. The visualisation is done by using the Mie-scattering images from the planar PIV as discussed in Section 4.2.1.

Visualizing the flashback process by using planar PIV in combination with the quartz burner tube has limitations. First, to visualize the flow, a significant amount of seeding particles have to be released in the flow. The higher Reynolds number used in the experiment, the more seeding particles per unit of time pass through the burner tube to maintain the same seeding density. This poses a problem for the flashback visualisation in terms of the quartz burner tube wall getting dirty because of the deposition of the aluminum oxide particles. Especially for hydrogen this is a limiting factor, since hydrogen flames require high flow velocities to remain stable. To limit this side effect and still be able to investigate the flashback process of natural gas and hydrogen, it was decided to use a stoichiometric ($\phi = 1$) 100% natural gas flame and a very lean ($\phi = 0.4$) 100% hydrogen flame. The flames are turbulent and have a laminar flame speed $s_{l,0}$ of 0,36 m/s and 0,19 m/s, respectively.

A second limitation of planar PIV is the fact the flashback process is a three-dimensional phenomenon. Flashback can be triggered by a so-called tripwire, which disturbs the flow leading to the flame flashing back. However, this is however undesired, because a tripwire will block part of the incoming laser sheet and it will also interact with the flame when the flame propagates into the burner [43]. To overcome this limitation, the experiments have been repeated 20 times for each flame. From careful examination of the Mie-scattering images and velocity fields it is determined whether the flashback process is within the PIV plane. However, still some precaution has to be taken into account as this cannot be ensured with 100% confidence.

The flashback process is presented here using the Mie-scattering images and the obtained velocity fields. The images are shown in chronological order where the the first images denotes the start of the flashback process at $t = 0$. The Mie-scattering images are used to determine the flame front.
The flashback process is divided into two different regions: unconfined flashback and confined flashback. Unconfined flashback denotes the onset of flashback, where the flame is propagating from the outside of the burner tube to the inside. Once the flame is propagating inside the burner tube it is referred to as confined flashback, see also Sections 3.2.2 and 3.2.3.

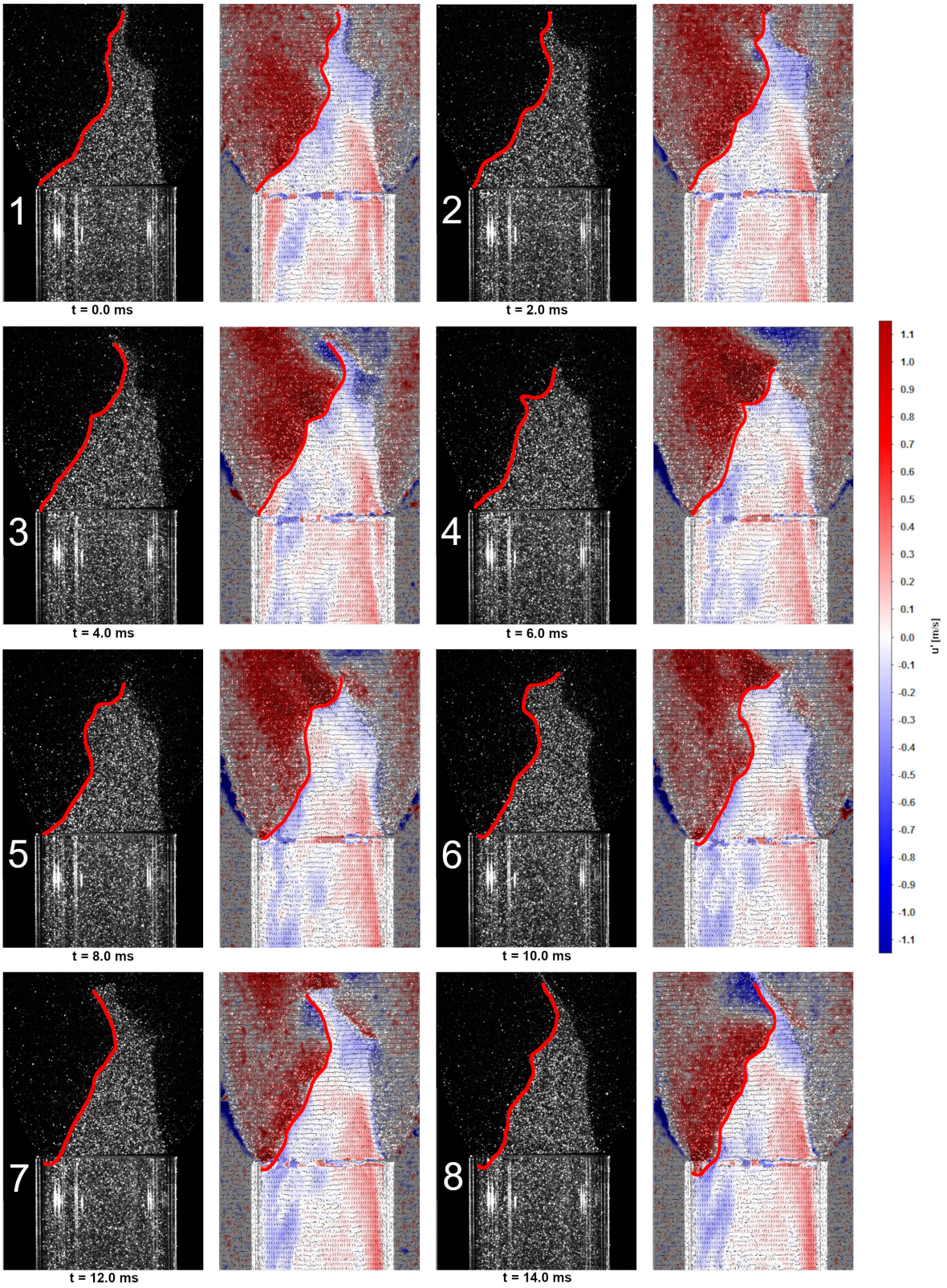

Figure 5.11: Visualisation of the unconfined flashback process for a stoichiometric ($\phi = 1$) 100% natural gas flame. Flashback starts here on the left-hand side of the burner tube. Eight sequential image pairs are shown, each with a time interval of 2 ms. The image pair consists of a Mie-scattering image on the left-hand side and the corresponding axial velocity fluctuations u' on the right-hand side. The flame front is marked with a red line.

5.4.1. Unconfined flashback process

The unconfined flashback process of a natural gas flame and a hydrogen flame can be seen in Figures 5.11 and 5.12, respectively. Eight sequential image pairs are shown, each with a time interval of 2 ms for the natural gas flame and 0.8 ms for the hydrogen flame. Each image pair consists of a Mie-scattering image on the left-hand side and the corresponding axial velocity fluctuations u' on the right-hand side. The flame front in every image is marked with a red line. The velocity fluctuations are obtained by subtracting the average velocity field from the instantaneous velocity field. The red and the blue areas in the axial velocity fluctuations images mean a positive and a negative velocity fluctuation, respectively. First the onset of flashback for the natural gas flame is treated, see Figure 5.11. It can be seen in the images 1-3 of Figure 5.11 that the flame interacts with the positive velocity fluctuations. To maintain the kinematic balance between the incoming flow and the flame speed, as described in Section 2.2.2, the flame angle needs to decrease. This can clearly be seen by comparing image 1 and 3. So effectively, the flame is pushed away from the burner rim by the positive velocity fluctuation.

Moving on to image 4, the flame starts to interact with the negative velocity fluctuation. Due to the lower velocity of the incoming mixture, the flame starts to form a small convex bulge towards the reactants. Comparing image 4 with image 3, it can be seen that the small bulge increases the magnitude of the negative velocity fluctuations. As described in Section 2.4.1 this has to do with the hydrodynamic flame instability. Following the bulge in images 4-8 it can be seen that the hydrodynamic instability causes the bulge to grow in time. However, the bulge is advected from the burner rim by the incoming flow. Comparing image 4 with image 1, the angle of the flame on the left-hand side of the burner rim looks quite similar. The only difference is that there is no positive velocity fluctuation to counteract the large cone angle of the flame. As a result, the flame is able to move even closer to burner rim as can be seen in image 5. From the kinematic balance over the flame it can be shown that a larger cone angle of the flame leads to a higher flow acceleration across the flame. As a consequence the flame induces a higher adverse pressure gradient leading to more retardation of the flow in front of the flame as is shown by Van Put [66]. So, the combination of this effect and the negative velocity fluctuations causes the flame to move upstream into the tube as can be seen in image 6. The flame front forms again a convex shape into the unburned mixture and as discussed earlier, the intrinsic hydrodynamic flame instability is causing the flow to be even more retarded and the flame is able to move further into the tube. The time needed for this whole process is only 14 ms, which shows that flashback is a rapid transient phenomenon. In contrast to what Baumgartner [11] observed, is the onset of unconfined flashback not at some distance downstream of the burner rim, but at the burner rim.

A similar flashback process is found for the pure hydrogen flame, which can be seen in Figure 5.12. This time the flashback process starts at the right-hand side of the burner, which illustrates the stochastic behaviour. Again, in images 1-3 a region with positive velocity fluctuations pushes the flame outwards. At image 4 the negative velocity fluctuations starts to interact with the flame leading to the formation of a convex bulge in image 5. The flame loses its anchoring position and instantly propagates into the burner, see images 6-8. If we compare this with the flashback process of the natural gas flame, it can be seen that the hydrogen flame propagates much faster into the burner. The time needed to propagate into the burner is about 3 times less than for the natural gas flame, even though the laminar flame speed of the hydrogen flame (= 0.19 m/s) is about two times lower than the laminar flame speed of the natural gas flame (= 0.36 m/s), see Figure 5.3a. This will be further elaborated in Section 5.4.3.

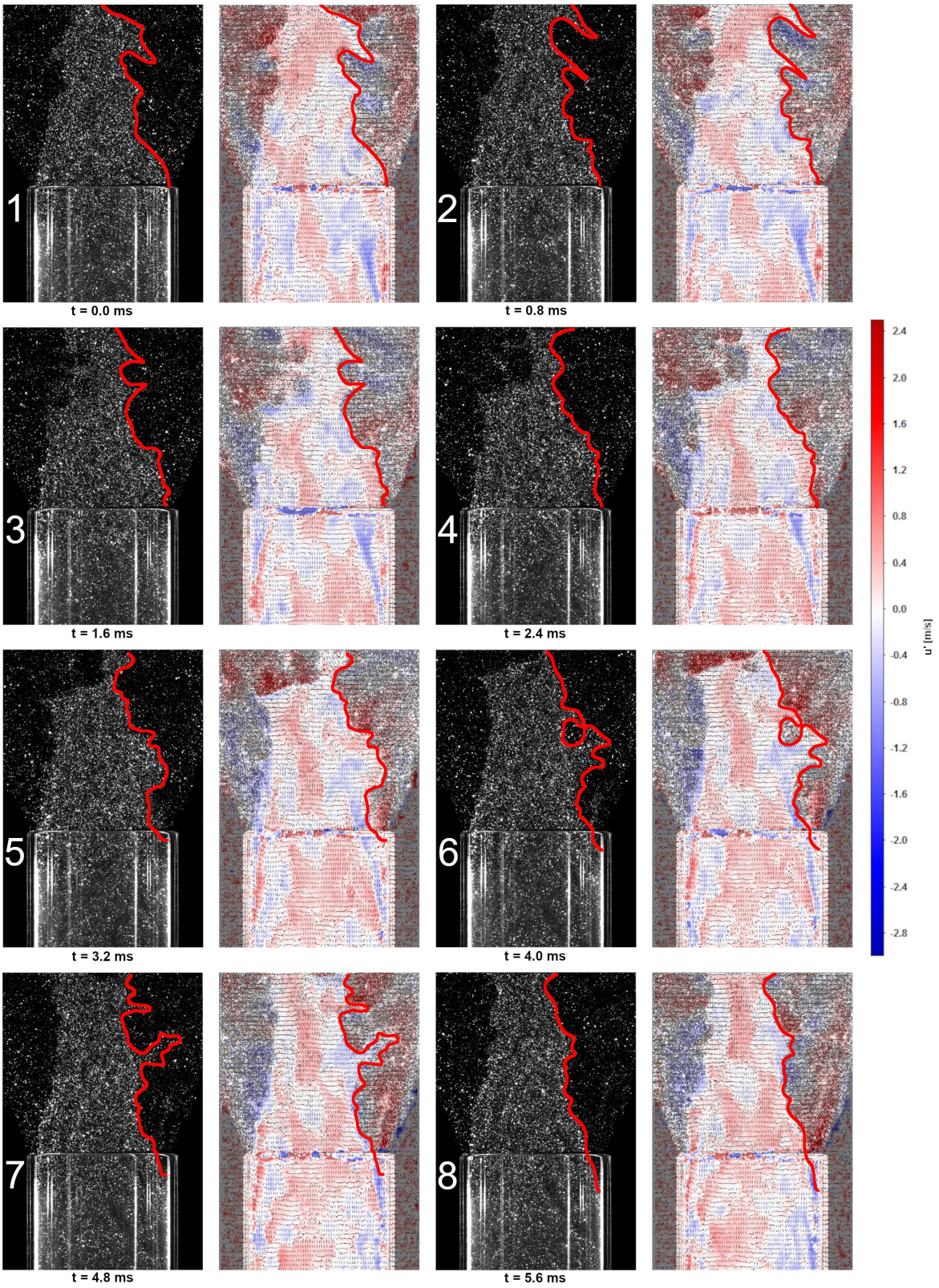

Figure 5.12: Visualisation of the unconfined flashback process for a lean (ϕ =0.4) 100% hydrogen flame. Flashback starts here on the right-hand side of the burner tube. Eight sequential image pairs are shown, each with a time interval of 0.8 ms. The image pair consists of a Mie-scattering image on the left-hand side and the corresponding axial velocity fluctuations u' on the right-hand side. The flame front is highlighted with a red line.

5.4.2. Confined flashback process

The continued upstream propagation of the natural gas flame and the hydrogen flame is shown in the Figures 5.13 and 5.16, respectively. The image sequence starts with the flame inside the quartz tube. Note that each image pair now consists of a Mie-scattering image with the corresponding the velocity field instead of the velocity fluctuation u' Again, the flame front is marked by the red line. The Al_2O_3 seeding particles are able to survive the flame front, but due to the expansion of gasses the seeding density is much lower in the combustion products downstream of the flame front. For the burned gases downstream of the burner tube still a reasonable PIV correlation value could be found. However, for the inside of the burner tube the combination of the low seeding density and the reflections of the burner tube leads to a poor PIV correlation value for the region downstream of the flame. Therefore, no reliable PIV information downstream of the flame front inside the tube could be found. This poses not much of a problem to the analysis of confined flashback as the main focus will be on the flow in front of the flame.

The upstream propagation of the natural gas flame is shown in Figure 5.13. It can be seen that the flame tip is propagating upstream in the vicinity of the wall. The reason for this is the low mixture velocity close to the wall due to the no-slip condition, see the mean velocity profile in Figure 5.1a.
In the previous section about unconfined flashback the experiments already showed that an convex shape of the flame front into the reactants leads to a retardation of the flow in front of the flame. This effect plays a major role for the flame propagating inside the tube as the flame takes a convex shape into the reactants when propagating upstream. It can be seen in the PIV images of Figure 5.13 that the incoming mixture flow decelerated in axial direction, which is not observed for a flame anchored at the burner rim. It seems that the flame has a stronger interaction with the flow when it is inside the tube. In fact, a close-up of the flow in front of the flame in Figure 5.14 shows that the interaction between the flame and the flow is such that a backflow region is formed in front of the flame tip. It was observed in the Mie-scattering images that the backflow region starts to develop between image 2 and 3 in Figure 5.13, which is approximately 5 mm inside the tube. This denotes the start of confined flashback. However, no clear PIV data could be obtained at that particular location due to laser light reflections of the quartz. Therefore, the close-up in Figure 5.14 is taken between image 4 and 5. As can be seen, the backflow extends to approximately 8 mm upstream of the flame tip. This phenomenon is also observed in experiments performed in a channel burner [27], and in swirls burners with a bluff center body [24, 36]. Due to the backflow region, the flame is able to propagate upstream and shows why a confined flame has a much higher flashback propensity compared to an unconfined flame.

A physical mechanism that leads from unconfined flashback to confined flashback can be found in the confinement of the exhaust gases of the flame, as discussed in Section 3.2.2. When the convex flame bulge propagates into the burner, the burned gases at the leading tip of the bulge are blocked by the tube wall. As a consequence, the cross-sectional area of the flow is reduced, leading to higher burned gas velocities. This can clearly be seen when comparing the velocity of the burned gases downstream of the burner rim in image 1 and 2 of Figure 5.13. The ratio in absolute burned gas velocity downstream of the burner rim before and after flashback is approximately 3.6. It is expected that the higher acceleration of the burned gases leads to an increased backpressure at the leading tip of the bulge.

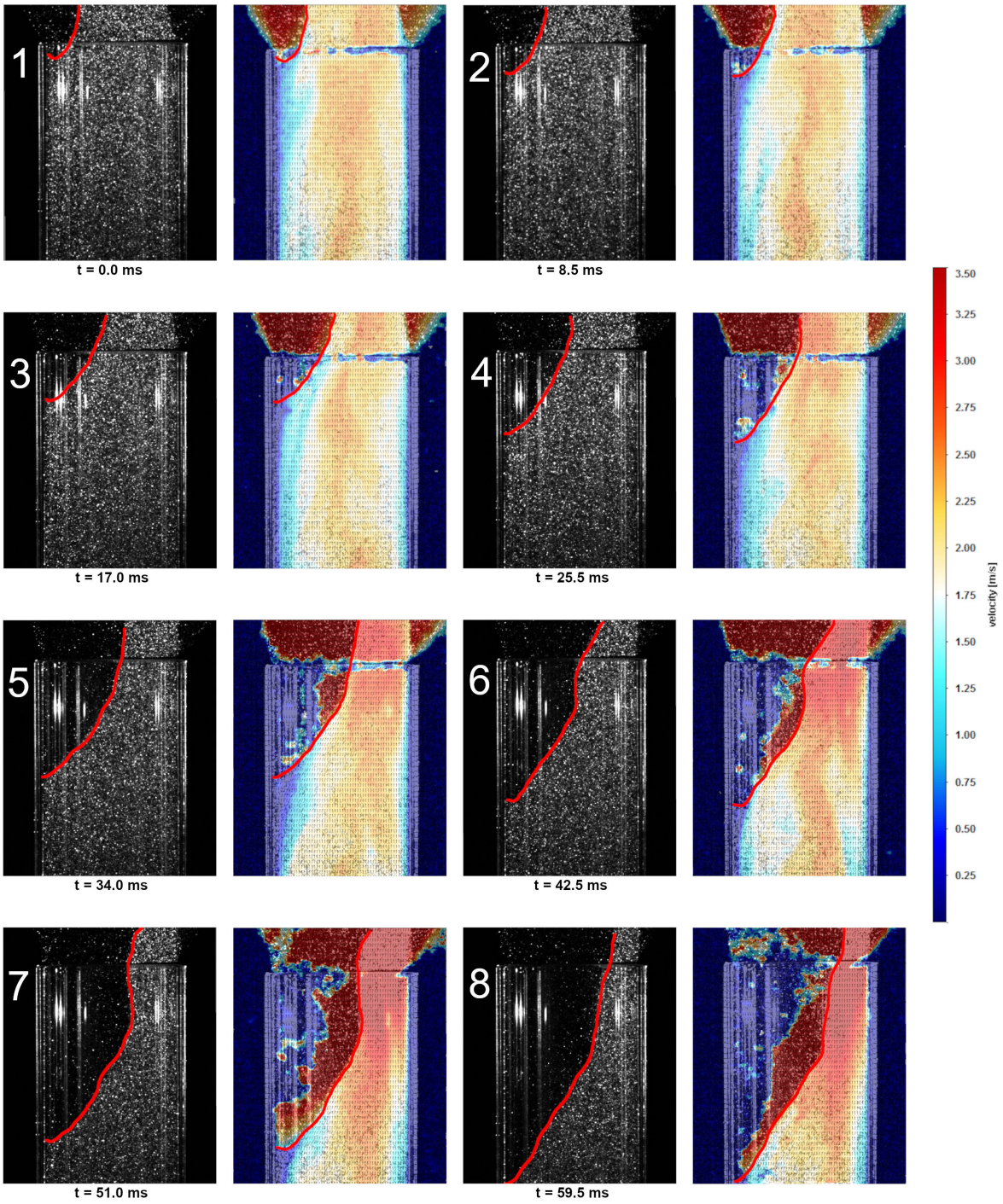

Figure 5.13: Visualisation of the confined flashback process for a stoichiometric ($\phi = 1$) 100% natural gas flame. Flashback occurs here on the left-hand side of the burner tube. Eight sequential image pairs are shown, each with a time interval of 8.5 ms. The image pair consists of a Mie-scattering image on the left-hand side and the corresponding velocity field on the right-hand side. The flame front is marked with a red line.

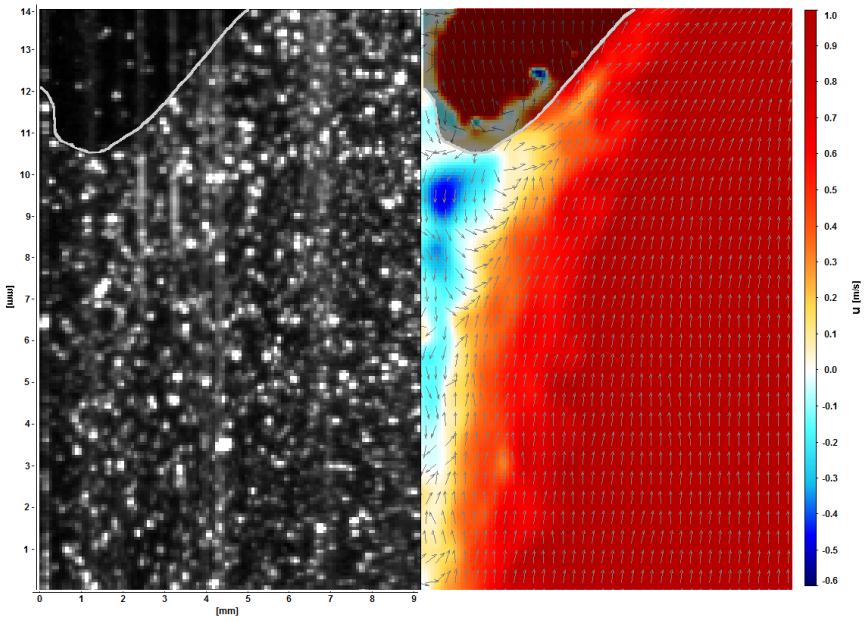

Figure 5.14: Close-up of the confined flashback process showing the interaction between the flame tip and the incoming fresh mixture for the flame inside burner tube. The figure consists of a Mie-scattering image on the left-hand side and the corresponding axial velocities on the right-hand side. The left side of the Mie-scattering image denotes the tube wall. The blue colors denote a negative axial velocity, which show the backflow region formed in front of the flame tip.

Since the stoichiometric natural gas flame is in the wrinkled flamelet regime, see Figure 5.4, it is expected that the hydrodynamic instability plays a significant role in the increased flow flame interaction leading to confined flashback. This is further elaborated in section 5.4.4. The convex shape of the flame inside the tube leads to a significant retardation of the flow at the front of the flame, as described in Section 2.4.1. Note the similarities in streamlines before the convex bulge in Figure 2.9 and Figure 5.14. Since the flame is moving in the low velocity region close to the tube wall, it is presumed that the combined effect of the increased acceleration of the burned gases and the hydrodynamic instability leads to the backflow region in front of the leading tip of the flame.

In the images 4-8 of Figure 5.13, it is observed that the unburned mixture velocity at the right-hand side in the burner tube increases as the flame is propagating further into the burner. This can be explained by the curvature of the streamlines, see Figure 5.15. Figure 5.14 shows that the adverse pressure gradient in front of the flame tip causes the streamlines to be directed from to the right. So, the unburned mixture is directed towards the right-hand side of the burner tube wall. Eventually the streamlines have to be parallel to the opposite wall, leading to opposite curvature of the streamlines. Since a positive pressure gradient points outwards of the center of curvature, the flow on the right-hand side is accelerated. Therefore, the flame is not able to simultaneously propagate upstream on the right-hand side of the burner.

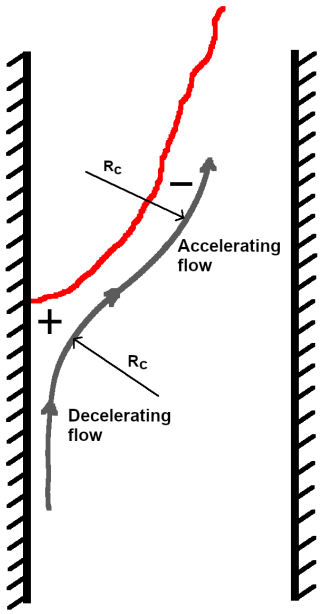

Figure 5.15: Schematic representation of the streamline curvature during confined flame flashback. The flame front is marked by a red line and the radius of curvature is denoted with R_c. The high positive pressure gradient denoted by the (+) in front of the flame decelerates the flow and curves the streamlines to the right. Eventually the streamlines have to be parallel to the opposite wall, leading to opposite curvature of the streamlines accompanied a negative pressure gradient (-), which accelerates the flow.

The confined flashback process of the lean hydrogen shown in Figure 5.16 looks similar to that of the natural gas flame. Image 1-3 show a convex flame bulge propagating upstream along the wall with a reduced flow velocity in front of the flame tip. However, some differences between the hydrogen flame and the natural gas flame are noted. The hydrogen flame propagates much faster upstream into the burner, which will be further elaborated in Section 5.4.3. Also, the hydrogen flame propagates much closer to wall than the natural gas flame. A reason for this phenomenon is that the quenching distance of a hydrogen flame is very low compared to a natural gas flame [58]. This means that the hydrogen flame is able to sustain itself closer to the wall and can therefore propagate upstream very close to the wall. As a result, the cross-sectional flow area of the burned gases is more reduced than for the natural gas flame leading to higher acceleration of the burned gas. The ratio in absolute burned gas velocity downstream of the burner rim before and after flashback of the hydrogen flame is 4.5, which is indeed higher than for the natural gas flame. It is expected that this results in a higher backpressure on the flow at the flame tip. Since the hydrogen flame propagates close to the burner wall, it was very difficult to obtain a clear detailed image of the interaction between the leading tip of the hydrogen flame and the flow due to the laser light reflections. Also, the flame tip of the hydrogen flame is likely to move in and out of the focal PIV plane, which will be mentioned in Section 5.4.3. Still, from the close-up setup described in Section 4.3 a small backflow region in front of the flame tip was observed in the Mie-scattering images, which is also observed by Eichler [27].

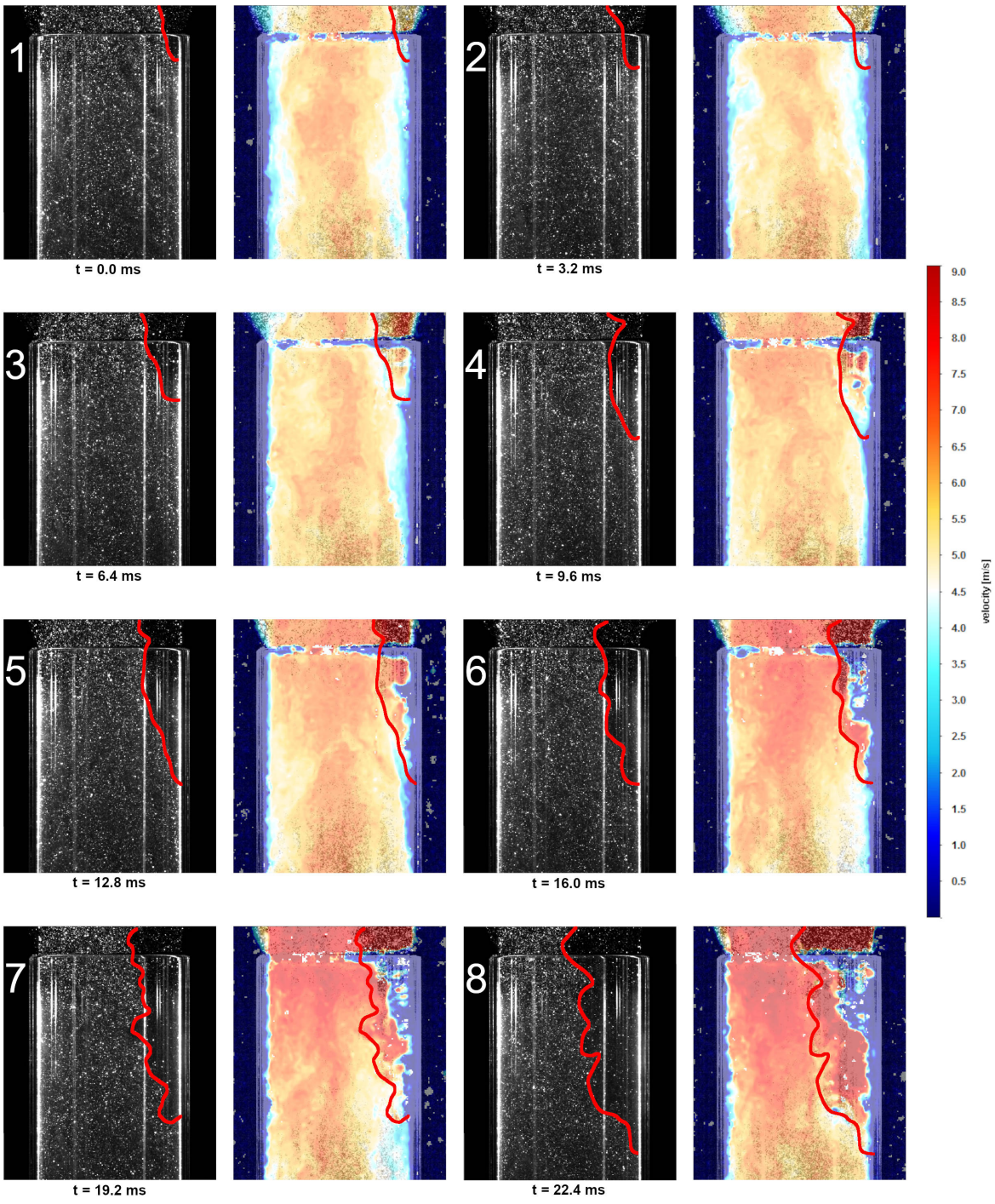

Figure 5.16: Visualisation of the confined flashback process for a lean (ϕ =0.4) 100% hydrogen flame. Flashback occurs here on the right-hand side of the burner tube. Eight sequential image pairs are shown, each with a time interval of 2 ms. The image pair consists of a Mie-scattering image on the left-hand side and the corresponding velocity field on the right-hand side. The flame front is marked with a red line.

5.4.3. Upstream propagation velocity

Figure 5.17 shows the position of the flame tip propagating inside the quartz tube as a function of time and the corresponding upstream propagation velocity as determined via the Mie-scattering images for both the natural gas flame and the hydrogen flame. The data sampling is done manually because of the difficulty to determine the flame front inside the tube, especially in the case of the hydrogen flame. The time for both the natural gas flame and the hydrogen flame to reach 40 mm inside the tube was different for each measurement. Therefore, multiple flashback measurements are taken to obtain an average propagation velocity of the flames, which are shown by the bold red and blue lines in Figure 5.17b. Figure 5.17a shows the position of the flame tip inside the burner tube as a function of time. At x = 0, t = 0, the flame tip is located at the burner rim.

Figure 5.17a shows that, in some flashback events, the flame tip of the natural gas flame (0% H_2) propagates steadily upstream into the burner tube. However, there are also cases where the flame tip moves upstream and downstream in an irregular way. Since the unburned mixture flow is turbulent, it consists of positive and negative velocity fluctuations. Some positive velocity fluctuations are able to overcome the adverse pressure gradient induced by the flame and push the flame in the downstream direction, which is denoted as a negative upstream propagation velocity in Figure 5.17b. On the other hand, the negative velocity fluctuations increase the upstream propagation velocity of the flame.

In the 100% hydrogen case the irregular movements of the flame tip are much stronger and occur more frequently, see Figure 5.17b. The reason for this can be found in the higher Reynolds number at flashback than the natural gas flame. A natural gas flame with ϕ = 1 flashes back at Re $\approx$ 2800, which is close to laminar flow. For comparison, a hydrogen flame with ϕ = 0.4 already flashes back at Re $\approx$ 8000. At Re $\approx$ 8000, the velocity fluctuations u' are higher than at Re $\approx$ 2800. Also, the timescale of the smallest turbulent eddies is smaller in a flow characterized by a higher Reynolds, meaning a higher frequency of the velocity fluctuations.

Another reason for the very high peaks in the upstream propagation velocity for the hydrogen case is the three dimensional nature of flashback. As Eichler [27] and Ebi et al. [24] observed, it is not only one flame bulge that propagates upstream into the burner. Also, the flame tip of the lean hydrogen flame has a much higher tendency to widen and to break up into smaller bulges than the natural gas flame [27]. This poses a problem for the measurement of the upstream propagation of the flame tip. Since a 2D-measurement technique is used, it is likely that the actual flame tip moves in and out of the

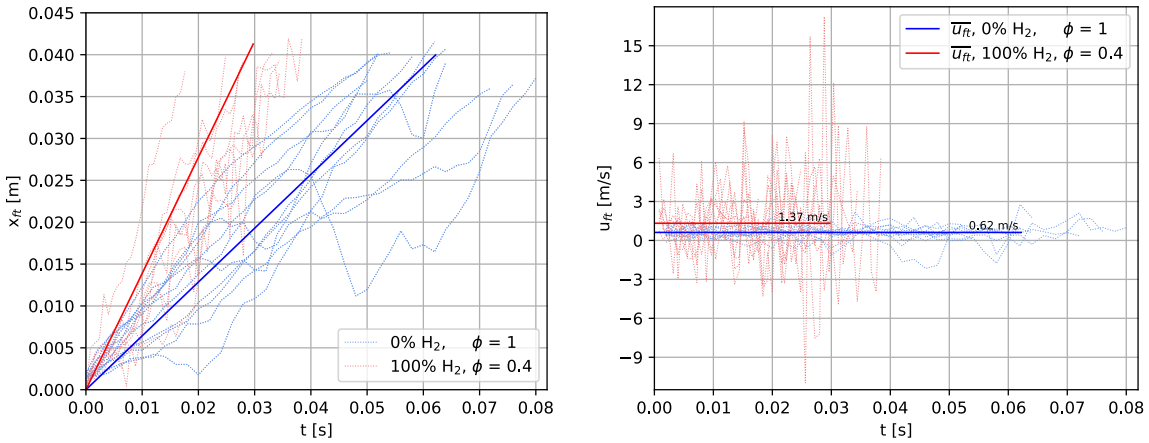

(a) Position of the flame tip x_{ft} propagating inside the quartz tube as a function of time. At x = 0, t = 0, the flame tip is at the burner rim.

(b) Upstream propagation velocity of the flame tip u_{ft} inside the quartz tube as a function of time. At t = 0, the flame tip is at the burner rim.

Figure 5.17: **(a)** Position of the flame tip propagating upstream inside the quartz tube as a function of time. At x = 0, t = 0, the flame tip is at the burner rim. **(b)** Upstream propagation velocity of the flame tip inside the quartz tube as a function of time. At t = 0, the flame tip is at the burner rim. Two mixtures of pure natural gas (0% H_2) and hydrogen (100% H_2) are used with ϕ=1 and ϕ=0.4, respectively. The bold lines denote the mean upstream propagation velocity. The length of these lines show the average time needed to propagate 40 mm inside the tube.

focal PIV plane. As a consequence, certain jumps in flame tip location were observed which lead to a very high velocity peaks. therefore, it is more appropriate to focus on the average upstream propagation velocity of the flame.

In Figure 5.17b it can be seen that the mean upstream propagation velocity of the stiochiometric (ϕ = 1) natural gas flame and the lean (ϕ = 0.4) hydrogen flame is 0.62 m/s and 1.37 m/s, respectively. Interestingly, similar upstream propagation velocities of these flames are reported in different types of burners. Ebi et al. [23], who studied confined boundary layer flashback in a swirl burner with a bluff body, reported that the leading edge of a stiochiometric (ϕ = 1) natural gas flame propagates with a mean velocity of 0.6 m/s. Eichler [27] mentioned that during confined boundary layer flashback in a channel burner, the mean upstream bulge velocity of a slightly leaner (ϕ = 0.36) hydrogen flame was 1.37 m/s. However, more experimental data is needed to conclude that these mean upstream propagation velocities are characteristic for these two flames.

The ratio of the mean upstream propagation velocity and the unstretched laminar flame speed ($\overline{u_{ft}}/s_{l,0}$ = 0.62/0.36) = 2 for natural gas and ($\overline{u_{ft}}/s_{l,0}$ = 1.37/0.19) = 7.2 for hydrogen. That these ratios are larger than unity is expected, since the flame is highly curved during confined flashback and $s_{l,0}$ is based on an one-dimensional flat flame. However, the ratio for the hydrogen flame is much higher than for the natural gas flame. This can be due to several reasons. As mentioned in section 5.4.2, when the flame tip is located inside the tube, the burned gases of the hydrogen flame are more accelerated than the natural gas flame, which is expected to induce a higher backpressure on the flow in front of the flame tip. Another reason can be found in the different flame instabilities encountered in the natural gas flame and the hydrogen flame. Figure 5.18 shows the interaction of the natural gas flame with a low velocity region in the unburned mixture. It can be seen that a convex bulge is formed towards the reactants as a result of the sudden low mixture velocity. As a result, the flow velocity in front of the convex bulge is retarded and the bulge starts to grow, which is a clear example of the hydrodynamic instability. The Markstein number is positive for a stoichiometric natural gas flame, so no thermal-diffusive instabilities are expected. This is not true for the lean hydrogen flame, where the Markstein number is negative and thus the effects of thermal-diffusive instabilities are expected. The flame regime map in Section 5.2.1 indicates that the hydrogen flame is operating in the thin reaction regime, close to the corrugated flamelet regime. According to Chaudhuri et al. [20] and Chomiak et al. [49] no hydrodynamic instabilities can be expected there. This can be seen in Figure 5.19. Again, convex bulges towards the reactants are formed to small low velocity regions in the unburned mixture. However, in contrast with the natural gas flame, the flow velocity is not retarded in front of the convex flame bulges. Still, the bulges grow as they are advected by the bulk flow, which shows the effect of the thermal-diffusive instability. The effect of the hydrodynamic instability on the flame speed due to additional flame wrinkling becomes only evident at large $\ell_0/\delta_f > 10^2$ [20], so the flame speed of the natural gas flame is not

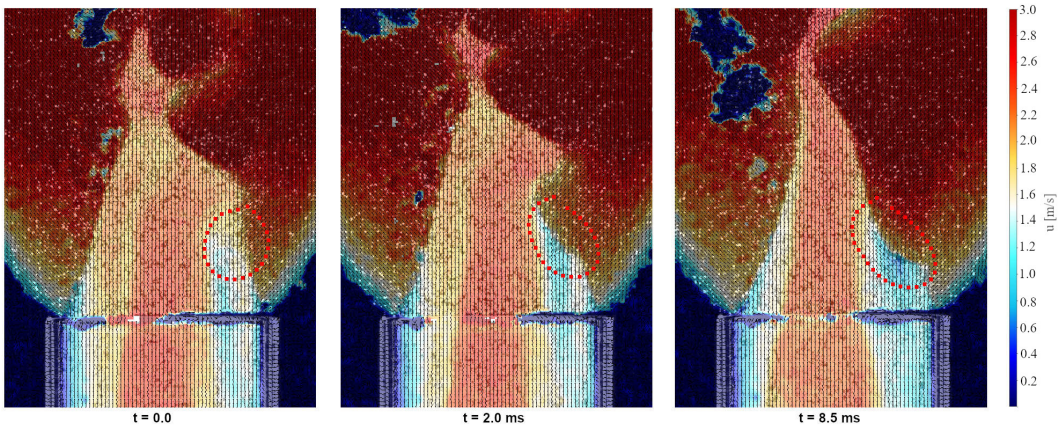

Figure 5.18: Interaction of a low velocity region with the stoichiometric (ϕ = 1) natural gas flame, leading to the hydrodynamic instability. The convex bulge towards the reactants is marked by the red dashed line.

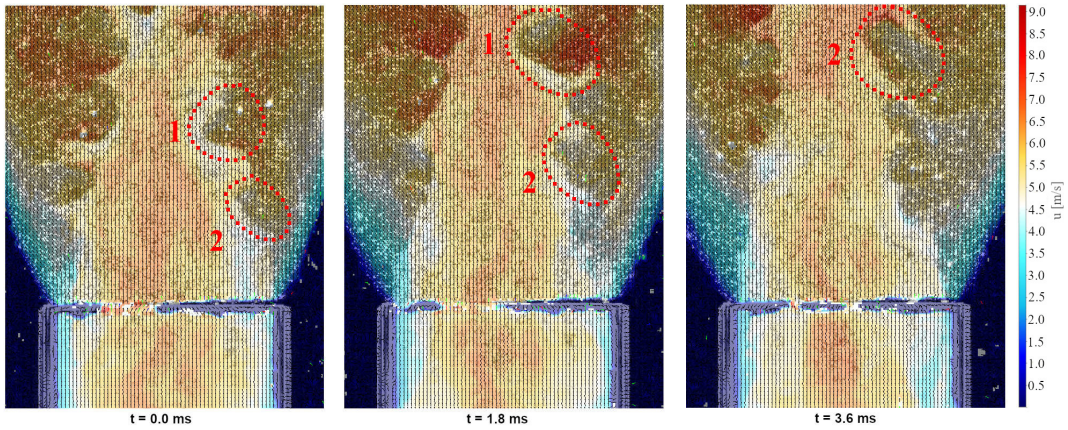

Figure 5.19: Convex bulges in the lean (ϕ = 0.4) initiated by low velocity regions in the flow. The growth of the bulges without flow retardation shows the thermal-diffusive instability. The convex bulges towards the reactants is marked by the red dashed line.

affected by the hydrodynamic instability. On the other hand, the thermal-diffusive instability has a large effect on the flame speed of the lean hydrogen flame even at high turbulent intensity [48] and given that the leading flame tip is convex to the reactants during confined flashback as shown in Section 5.4.2, this will strongly increase the local flame speed. As a result, the upstream propagation velocity of the flame will increase.

5.4.4. Discussion on the flashback process

The unconfined flashback process as described in Section 3.2.3 shows that regions with negative velocity fluctuations in the unburned mixture are the predominant physical mechanism for the start of a flashback event and for the transient flashback process of the flame propagating into the burner. However, it is important to note that flashback is not occurring for every region with negative velocity fluctuations. The experiments showed that the start of a flashback event depends on the combination of several parameters: the bulk velocity, the position of the flame front before it interacts with a region with negative velocity fluctuations, the magnitude of the negative velocity fluctuations and whether a region with positive velocity fluctuations is absent after interaction of the flame with the region consisting of negative fluctuations. So, unconfined flashback is rather a statistical phenomena, where the chance of the occurrence of a flashback event is increasing for a decreasing bulk flow velocity. This explains why there is a certain scatter in the bulk velocity at flashback in Figure 5.2.

After initiation of unconfined flashback, the flame starts to propagate upstream past the burner rim along wall of the burner tube. As mentioned in Section 5.4.2, after a distance of approximately 5 mm upstream of the burner rim, a backflow region starts to develop in front of the flame. The flashback mechanism is then referred to as confined flashback. The time needed for a natural gas flame propagating upstream from the burner rim to reach a confined configuration is approximately 17 ms. So, the transient process between unconfined and confined flame flashback is very short and fast. It is suggested that the convex shape of the flame front towards the reactants, the reduced cross-sectional flow area of the burned gases strongly enhances the flame flow interaction, leading from unconfined flashback to confined flashback. The created backflow in front of the flame and the above-mentioned mechanisms strongly enhance the upstream flame propagation, which explains why the flashback propensity for confined flames is much higher than for unconfined flames. A leakage flow that would reduce the flashback propensity of unconfined flames, mentioned in Section 3.2.2, is not found.

For the flashback process, it is important to know the diffusion characteristics of the unburned mixture and the flame regime in which the flame is operating. This will give an indication which flame instabilities can be encountered and how much influence the turbulent flow has on the laminar flame speed. So in other words, it gives information about the flame flow interaction. The hydrodynamic instability is relevant in the stoichiometric natural gas flame, where the thermal-diffusive instability plays an important role in the lean hydrogen flame.

6

Conclusion

The flashback phenomena of turbulent hydrogen-natural gas-air flames have been investigated experimentally in a quartz Bunsen burner using Particle Image Velocimetry (PIV). Experiments were conducted to gain insight into the physical mechanisms that play a role in the transition from unconfined to confined flame flashback. The answers to the research questions formulated in Section 1.3 are presented in the conclusions of the experiments that can be divided into three groups:

- Flashback maps: The flashback maps are obtained to determine the flashback limits of the quartz Bunsen burner in terms of the bulk velocity and the Reynolds number at flashback as a function of the equivalence ratio. The flashback limits of six different fuel mixtures were investigated ranging from pure natural gas (0% H_2) to pure hydrogen (100% H_2) to gain insight into the effects of hydrogen addition in the fuel.
- Influence of the flame on the flow characteristics: The first objective was to determine whether the stable unconfined flame affects the mean velocity profile in the tube. Thereby, it is investigated whether the fuel composition plays a role. The mean velocity profiles are measured in the presence of the flame. These mean velocity profiles are compared to the velocity profiles of the cold flow. The second objective was to determine whether the transition of a stable flame to an unstable flame close to flashback has an effect on the mean velocity profile inside the burner tube. The influence of the flame on the Reynolds stresses is also considered here.
- Instantaneous flashback process: The transient flashback process from unconfined to confined is captured for a stoichiometric (ϕ = 1) natural gas flame and a lean (ϕ = 0.4) hydrogen flame. The upstream propagation velocity of both flames is determined and analysed.

Conclusions
The following conclusions can be made regarding the flashback maps:

- Hydrogen addition in the fuel leads to a significantly higher flashback propensity.
  Every 20% hydrogen addition in the fuel results in a nonlinear increase in the bulk velocity at flashback.
- The ratio between the bulk velocity at flashback and the unstretched laminar flame speed ($U_b/s_{l,0}$) is not the same for the six different fuel mixtures, Especially at low equivalence ratios, the ratio $U_b/s_{l,0}$ becomes very large for the fuels with a high hydrogen content. This is attributed to thermal-diffusive instability of the lean hydrogen flame. Also at very low equivalence ratios (ϕ = 0.4, ϕ = 0.5) the flames with 80% hydrogen or higher indicate to operate in the thin reaction regime, where turbulence has an effect on the transport in the preheat zone, which enhances the turbulent flame speed.

The following conclusions can be made about the influence of the flame on the flow characteristics:

- The backpressure of a stable unconfined natural gas/hydrogen flame has no influence on the mean velocity profile at a distance of $0.12d_i$ upstream of the burner rim. This also holds for a hydrogen flame close to flashback conditions.

- The main difference between a stable flame and a flame close to flashback can be seen in the Reynolds stresses outside the tube. Both regions with high normalized Reynolds stresses in axial direction ($\overline{u'u'}/U_b^2$) and in radial direction ($\overline{v'v'}/U_b^2$) increase in magnitude and are spread over a larger area when the stable unconfined flame is brought to flashback conditions. This is due to the following reasons:
  - As the Reynolds number decreases, intrinsic flame instabilities like the thermal-diffusive instability have more time to develop before they are advected by the bulk flow. As a result, the flame becomes more wobbly and the location of the frame front will be spread over a larger area. Consequently, the high normalized Reynolds stresses are spread over a larger area.
  - As the Reynolds number decreases, the average flame cone angle increases. This leads to a higher acceleration across the flame front in both the axial and radial direction for an average flame angle between 0°and 45°. Consequently, the normalized Reynolds stresses increase in magnitude.

The following conclusions can be made after capturing the transient flashback process of a stoichiometric natural gas flame and a lean hydrogen flame:

- Regions with negative velocity fluctuations in the unburned mixture are the predominant physical mechanism for the start of unconfined flashback and for the transient flashback process of the flame propagating into the burner. However, the start of a flashback event depends on the combination of several parameters: the bulk velocity, the position of the flame front before it interacts with a region with negative velocity fluctuations, the magnitude of the negative velocity fluctuations and whether a region with positive velocity fluctuations is absent after interaction of the flame with the region consisting of negative fluctuations. So, unconfined flashback is rather a statistical phenomena, where the chance of the occurrence of a flashback event is increasing for a decreasing bulk flow velocity.
- The transient process between unconfined and confined flashback is very short and fast. After a distance of approximately 5 mm upstream of the burner rim, a backflow region starts to develop in front of the flame, which denotes the start of confined flashback. The time needed for a natural gas flame propagating upstream from the burner rim to reach a confined configuration is approximately 17 ms and only 5.6 ms for the hydrogen flame.
- The suggested physical mechanisms leading from unconfined flashback to confined flashback are: the convex shape of the flame towards the reactants during upstream flame propagation and the reduced cross-sectional flow area of the burned gases at the flame tip. Due to the created backflow in front of the flame and the above-mentioned mechanisms, the upstream flame propagation is strongly enhanced, leading to a higher flashback propensity for confined flames than for unconfined flames.
- The ratio between the mean upstream propagation velocity and the laminar flame speed ($u_{ft}/s_{l,0}$) is much higher for the hydrogen flame than for the natural gas flame. It is suggested that this is due to two reasons:
  - The hydrogen flame propagates closer to the wall, leading to a smaller cross-sectional flow area for the burned gases at the flame tip. This results in a higher acceleration of the burned gases and thus in a higher backpressure at the flame tip.
  - The hydrogen flame is thermal-diffusive unstable and the convex shape of the flame tip during flashback strongly enhances the local flame speed and thus the upstream propagation velocity. In contrast, the hydrodynamic instability encountered in the natural gas flame only retards the flow in front of the flame tip, but does not affect the flame speed.

Recommendations and further developments

- Since flashback is a three-dimensional phenomenon, it is recommended to use tomographic PIV to gain more insight into the interaction of an unconfined flame with velocity fluctuations. This also holds for the interaction of a confined flame with the boundary layer.

- To learn more about the backpressure effect of a reduced cross-sectional flow area of the burned gases, quartz tubes of larger inner diameters could be placed on top of the existing quartz tube.
- Future research could be performed on tube burners with rough surfaces to manipulate the velocity fluctuations close to the wall.
- High temperatures and pressures are present in a gas turbine. The effects of elevated preheat temperatures and pressures on the flashback mechanism could be the subject of future experimental research.

A

Labview Control panel

The Labview control panel is designed by Luuk Altenburg. This chapter gives an overview of the used constants and formulas.

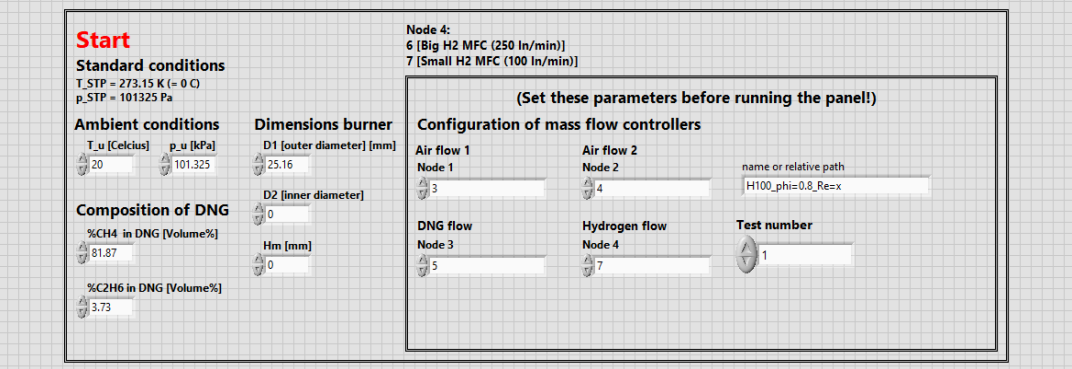

(a) Panel to provide the initial conditions conditions before starting an experiment.

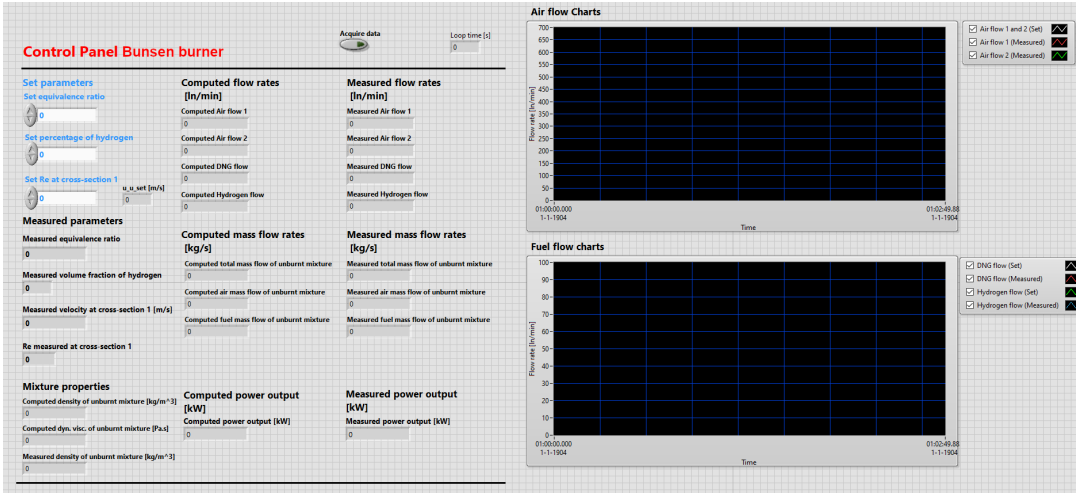

(b) In this panel the equivalence ratio ϕ, the volume percentage of hydrogen in the fuel and the Reynolds number can be filled in to obtain the required mixture. All the measured values by the mass flow controllers are checked by computed values in order to know whether the mass flow controllers have converged to the right mass flow.

Figure A.1: Labview Frontpanel

A.1. Labview frontpanel
A.2. Labview backpanel: Governing Equations

Molar masses and molar volume

$M_H = 1.008\ \frac{g}{mol};\quad M_{H2} = 2M_H;\quad M_C = 12.011\ \frac{g}{mol};\quad M_N = 14.007\ \frac{g}{mol};\quad M_{N2} = 2M_N;$

$M_O = 15.999\ \frac{g}{mol};\quad M_{O2} = 2M_O;\quad M_{Ar} = 39.948\ \frac{g}{mol}$

$R_{gas} = 8.314\ \frac{Pam^3}{molK};\quad V_m = \frac{R_{gas}T}{p}$

Density of species

$\rho_{H2} = \frac{2M_H}{V_m};\quad \rho_{CH4} = \frac{M_C + 4M_H}{V_m}$

$\rho_{C2H6} = \frac{2M_C + 6M_H}{V_m};\quad \rho_a = \frac{f_{N2/air}M_{N2} + f_{O2/air}M_{O2} + f_{Ar/air}M_{Ar}}{V_m}$

Composition of air

Volume fractions:

$f_{N2/air} = 0.78;\quad f_{O2/air} = 0.21;\quad f_{Ar/air} = 0.01$

Number of moles of air normalized for 1 mol of O_2:

$n_a = \frac{f_{N2/air}}{f_{O2/air}} + \frac{f_{O2/air}}{f_{O2/air}} + \frac{f_{Ar/air}}{f_{O2/air}} = \frac{f_{N2/air}}{f_{O2/air}} + 1 + \frac{f_{Ar/air}}{f_{O2/air}} (= 4.76)$

$n_a \mathrm{AIR} = \frac{f_{N2/air}}{f_{O2/air}} \mathrm{N_2} + 1\ \mathrm{O_2} + \frac{f_{Ar/air}}{f_{O2/air}} \mathrm{Ar}$

Composition of fuel

$x_{DNG} + x_{H2} = 1;\quad x_{CH4} + x_{C2H6} + x_{N2} = 1$

$x_{CH4} = 0.8187;\quad x_{C2H6} = 0.0373;\quad x_{N2} = 1 - (x_{CH4} + x_{C2H6})$

Chemical reactions

Combustion of hydrogen:

$$x_{H2}\left[\mathrm{H_2} + \frac{1}{2} n_a \mathrm{AIR} \rightarrow \mathrm{H_2O} + \frac{1}{2}\left(\frac{f_{N2/air}}{f_{O2/air}}\mathrm{N_2} + \frac{f_{Ar/air}}{f_{O2/air}}\mathrm{Ar}\right)\right]$$

Combustion of methane:

$$x_{DNG}\left[x_{CH4}\left[\mathrm{CH_4} + 2n_a \mathrm{AIR} \rightarrow \mathrm{CO_2} + 2\mathrm{H_2O} + 2\left(\frac{f_{N2/air}}{f_{O2/air}}\mathrm{N_2} + \frac{f_{Ar/air}}{f_{O2/air}}\mathrm{Ar}\right)\right]\right]$$

Combustion of ethane:

$$x_{DNG}\left[x_{C2H6}\left[\mathrm{C_2H_6} + \frac{7}{2} n_a \mathrm{AIR} \rightarrow 2\mathrm{CO_2} + 3\mathrm{H_2O} + \frac{7}{2}\left(\frac{f_{N2/air}}{f_{O2/air}}\mathrm{N_2} + \frac{f_{Ar/air}}{f_{O2/air}}\mathrm{Ar}\right)\right]\right]$$

Correction for Standard Temperature and Pressure (STP)

$T_{stp} = 273.15\ K; \quad p_{stp} = 101325\ Pa$

Ideal Gas Law:

$$pV = nRT \xrightarrow{n=1} pV = RT \xrightarrow{V=Q\cdot t} pQt = RT$$

Unburnt conditions:

$$\frac{p_u Q_X}{RT_u} = \frac{p_{stp} Q_{X,stp}}{RT_{stp}} \rightarrow Q_X = Q_{X,stp} \cdot \underbrace{\frac{T_u}{T_{stp}} \cdot \frac{p_{stp}}{p_u}}_{STP}$$

$$\phi = \frac{\dot{m}_f/\dot{m}_a}{(\dot{m}_f/\dot{m}_a)_{stoich}} = \frac{Q_f/Q_a}{(Q_f/Q_a)_{stoich}} = \frac{n_f/n_a}{(n_f/n_a)_{stoich}}$$

$$\left.\begin{matrix}(n_f/n_a)_{stoich} \\ n_{f,stoich} = 1\end{matrix}\right\} (n_f/n_a)_{stoich} = \frac{1}{n_a\left(\frac{1}{2}x_{H2} + x_{DNG}\cdot(2x_{CH4} + \frac{7}{2}x_{C2H6})\right)}$$

Flow rates and velocity

$Q_u = Q_a + Q_f; \quad Q_u = Au_u$

$$Q_f = \frac{u_u A}{1 + \frac{1}{\phi(n_f/n_a)_{stoich}}}; \quad Q_a = \frac{u_u A}{1 + \phi(n_f/n_a)_{stoich}}$$

$\dot{m}_u = \dot{m}_a + \dot{m}_f; \quad \dot{m}_u = \rho_u * Q_u$

$\dot{m}_f = \rho_f Q_f; \quad \dot{m}_a = \rho_a Q_a$

$$\rho_u = \frac{\rho_f Q_f + \rho_a Q_a}{Q_u}$$

$$\rho_f = \rho_{H2} x_{H2} + \rho_{CH4} x_{DNG} x_{CH4} + \rho_{C2H6} x_{DNG} x_{C2H6}$$

Wilke's method [71] for dynamic viscosity of the mixture (extension in current labview panel):

$$\mu_u = \sum_{j=1}^{n} \frac{\mu_i}{1 + \frac{1}{x_i} \sum_{\substack{j=1 \\ j \neq i}}^{j=n} x_j \phi_{ij}}; \quad \phi_{ij} = \frac{\left(1 + \left(\frac{\mu_i}{\mu_j}\right)^{\frac{1}{2}} \left(\frac{M_j}{M_i}\right)^{\frac{1}{4}}\right)^2}{\left(\frac{4}{\sqrt{2}}\right)\left(1 + \left(\frac{M_i}{M_j}\right)\right)^{\frac{1}{2}}}$$

$$Re = \frac{\rho_u u_u D_i}{\mu_u}$$

Power output

Lower heating values:

$$LHV_{H2} = 120\ MJ/kg; \quad LHV_{CH4} = 50\ MJ/kg; \quad LHV_{C2H6} = 50\ MJ/kg$$

$$P_{thermal} = Q_f(\rho_{H2} x_{H2} LHV_{H2} + \rho_{CH4} x_{DNG} x_{CH4} LHV_{CH4} + \rho_{C2H6} x_{DNG} x_{C2H6} LHV_{C2H6})$$

Bibliography

[1] Bronkhorst :EL-FLOW® Select Digital Thermal Mass Flow Meters and Controllers for Gases. URL https://www.bronkhorst.com/getmedia/98668a82-8d1c-4b7f-af8e-995be25641b3/EL-FLOW-Select_en.pdf.

[2]

[3] EIA: How much carbon dioxide is produced when different fuels are burned? URL https://www.eia.gov/tools/faqs/faq.php?id=73&t=11.

[4] Eurostat: Renewable energy statistics. URL https://ec.europa.eu/eurostat/statistics-explained/index.php/Renewable_energy_statistics#Share_of_renewable_energy_more_than_doubled_between_2004_and_2019.

[5] EU Climate strategies & targets: 2050 long-term strategy. URL ec.europa.eu/clima/policies/strategies/2050en.

[6] IEA: Data and Statistics. URL https://www.iea.org/data-and-statistics?country=WORLD&fuel=Energy%20supply&indicator=TPESbySource.

[7] Kawasaki: Gas Turbine Technology, DLE Combustion Method. URL https://global.kawasaki.com/en/energy/equipment/gas_turbines/technology/index.html.

[8] CE Delft: Verkenning ontwikkeling CO_2-vrije flexibele energietechnieken, 2020. publication number: 20.190402.041.

[9] J. Andersson and S. Grönkvist. Large-scale storage of hydrogen. *International Journal of Hydrogen Energy*, 44(23):11901–11919, 2019. ISSN 0360-3199. doi: https://doi.org/10.1016/j.ijhydene.2019.03.063. URL https://www.sciencedirect.com/science/article/pii/S0360319919310195.

[10] A. J. Aspden, J. B. Bell, M. S. Day, S. E. Woosley, and M. Zingale. Turbulence□flame interactions in type ia supernovae. *The Astrophysical Journal*, 689(2):1173–1185, 2008. ISSN 0004-637X. doi: 10.1086/592726. URL https://dx.doi.org/10.1086/592726.

[11] G. Baumgartner. *Flame flashback in premixed hydrogen-air combustion systems*. Verlag Dr. Hut, 2014. ISBN 3843920753.

[12] G. Baumgartner, L. R. Boeck, and T. Sattelmayer. Experimental investigation of the transition mechanism from stable flame to flashback in a generic premixed combustion system with high-speed micro-piv and micro-plif combined with chemiluminescence imaging. In *Turbo Expo: Power for Land, Sea, and Air*, volume 56680, page V04AT04A047. American Society of Mechanical Engineers. ISBN 0791856682.

[13] J.K. Bechtold and M. Matalon. The dependence of the markstein length on stoichiometry. *Combustion and flame*, 127(1-2):1906–1913, 2001. ISSN 0010-2180.

[14] A. C. Benim and K.J. Syed. *Concepts Related to Combustion and Flow in Premix Burners*, pages 5–18. 2015. ISBN 9780128007556. doi: 10.1016/b978-0-12-800755-6.00002-7.

[15] A. Cemal Benim and K.J. Syed. *Combustion-Induced Vortex Breakdown–Driven Flashback*, pages 73–102. 2015. ISBN 9780128007556. doi: 10.1016/b978-0-12-800755-6.00009-x.

[16] A.L. Berlad and A.E. Potter. Relation of boundary velocity gradient for flash-back to burning velocity and quenching distance. *Combustion and Flame*, 1(1):127–128, 1957. ISSN 0010-2180. doi: https://doi.org/10.1016/0010-2180(57)90040-8. URL https://www.sciencedirect.com/science/article/pii/0010218057900408.

[17] O.H. Björnsson. Boundary layer flashback prediction for low emissions full hydrogen gas turbine burners using flow simulation. Master thesis, Delft University of Technology, 2019 URL http://resolver.tudelft.nl/uuid:8272a27d-692d-4721-a24c-98ffd4c52511.

[18] E. M. Burke, F. Güthe, and R. F. D. Monaghan. A Comparison of Turbulent Flame Speed Correlations for Hydrocarbon Fuels at Elevated Pressures. Volume 4B: Combustion, Fuels and Emissions, 06 2016. doi: 10.1115/GT2016-57804. URL https://doi.org/10.1115/GT2016-57804. V04BT04A043.

[19] Y.A. Çengel and J.M. Cimbala. *Fluid Mechanics: Fundamentals and Applications*. Fluid Mechanics: Fundamentals and Applications. McGraw-HillHigher Education, 2006. ISBN 9780073044651.

[20] Swetaprovo Chaudhuri, V'Yacheslav Akkerman, and Chung K. Law. Spectral formulation of turbulent flame speed with consideration of hydrodynamic instability. *Physical Review E*, 84(2), 2011. ISSN 1539-3755. doi: 10.1103/physreve.84.026322.

[21] J Driscoll. Turbulent premixed combustion: Flamelet structure and its effect on turbulent burning velocities. *Progress in Energy and Combustion Science*, 34(1):91–134, 2008. ISSN 0360-1285. doi: 10.1016/j.pecs.2007.04.002.

[22] Z. Duan, B. Shaffer, V. McDonell, G. Baumgartner, and T. Sattelmayer. Influence of burner material, tip temperature, and geometrical flame configuration on flashback propensity of h2-air jet flames. *Journal of Engineering for Gas Turbines and Power*, 136(2), 2014. ISSN 0742-4795 1528-8919. doi: 10.1115/1.4025359.

[23] D. Ebi, R. Ranjan, and N.T. Clemens. Coupling between premixed flame propagation and swirl flow during boundary layer flashback. *Experiments in Fluids*, 59(7), 2018. ISSN 0723-4864 1432-1114. doi: 10.1007/s00348-018-2563-7.

[24] Dominik Ebi and Noel T. Clemens. Experimental investigation of upstream flame propagation during boundary layer flashback of swirl flames. *Combustion and Flame*, 168:39–52, 2016. ISSN 0010-2180. doi: https://doi.org/10.1016/j.combustflame.2016.03.027. URL https://www.sciencedirect.com/science/article/pii/S001021801630044X.

[25] C. Eichler and T. Sattelmayer. Premixed flame flashback in wall boundary layers studied by long-distance micro-piv. *Experiments in Fluids*, 52(2):347–360, 2012. ISSN 0723-4864. doi: 10.1007/s00348-011-1226-8. URL https://dx.doi.org/10.1007/s00348-011-1226-8.

[26] C. Eichler, G. Baumgartner, and T. Sattelmayer. Experimental investigation of turbulent boundary layer flashback limits for premixed hydrogen-air flames confined in ducts. *Journal of Engineering for Gas Turbines and Power*, 134(1), 2012. ISSN 0742-4795 1528-8919. doi: 10.1115/1.4004149.

[27] C.T. Eichler. *Flame flashback in wall boundary layers of premixed combustion systems*. Verlag Dr. Hut, 2011. ISBN 3843902518.

[28] F. Faldella. Experimental investigation of Boundary Layer Flashback in high H2 concentration turbulent premixed jet flames. Master thesis, Delft University of Technology, 2020 URL http://resolver.tudelft.nl/uuid:ab0c472e-0dd1-4086-8eeb-18ef14ee226e.

[29] H. Fellouah, C.G. Ball, and A. Pollard. Reynolds number effects within the development region of a turbulent round free jet. *International Journal of Heat and Mass Transfer*, 52(17-18):3943–3954, 2009. ISSN 0017-9310. doi: 10.1016/j.ijheatmasstransfer.2009.03.029.

[30] Andreas Fischer. Imaging flow velocimetry with laser mie scattering. *Applied Sciences*, 7(12):1298, 2017. ISSN 2076-3417. doi: 10.3390/app7121298. URL https://dx.doi.org/10.3390/app7121298.

[31] J. Fritz, M. Kröner, and T. Sattelmayer. Flashback in a swirl burner with cylindrical premixing zone. *Journal of Engineering for Gas Turbines and Power*, 126(2):276–283, 2004. ISSN 0742-4795 1528-8919. doi: 10.1115/1.1473155.

[32] H.C. Gils, Y. Scholz, T. Pregger, D. Luca de Tena, and D. Heide. Integrated modelling of variable renewable energy-based power supply in Europe. *Energy*, 123:173 – 188, 2017. ISSN 0360-5442. doi: https://doi.org/10.1016/j.energy.2017.01.115. URL http://www.sciencedirect.com/science/article/pii/S0360544217301238.

[33] I. Glassman and R.A. Yetter. *Combustion*. Elsevier, Amsterdam ; Boston, 4th edition, 2008. ISBN 9780120885732 (hbk.) 0120885735 (hbk.).

[34] Edward M Greitzer, Choon Sooi Tan, and Martin B Graf. *Internal flow: concepts and applications*, volume 3. Cambridge University Press, 2007.

[35] A. Gruber, J.H. Chen, D. Valiev, and C.K. Law. Direct numerical simulation of premixed flame boundary layer flashback in turbulent channel flow. *Journal of Fluid Mechanics*, 709:516–542, 2012. ISSN 0022-1120 1469-7645. doi: 10.1017/jfm.2012.345.

[36] C. Heeger, R.L. Gordon, M.J. Tummers, T. Sattelmayer, and A. Dreizler. Experimental analysis of flashback in lean premixed swirling flames: upstream flame propagation. *Experiments in Fluids*, 49(4):853–863, 2010. ISSN 0723-4864 1432-1114. doi: 10.1007/s00348-010-0886-0.

[37] V. Hoferichter. *Boundary Layer Flashback in Premixed Combustion Systems*. Thesis, 2017.

[38] V. Hoferichter, C. Hirsch, and T. Sattelmayer. Analytic prediction of unconfined boundary layer flashback limits in premixed hydrogen–air flames. *Combustion Theory and Modelling*, 21(3):382–418, 2017.

[39] A. Kalantari and V. McDonell. Boundary layer flashback of non-swirling premixed flames: Mechanisms, fundamental research, and recent advances. *Progress in Energy and Combustion Science*, 61:249–292, 2017. ISSN 03601285. doi: 10.1016/j.pecs.2017.03.001.

[40] L.N. Khitrin, P.B. Moin, D.B. Smirnov, and V.U. Shevchuk. Peculiarities of laminar- and turbulent-flame flashbacks. *Symposium (International) on Combustion*, 10(1):1285–1291, 1965. ISSN 0082-0784. doi: https://doi.org/10.1016/S0082-0784(65)80263-6. URL https://www.sciencedirect.com/science/article/pii/S0082078465802636. Tenth Symposium (International) on Combustion.

[41] M. Konle, F. Kiesewetter, and T. Sattelmayer. Simultaneous high repetition rate piv–lif-measurements of civb driven flashback. *Experiments in Fluids*, 44(4):529–538, 2007. ISSN 0723-4864 1432-1114. doi: 10.1007/s00348-007-0411-2.

[42] M. Kröner, T. Sattelmayer, J. Fritz, F. Kiesewetter, and C. Hirsch. Flame propagation in swirling flows—effect of local extinction on the combustion induced vortex breakdown. *Combustion Science and Technology*, 179(7):1385–1416, 2007. ISSN 0010-2202 1563-521X. doi: 10.1080/00102200601149902.

[43] T. Lambers. Boundary layer flashback of turbulent premixed hydrogen/dng/air flames produced by a bunsen burner. Master thesis, Delft University of Technology, 2021 URL http://resolver.tudelft.nl/uuid:ad99dd53-063a-48c8-9cf2-cafd31ca3deb.

[44] C.K. Law. *Combustion physics*. Cambridge University Press, New York, 2006. ISBN 9780521870528 (hardback) 0521870526 (hardback). URL http://www.loc.gov/catdir/enhancements/fy0642/2006011565-d.htmlhttp://www.loc.gov/catdir/enhancements/fy0642/2006011565-t.html.

[45] B. Lewis and G. von Elbe. Stability and structure of burner flames. *The Journal of Chemical Physics*, 11(2):75–97, 1943. ISSN 0021-9606 1089-7690. doi: 10.1063/1.1723808.

[46] T. Lieuwen, V. McDonell, D. Santavicca, and T. Sattelmayer. Burner development and operability issues associated with steady flowing syngas fired combustors. *Combustion Science and Technology*, 180(6):1169–1192, 2008. ISSN 0010-2202 1563-521X. doi: 10.1080/00102200801963375.

[47] T.C. Lieuwen. *Unsteady combustor physics*. Cambridge University Press, New York, 2012. ISBN 9781107015999 (hardback) 1107015995 (hardback).

[48] A.N. Lipatnikov and J. Chomiak. Molecular transport effects on turbulent flame propagation and structure. *Progress in Energy and Combustion Science*, 31(1):1–73, 2005. ISSN 0360-1285. doi: 10.1016/j.pecs.2004.07.001.

[49] A.N. Lipatnikov and J. Chomiak. Effects of premixed flames on turbulence and turbulent scalar transport. *Progress in Energy and Combustion Science*, 36(1):1–102, 2010. ISSN 0360-1285. doi: 10.1016/j.pecs.2009.07.001.

[50] F.T.M. Nieuwstadt, J. Westerweel, and B.J. Boersma. *Turbulence: introduction to theory and applications of turbulent flows*. Springer, 2016.

[51] Marcus Ó Conaire, Henry J Curran, John M Simmie, William J Pitz, and Charles K Westbrook. A comprehensive modeling study of hydrogen oxidation. *International journal of chemical kinetics*, 36(11):603–622, 2004.

[52] R.K. Pachauri, M.R. Allen, V.R. Barros, J. Broome, W. Cramer, R. Christ, J.A. Church, L. Clarke, Q. Dahe, and P. Dasgupta. *Climate change 2014: synthesis report. Contribution of Working Groups I, II and III to the fifth assessment report of the Intergovernmental Panel on Climate Change*. Ipcc, 2014. ISBN 9291691437.

[53] N. Peters. Combustion theory. 2010 Lecture material, Aachen University.

[54] N. Peters. Turbulent combustion, 2001.

[55] S.L. Plee and A.M. Mellor. Review of flashback reported in prevaporizing/premixing combustors. *Combustion and Flame*, 32:193–203, 1978. ISSN 0010-2180.

[56] T. Poinsot and D. Veynante. *Theoretical and numerical combustion*. T. Poinsot, D. Veynante, France, 3rd edition, 2011. ISBN 9782746639904 2746639904.

[57] S.B. Pope. Turbulent flows, 2001.

[58] A.E. Potter and A.L. Berlad. The effect of fuel type and pressure on flame quenching. *Symposium (International) on Combustion*, 6(1):27–36, 1957. ISSN 0082-0784. doi: https://doi.org/10.1016/S0082-0784(57)80009-5. URL https://www.sciencedirect.com/science/article/pii/S0082078457800095. Sixth Symposium (International) on Combustion.

[59] G.A. Richards, M.M. McMillian, R.S. Gemmen, W.A. Rogers, and S.R. Cully. Issues for low-emission, fuel-flexible power systems. *Progress in Energy and Combustion Science*, 27(2):141–169, 2001. ISSN 0360-1285. doi: https://doi.org/10.1016/S0360-1285(00)00019-8. URL https://www.sciencedirect.com/science/article/pii/S0360128500000198.

[60] H. Schlichting, K. Gersten, and K. Mayes. *Boundary-layer theory*. Springer„ Berlin, ninth edition. edition, 2016. ISBN 9783662529195 366252919X. doi: 10.1007/978-3-662-52919-5. URL http://dx.doi.org/10.1007/978-3-662-52919-5.

[61] Andrea Sciacchitano and Bernhard Wieneke. Piv uncertainty propagation. *Measurement Science and Technology*, 27(8):084006, 2016.

[62] EFC Somerscales, AN Papyrin, and RI Soloukin. Tracer methods. *Fluid Dynamics. London: Academic Press, Inc.(London) LTD. p*, pages 1–93, 1981.

[63] L.K. Tseng, M. Ismail, and G.M. Faeth. Laminar burning velocities and markstein numbers of hydrocarbonair flames. *Combustion and Flame*, 95(4):410–426, 1993.

[64] Mark J. Tummers, Jeroen Jacobse, and Sebastiaan G.J. Voorbrood. Turbulent flow in the near field of a round impinging jet. *International Journal of Heat and Mass Transfer*, 54(23-24):4939–4948, 2011. ISSN 0017-9310. doi: 10.1016/j.ijheatmasstransfer.2011.07.007.

[65] M. Van Dyke. *An Album of Fluid Motion*. An Album of Fluid Motion. Parabolic Press, 1982. ISBN 9780915760022.

[66] M. van Put. Numerical modelling of flame flashback in premixed tube burners with turbulent flow and high hydrogen content. Master thesis, Delft University of Technology, 2021 URL http://resolver.tudelft.nl/uuid:84b5e88d-72b8-4663-a597-84993aa347f7.

[67] Faizan Habib Vance. *Unravelling flame stabilization: a detailed investigation of Lewis number, flame stretch and heat transfer phenomena*. PhD thesis, Mechanical Engineering, May 2020. Proefschrift.

[68] J. Warnatz, U. Maas, and R.W. Dibble. *Combustion : physical and chemical fundamentals, modeling and simulation, experiments, pollutant formation*. Springer, Berlin ; New York, 4th edition, 2006. ISBN 3540259929 9783540259923.

[69] Z.L. Wei, H.S. Zhen, C.W. Leung, C.S. Cheung, and Z.H. Huang. Heat transfer characteristics and the optimized heating distance of laminar premixed biogas-hydrogen bunsen flame impinging on a flat surface. *International Journal of Hydrogen Energy*, 40(45):15723–15731, 2015. ISSN 0360-3199. doi: 10.1016/j.ijhydene.2015.06.047.

[70] Jerry Westerweel and Fulvio Scarano. Universal outlier detection for piv data. *Experiments in fluids*, 39(6):1096–1100, 2005.

[71] C. R. Wilke. A viscosity equation for gas mixtures. *The Journal of Chemical Physics*, 18(4): 517–519, 1950. ISSN 0021-9606. doi: 10.1063/1.1747673.

[72] F.A. Williams. *Combustion theory 2nd edition*. The Benjamin/Cummings Publishing Company, Inc., 1985.

[73] T. Zorn. The Linde group: Innovation Experience. Hydrogen Technology and Infrastructure. URL https://energiforskmedia.blob.core.windows.net/media/18546/aga-linde-h2-dec.pdf.